UNIVERSITY OF OKLAHOMA

GRADUATE COLLEGE

THE MECHANICAL CHARACTERIZATION OF SUBSURFACE LITHOLOGIES USING AN INTEGRATED APPROACH; COMBINING LABORATORY STUDIES, BOREHOLE & DRILLING DATA AND SEISMIC INFORMATION TO EXPLAIN HYDROCARBON PRODUCTION IN MATURE FIELDS

A THESIS

SUBMITTED TO THE GRADUATE FACULTY

in partial fulfillment of the requirements for the

Degree of

MASTER OF SCIENCE

By

ALEXANDRO VERA-ARROYO
Norman, Oklahoma
2019

Downloaded from SHAREOK. Persistent Handle URL: https://hdl.handle.net/11244/319975

THE MECHANICAL CHARACTERIZATION OF SUBSURFACE LITHOLOGIES USING AN INTEGRATED APPROACH; COMBINING LABORATORY STUDIES, BOREHOLE & DRILLING DATA AND SEISMIC INFORMATION TO EXPLAIN HYDROCARBON PRODUCTION IN MATURE FIELDS

A THESIS APPROVED FOR THE
CONOCOPHILLIPS SCHOOL OF GEOLOGY AND GEOPHYSICS

BY

Dr. Brett M. Carpenter, Chair

Dr. Heather Bedle

Dr. Nori Nakata

© Copyright by ALEXANDRO VERA-ARROYO 2019
All Rights Reserved.

This thesis is dedicated to my father.

Acknowledgments

I would thank Mexico's council of science and technology (CONACYT), in particular, the Department of Energy scholarship (SENER) for providing funding and Pemex Exploracion y Produccion (PEP ®) as my employer.

I would like to express my special appreciation and thanks to my advisor Dr. Carpenter for his thoughtful insights and positive, and precise comments, on both the experimental setup and interpretation of the data, also to accepting me among his students when I most needed. Also, Dr. Heather Bedle has helped me to better understand different aspects of geophysical seismic interpretation and help me to focus my motivation.

My deepest gratitude goes to my advisor Dr. Nori Nakata for countless meetings where he motivated me to exploit my potential and challenge my capacity. Presented to me as an infinite source of ideas and drove me to continue learning.

I thank everyone in my former research group and my actual group, faculty and staff. I am very happy to study and work with them.

Last but not least, my brother Gerardo Vera for all the times he listened to me and helped me. Also, Erika Comparan, my fiancé for all the love and support she unconditionally showed me. Her resilience and discipline are among many other attributes I look up to.

Table of Contents

Acknowledgments v

List of Tables viii

List of Figures ix

Abstract xix

Chapter 1 Introduction 1

1.1 Monitoring in-situ stress and mechanical properties in a reservoir. 1

1.2 Shale velocity anisotropy and its importance 2

1.3 Lab experiments on core samples to study mechanical rock properties 3

1.4 Structure of the thesis 5

Chapter 2 Brittleness characterization of northeastern Oklahoma: An integrated approach to improve near-field exploration 9

2.1 Abstract 9

2.2 Introduction 10

2.2 Tectonic setting 18

2.3 Stratigraphic setting 21

2.4 Dataset description 26

2.4.1 Borehole information 26

2.4.2 Seismic dataset 29

2.5 Methodology and results 31

2.6 Interpretation 71

2.7 Conclusion 88

Chapter 3 Velocity anisotropy analysis from an outcrop sample of the Woodford shale in southern Oklahoma 93
3.1 Introduction 93
3.2 Geological background 94
3.3 Methodology 103
3.4 Wavefield acquisition and waveform analysis 108
3.5 Anisotropy screening 109
3.6 Results 112
3.7 Hydraulic fracture simulation 117
3.8 Anisotropy versus Scattering discussion 122
3.9 Interpretation and discussion 124
Chapter 4 Discussion and Conclusions 129
4.1 Discussion 129
4.2 Conclusions 129
References 133
Appendix A: Experiments to characterize velocity recovery in a porous limestone after a stress-perturbation 145
Appendix B: Table with the wellbores analyzed in the Brittleness Index characterization. 158

List of Tables

Table 1.- Workflow summary as input, model, output and comments and the connection between different. 70

Table 3-2. Stiffness values computed from the measurements for the five unknowns to characterize the horizontal transverse isotropic (Tran et al., 2007; Abousleiman, et al., 2010). 112

Table 3-1. Mechanical properties used as assumptions for the numerical simulation..... 120

Table 4-1. Mechanical parameters used in Adachi J, 2009. 126

Table A-1 . XRF mineralogy composition of the tested rock sample 151

Table 6. Location of the boreholes used in the analysis; 234 wellbores were studied in this project to integrate different the distribution of this table is in Figure B.0-1 166

Table 7. Location of boreholes that were included in the geomechanical model..... 168

Table 8. Latitude and longitude of the boreholes with wireline logs..... 169

List of Figures

Figure 1-1. Distribution in pink envelopes of major carbonate reservoirs in the Gulf of Mexico. In gray, envelopes of hydrocarbon fields producing from siliciclastic. The map interpretation is from National Hydrocarbons Commission (CNH) website..... 6

Figure 1-2. Distribution of unconventional potential resources in Mexico to be explored, characterized and apprise. Map modified after CNH. Note: the potential continuation on the Mexican side of the prolific Barnett Shale..... 7

Figure 1-3. Location of boreholes in the state of Oklahoma, principal structural faults documented by OGS and location of seismic focus. Map generated from integration of different inputs source of information. (Faults from Marsh & Holland, 2016 ,OFS-2016), Earthquakes occurred within Oklahoma from Oklahoma Geological survey(http://www.ou.edu/ogs/research/earthquakes/catalogs) Boreholes from IHS database..... 8

Figure 2-1. Location of the study area enclosed by a dashed line. Black dots represent the borehole locations where information considered for this study was obtained and the black rectangle indicates the location of the seismic survey. 13

Figure 2-2. Bouguer anomaly map from the USGS national potential survey. Green values represent higher Bouguer anomalies, typically associated with shallower, more dense geologic units, such as granite rocks. (USGS, 2016)..... 20

Figure 2-3. A), B) show the contrast in number of detected earthquakes with magnitudes M_w>2.5 between Osage County and neighboring counties. In the area of study only three events

are reported in the OGS. C) Interpreted faults on the basement and upper strata. Fault direction is N 5-10° E..... 21
Figure 2-4. Boreholes drilled in the study area. Approximately two hundred boreholes are drilled inside the amplitude seismic information (cyan boreholes), the remaining of boreholes are outside the amplitude information (green symbols). White symbols overlap with blue symbols, but the difference is the presence of wireline logs 28
Figure 2-5. A) Amplitude spectrums of the 3D seismic frequency distribution. Red curve is the power spectrum from the legacy processing. B) shows the P-velocity distribution from borehole information. C) Vertical resolution plot from frequency distribution and P-velocity..... 30
Figure 2-6. Methodology workflow to integrate data from different streams of information. Potential geophysical data assist interpretation. The selection of discrete facies helps to determine the distribution of P-impedance and attributes. 32
Figure 2-7. Precambrian basement surface used in the geo-cellular model along with the boreholes with sonic information that helped translate the basement location from time to depth..... 33
Figure 2-8. A) Borehole API: 35113200030000. A) P-wave B) S-wave velocity help derive the reflectivity coefficient information. C) The reflectivity coefficient is computed from the P-wave velocity profile. C) The synthetic trace in the left panel is the result of the reflectivity coefficient profile convolved with a 35 Hz Ricker wavelet. 35
Figure 2-9. Well-tie and seismic comparison between the conditioned stack and the legacy amplitude information. A) SP log as a lithological indicator. B) P-velocity and Density

log used as mechanical and lithological logs. C) P-Impedance is the product of P-velocity and Density. D) The equivalent P-velocity after time-depth drift correction. E) The legacy seismic information on the borehole position. F) The extracted wavelet and the synthetic seismic trace used to correlate the observed data with the synthetic trace. G) The conditioned seismic trace. H) The wavelet extracted from the seismic data (8 degrees phase). 36

Figure 2-10. 1-D Ray-tracing at seismic frequency from borehole information. A) P-wave profile. B) S-wave profile. C) Equivalent synthetic seismic response at 20 Hz resolution, which is the resolution of seismic information basement depth. 38

Figure 2-11. A) Petrophysical curves to represent the model and fluid substitution in the Mississippi Lime. First panel shows the GR variability and second profile is water saturation curvature. B) is the synthetic seismic wedge model to investigate the tuning thickness. 39

Figure 2-12. Porosity distribution on the Mississippi Lime. A) Density distribution function. B) Histogram distribution. 41

Figure 2-13. Maximum curvature attribute extraction on top of the basement. 42

Figure 2-14. Representative tectonic framework on the seismic generated from seismic interpretation. Different fault colors represent the variety of faults orientation, depth and age. Green horizon represents the Mississippi Lime. Blue surface is the basement interpreted in the survey and affected by the tectonism. The vertical extension of blue and violet faults suggests a possible connection between shallower strata and the granitic basement. 44

Figure 2-15. A) 3D Seismic inline and crossline to show down lap terminations. These patterns guided the mechanical property extrapolation. B) Discretized facies distribution on top of the Mississippi Lime. The mechanical pattern represents the three different lithologies observed in the boreholes..... 46

Figure 2-16. Fault likelihood attribute on the top of the interpreted basement. The attribute shows a North to South fault set trend on the top of the basement..... 48

Figure 2-17. Scheme to compute pattern recognition attribute. Attribute computed and used for flat structure classification and correlation of the selected mechanical stratigraphy..... 50

Figure 2-18. Rock-physics model of the Mississippian Limestone calibrated from lithological information and water saturation. 51

Figure 2-19. Geomechanical model representative of the borehole information. A) Discrete mechanical facies used on the model. B) GR profile, C) P-Velocity profile D) S-velocity from the rock-physics model. E) Density profile F) Total Porosity and Porosity trend G) Clay volume H) Unconfined Compressive strength from the mechanical model I) Friction angle curve from the poro-elastic model J) Shear modulus K) Bulk modulus L) Drilling window..... 54

Figure 2-20. P-Impedance distribution in a W-E section from the post-stack seismic inversion. 65

Figure 2-21. Mechanical facies classification (BI) using P-Impedance and the geocellular model section showing the discrete facies distribution with depth..... 68

Figure 2-22. Basement and other irregularities on the brittle facies classification with fault likelihood and compaction attribute included..... 69

Figure 2-23. The 3D visualization of the inner basement low brittleness anomaly, this low BI anomaly could represent volcanic intrusions or a change on lithology. 73
Figure 2-24. Schematic section on the different thickness as a function of structured basement along with other secondary deposition features. (Modified after an interpretation similar in Becerra, 2017)..... 74
Figure 2-25. BI section shows a borehole that intersect a low brittleness anomaly on the basement. The borehole suffered a major fluid loss of circulation. 75
Figure 2-26. 3D visualization of the high values of the high Brittleness Index in the Mississippi Lime (ML). The vertical seals separate reservoir levels. Also the BI shows the inner basement low brittleness anomaly. 79
Figure 2-27. Brittleness index distribution on the Mississippian Chert. Polygons show basement topography via contour lines..... 80
Figure 2-28. Accumulative oil production of Osage County. The highest hydrocarbon production accumulations correspond to higher values of the Brittleness Index..... 81
Figure 2-29.Woodford shale thickness in southwest Osage County with BI attribute extracted on the surface interpreted as the Woodford shale. 83
Figure 2-30. Maximum extraction of BI attribute on the Woodford shale. Displayed on the figure, the boreholes with reported production from the Woodford shale and a normal fault on the west portion of the study area. 84
Figure 2-31. Basement low brittleness anomaly distribution and white dash lines represents the direction of the section on Figure 2-25. Location of borehole A and B shows the borehole result..... 86

Figure 3-1. Location of the Woodford outcrop were the sample was collected. Abundant production has been documented from the oilfield's northwest and west of the outcrop. 95

Figure 3-2. Stratigraphical chart of the organic Woodford shale deposited from 388 to 359 Ma(stratigraphic chart from (Johnson & Cardott 1992; Bernal, 2013). 96

Figure 3-3. Structural schematic sections showing the evolution of Southern Oklahoma (after Ataman 2008; modified from Bixler, 1993). 97

Figure 3-4 . A) Top view of the Macalister outcrop is from Google maps to show the color contrast between formation contact and dip of the formations. B) North-South view of the outcrop I took the photo during a field trip to the McAlister cemetery quarry. The red squares represent the area of where the sample was collected. 98

Figure 3-5. A) Fracture sets present in the mudrock on the top of the outcrop photo by (Ghosh, 2017). Two main sets are product of tectonic events, other fractures are post exhumation. B) A zoom on the outcrop, the siliceous mudrock is intercalated by shales, contains few to no fractures in core and outcrop hand sample, and exhibits a papery to platy stratification. The vertical fractures are only evident on the massive rock and are perpendicular to the clayrock. C) The massive texture on the mudrock with siliceous bed intercalated. (B and C) are pictures taken by me. 100

Figure 3-6. All organic matter plots on the type I kerogen, which is lacustrine kerogen. The high Molybdenum concentration (Algeo et al., 2009) suggest a less restricted depositional environment, typical of an open lacustrine environment with sporadically water input from outer sources (data collected & analyzed in (Ifunaya, 2017). 101

Figure 3-7. Kerogen type and maturity assessment of the Woodford shale of studies conducted from (Bernal, 2013). The type of kerogen present (Type I, II, and III) is dependent on the different hydrocarbon produced with increasing thermal maturity (Ifunaya, 2017). 102

Figure 3-8. A) Mudrock sample from the quarry before undergoing the process of core sampling. It is a light gray with orange tones and bitumen filled fractures observed. B) Mudrock sample after collecting the four plugs, the change in color is due to water and other additives (grease) interaction during the core drilling. The change in color also gives inference on how the fluid can quickly interact with the rock. C) Plugs and rock sample after removing surface asperities. 104

Figure 3-9 Complete diagram for active ultrasonic acquisition setup for the shale plug to screen anisotropy..... 105

Figure 3-10. A) Acquisition diagram an ultrasonic active source used to measure first arrivals times to compute the velocity of P and S waves. Polarization of the sensors is represented on the receivers. B) second stage of acquisition with source parallel to fracture direction. C) Third stage of acquisition with source and receivers vertically oriented..... 107

Figure 3-11. A) Waveform representative of P and S wave at a source frequency of 150 kHz. B) Spectrogram of S-wave sensor, recording a 250 kHz. The peak of power amplitude is centered at 120 kHz. The low frequency band present is due to mechanical noise in the lab..... 109

Figure 3-12. Scheme on the VTI model for fractures of the rock sample. The horizontal plane is a plane taken from the rock sample. Conceptual model from (Tsvankin, 2013)..... 110

Figure 3-13. P-Wave velocity summary of a source activated on the X_2-X'_2 parallel to the fracture. 113
Figure 3-14. S-wave velocity profile as a function of frequency for X_1-X'_1, X_2-X'_2 and X_3-X'_3 direction. 114
Figure 3-15. P-Wave profiles on different direction on the rock sample acquired as a function of frequency when the source is activated on the X_2-X'_2. 115
Figure 3-16. S-Wave profiles as a function of frequency for a source activated on the X_1-X'_1 direction, that is perpendicular to the filled fracture. 116
Figure 3-17. Conceptual model and important terms of a hydraulic fracture (image modified from (J. Guo et al., 2016). 118
Figure 3-18. Conceptual Data Frack of a hydraulic fracture job. Derived from (Meng & De Pater, 2010) 119
Figure 3-19. Stress concentration on the X_2-X'_2 direction. A) Initial stage of the fracture propagation, the fracture initiates at a stress difference 75 PSI. B) shows the fracture on a late time stage (3 min) with a maximum horizontal stress difference of 100 PSI. 121
Figure 3-20 Stress concentration on the X_1-X'_1 direction A) Early stage of the fracture propagation, the fracture initiates at a stress difference 100 PSI. B) Later time step with a 900 PSI difference 122
Figure 3-21. Scattering effect after an incident plane wave a) Initial model of a numerical simulation in Madagascar with a Gaussian velocity anomaly of shape (1/r) faster than the background b) wave propagation on the isotropic media c) Wavefront impact the velocity

anomaly d) wavefront shape is affected, amplitude decrease and wavefront becomes flat. 123
Figure 3-22 Example of fracture height growth of stress contrast on a pseudo 3D modeling on an isotropic case. 126
Figure A-1-1 Acquisition diagram for damage experiments -Source-Sample-Receivers-Recording system-waveforms. 148
Figure A-1-2 Background monitoring and source and sensor location 149
Figure A-1-3 Damage monitoring and source and sensor location 150
Figure A-1-4 Loading scheme and waveform acquisition. 151
Figure A-1-5. Failure test to determine the maximum stress and the elastic behavior. The non-linear and linear change exhibit the non-elastic and elastic behavior of the rock. 152
Figure A-1-6. Velocity monitoring without any perturbation for 4200 seconds. 153
Figure A-1-7. This plot shows the velocity monitoring for monitoring different impacts. 153
Figure A-1-8. Velocity change with fitting lines from the experiment using the scheme on Figure 1-4. With two uniaxial compressions, the first at 50 seconds and the second at 2 min 40 seconds. The stress applied in this experiment was 250 psi (5% of maximum stress) and 500 psi (10 % of maximum stress), to make sure I was on the non-elastic domain and well below the maximum compressional strength of the rock. 154
Figure A-1-9. Portions of the rock sample with a difference in the porosity distribution. Red line represents the middle of the sample. 157

Figure B-1-1. Location of total list of boreholes analyzed in black symbols, blue dots represents the boreholes that were used during the geomechanical modeling either as mud-profiles to calibrate pressure, or formation integrity test when cemented the casing sites. 166

Figure B-1-2 Color location represent boreholes with wireline information, where I derived and compute multiple attributes. This survey has a well density of 3 wells per square kilometer. 169

Abstract

In our current energy landscape, subsurface assessment challenges within the oil industry are becoming more difficult. Mature stage reservoirs present an opportunity to individually investigate different components of the industry, e.g. drilling, completion, wireline logs, and seismic data. However, in order to understand the mechanisms driving reservoir production, it is vital to expand our understanding of reservoir properties, the mechanical relationship between fluid and rock and important tectonic context.

Mexico's oil industry has faced a major change in the last five years; however, PEMEX ® has managed to significantly expand activities in exploration and production of leased areas. Vast areas of these concession blocks have potential field data, seismic information (2D and 3D) and boreholes drilled with a complete suite of wireline logs. These areas are deeply studied and present an opportunity to integrate geophysics, geology and engineering inputs to understand the compelling drivers of production and production changes.

In this thesis, I explored the fundamental aspects related to two rock types that represent the present and future in terms of prospective resources, i.e. carbonate and shale reservoirs. On the first topic, my research focused on how the interpreted brittle behavior of the reservoir rocks deeply impacts the accumulative hydrocarbon production, and its competence to store wastewater. For the second research topic I conducted fieldwork to gather representative rock samples to screen for anisotropy and related anisotropic properties to hydraulic fracture propagation.

To investigate the Mississippi Lime, I used multiple datasets located in northern Oklahoma. Oklahoma, in particular Osage county, has been intensively drilled since the first well was

completed in 1896. By 1982 Osage county was second nationwide for wells drilled with more than 35,000 drilled wells and produced more than 450 million barrels of Oklahoma crude oil. This production was due to a high density of drilled wells. Given the well density of the area, an unintended benefit of the boreholes per square kilometer was obtaining deep insight into the physical properties of the subsurface, i.e. resistivity, sonic information, rock description, water saturation, etc. Using gravimetry and magnetic data recorded in the area and correlating the basement geometry with seismic information in southeastern Osage county, I established a fault architecture for the area. From borehole wireline logs, I investigated the dynamic elastic properties. Using rock-physics models, seismic data, and P-impedance inversion, I laterally extended the determined properties over the study area. Additionally, I computed rock mechanic properties at singular borehole positions and extended these properties using seismic inversion correlated with borehole log data. Finally, I calibrated my results using geomechanical models of several wells to determine the Brittleness Index (BI).

The results of this study, combined with velocity profiles from additional wells, showed the possible occurrence of a low velocity layer, below seismic resolution, near the top of the Precambrian basement. Furthermore, my results, when combined with production data, showed the sealing capacity of faults in the area and resulting compartmentalization. In general, using rock physics and well-log information from boreholes in the area, I showed that boreholes drilled near deep low brittleness zones experienced a severe loss of circulation. These low BI anomalies are likely due to structural elements near the basement top, elements that may propagate up into the shallower sedimentary sequences. Overall these results suggest structural connectivity

between structural elements in Paleozoic groups and the fractured igneous rocks that constitute the Precambrian basement of northeastern Oklahoma.

The Woodford shale is of particular interest as it is one of the most drilled and completed plays in our current energy landscape. Anisotropy characterization, combining geology and reservoir engineering, is paramount for well placement and well landing. Most materials show an anisotropic and heterogeneous behavior when evaluated at different scales, this is specifically true of shales at the scale of interest to completion and drilling engineers. Shale exhibits different acoustic characteristics as it encompasses the most common causes of anisotropy; stress, layering and, fractures. In this work I measured shear and compressional velocities at different frequency ranges to evaluate and characterize anisotropy in the Woodford shale. The incorporation of frequency sweeps in ultrasonic measurements of fractured upper Woodford shale could potentially identify anisotropy and its causes. I measured seismic velocities parallel to the bedding, perpendicular to fractures, perpendicular to bedding and parallel to fractures. I estimated the dynamic and static elastic modulus (shear, bulk, Young's modulus, and Poisson's ratio) accounting for shear and compressional velocity differences. I used the computed elastic moduli to generate a precise geomechanical model to determine the effects of anisotropy on hydraulic fracturing. The model, combined with numerical simulations allowed for the differences in fracture performance and geometry to be quantified. Also quantified were hydraulic fracture geometry, height and width, and the fluid pressure distribution within the fracture/formation boundary. The results showed the impact of correctly defining the anisotropy to evaluate, design, and budget efficient hydraulic fracture jobs.

Chapter 1 Introduction

1.1 Monitoring in-situ stress and mechanical properties in a reservoir.

It is vital for multiple objectives to infer subsurface velocity from active and passive seismology. For example, velocities are used as a parameter to explore mechanical properties, map mineral resources, and subsurface geomorphologies. Velocity information can be used for example to monitor pore fluid content (Nur, 1987), thermal fracturing (Looms, et al., 2008), state of stress around the fracture (Santamarina, et al., 1992), perturbation of the stress field, (Scott et al., 1994), mechanical anisotropy (Scott, et al., 2001), thermal maturity (Harris, 2015), mechanical recovery (Nakata & Snieder, 2011; Sleep & Nakata, 2017, 2018) and for many other effects.

Mexico's current energy sector is challenging and in constant change. Nowadays, most hydrocarbon production of PEMEX ® comes from the hydrocarbon reservoirs located in Campeche Sound. These reservoirs have been producing from Mesozoic carbonate rocks since 1979 and are in a mature stage. However, Mexico's energy plan for the next ten years is contemplating the integration of production from non-conventional reservoirs. The objective is to move exploration and production efforts, from producing 80% of the national production of Mexico (Romo, 2015) out of mainly carbonate debris flows facies deposited on the Yucatan slope (Figure 1-1), to Jurassic shales in the north and northeast portions of the country (Figure 1-2). These challenges share one goal, the quest for efficiency. That is, becoming more efficient in oil exploration and production in mature carbonates and program-efficient drilling and completions campaigns for non-conventional plays. This thesis project concentrated on developing a correlation between deformation and mechanical properties of subsurface rocks and their acoustic velocity signatures.

In this thesis, I aim to contribute to those challenges by first integrating different pieces of geophysical information in the exploration-production of a mature play by designing a methodology that derives mechanical properties related to reservoir capacity, to hydrocarbon production or to waste water storage. Subsequently, I will study a mechanism to screen the anisotropy effect in hydraulic fracturing by collecting an analogous outcrop rock sample, prepare to acquiring velocity profiles and deriving mechanical properties from it. Then I will use those results to model the stress concentration and propagation of a hydraulic fracture.

1.2 Shale velocity anisotropy and its importance

Most formations are heterogeneous and anisotropic at the mineral grain size scale, but when evaluated for drilling and completion, the investigation tool resolution limits the depth of investigation of the diverse constituents. In exploration geophysics, clay lithologies were at one point thought as of homogeneous material. Shales were commonly mischaracterized as an isotropic rock, but deeper examination has provided information showing them to be completely the opposite (Sayers, 2001; Slatt et al., 2011). Anisotropy is defined as the variation of a property as a function in which the property is measured: the dominant cause of anisotropy is heterogeneity.

The understanding of shale anisotropy has improved significantly since the combination of expertise in rock mechanics, measurements of borehole images and acoustics at the borehole scale, and more sophisticated processing algorithms that are tailored to fit to seismic acquisition (WAZ, coil technologies, etc.).

Today's difficulty is no longer in obtaining realistic values of the elastic constants; the challenges are now implementing the complex workflows across multiple disciplines and

platforms to apply 3D anisotropy of the elastic constants and computing the earth stresses based on the anisotropic moduli.

Understanding anisotropy in a reservoir shale requires researching the mechanical stiffness tensor (Tsvankin, 2013). The scale resolution might be derived at the micro-scale from laboratory experiments to regional scales from seismic azimuthal studies. The cost of these studies is proportional to the detail and scale magnitude. However, using analogous outcrop rock samples can help to investigate the impact the inclusion of transversely isotropy materials in numerical simulations. A transversely isotropy material is one that has the same property value in two directions but a different property value in the third direction (Tsvankin, 2013).

Understanding the anisotropy constitutive values helps to compute the condition of uniaxial-strain compression for the evaluation of the effective horizonal stress. Multiple methodologies might assist in detecting the minimum horizontal stress before well completion; once the wellbore is drilled, , it is a complex task to achieve. Estimating the minimum horizontal stress from laboratory geophysical techniques can help in the design of drilling and completion campaigns.

1.3 Lab experiments on core samples to study mechanical rock properties

Laboratory experiments to monitor velocity as a function of stress, temperature, and hydrocarbon concentration have helped derive important correlations since the late 1960s (Nur et al., 1969 ; Gupta, 1973 ; Lo et al., 1986 ; Fjær et al., 1992; Sayers et al., 1990; Scott et al., 1994). One of the multiple experimental challenges of information derived from core samples is the different scale paradox. For example, naturally fractured reservoirs are vital for geophysics exploration, either for producing from or controlling fluid storage. Detecting fractures on a core

scale is a challenge solved via ultrasonics (Pan et al., 2017), or via nuclear magnetic resonance techniques (Kerimov, 2013). However, characterizing at the seismic fractures on seismic exploration scale remains to be challenging. On the lower end of the frequency spectrum, to investigate fractures the tools to study fractured reservoirs are compressional wave anisotropy (Guo et al., 2013; Pan et al., 2017; Vernik & Liu, 2002 ; Li, et al., 2016), shear wave splitting (Baird et al., 2015) and seismic attributes such an anomalous curvature (Chopra & Marfurt, 2014).

The upscaling challenge of the most representative physical measurements to characterize fractured, porous systems or fluid attenuation mechanisms remains. In laboratory measurements, the rock sample is typically less than hundreds of centimeters. Using high frequency-high resolution setups (1000 Hz to 1 MHz) comes with the challenge of translating crucial relationships to measurements of the same physical property for example, the p-wave velocity calculated from first arrival travel time tomography which different by several orders magnitude. Thus, lower frequencies of investigation reduce the ability to detect the heterogeneities a method can resolve and vice versa (borehole wireline logs ~20 kHz, seismic velocities ~100 Hz, GPS information ~10 Hz).

In the field, a major advantage of experimental studies at laboratory scales is the possibility to study rock-fluid system interaction by discerning frequency dependent attenuation observed in fluid saturated rocks versus dry samples (Tisato & Madonna, 2012). However, seismic attenuation in fluid-saturated rocks remains to be more of an interpretative result than a quantitative. Laboratory studies at seismic frequency presents an opportunity to study wave attenuation at seismic frequencies on rock sample scales (Goodfellow et al., 2015).

1.4 Structure of the thesis

This thesis is structured to show a realm of geophysical exploration tools to assess subsurface properties and guide near-field exploration suited for mature areas. Borehole density, regardless of the wireline information present, can represent an essential piece of information that can mitigate the exploration risk and accelerate reserves incorporation. Different drilling and termination parameters can shed insight into the mechanical properties and the current in-situ stress. These parameters among others such as lithology and stratigraphy control the efficiency and effectiveness on the oilfield appraisal. This thesis integrates information from the borehole, potential data, seismic amplitude, rock laboratory experiments, and outcrop analysis to study essential information that directly impacts hydrocarbon production.

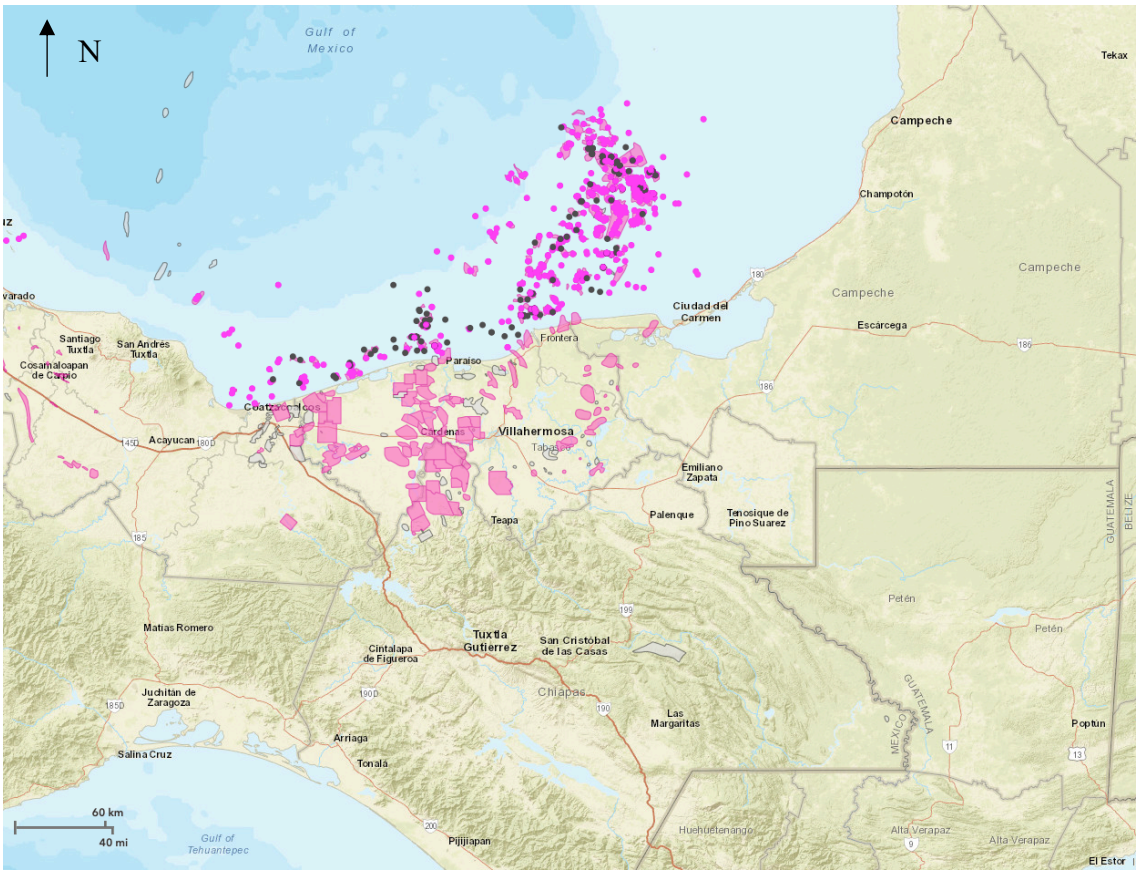

Figure 1-1. Distribution in pink envelopes of major carbonate reservoirs in the Gulf of Mexico. In gray, envelopes of hydrocarbon fields producing from siliciclastic. The map interpretation is from National Hydrocarbons Commission (CNH) website.



Gas prone potential resources Oil prone potential resources

Figure 1-2. Distribution of unconventional potential resources in Mexico to be explored, characterized and apprise. Map modified after CNH. Note: the potential continuation on the Mexican side of the prolific Barnett Shale.

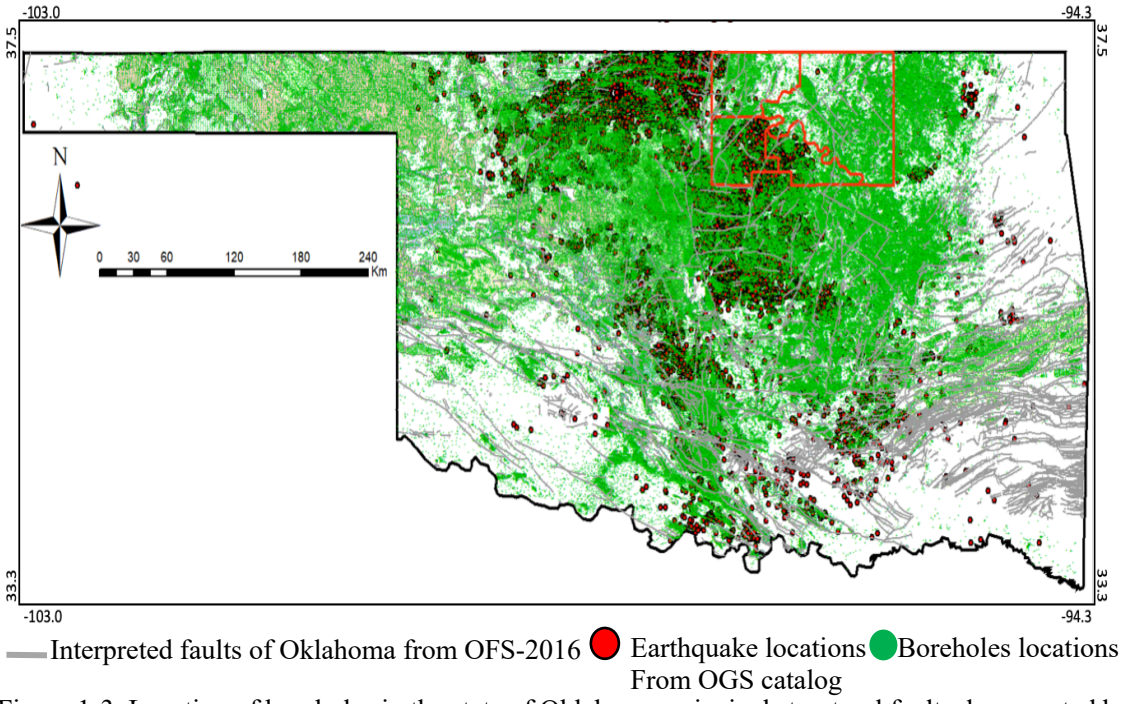

Figure 1-3. Location of boreholes in the state of Oklahoma, principal structural faults documented by OGS and location of seismic focus. Map generated from integration of different inputs source of information. (Faults from Marsh & Holland, 2016 ,OFS-2016), Earthquakes occurred within Oklahoma from Oklahoma Geological survey(http://www.ou.edu/ogs/research/earthquakes/catalogs) Boreholes from IHS database.

Chapter 2 Brittleness characterization of northeastern Oklahoma: An integrated approach to improve near-field exploration

2.1 Abstract

I developed a methodology to predict reservoir properties: porosity, water saturation, and facies, and applied it to an oil field in Osage County, Oklahoma. With this method, I estimated the mechanical properties (elastic modulus, shear modulus, and brittleness) of the subsurface from integrating different streams of information, borehole data, potential data, seismic attributes, and seismic inversion calibrated with well data analysis to improve the understanding of reservoir mechanical properties. Mechanical properties are merged within a sequence stratigraphy framework, incorporating mechanical fault stratigraphy, rock physics, and geomechanics models. This multistage integration created a comprehensive methodology that incorporates different inputs and translates them into a calibrated 3D mechanical model. The subsurface mechanical information is essential for understanding direction of fluid movement, as well as developing drilling strategies and successful completion of the exploration prospect. This mechanical model can be used to identify "sweet spots" in brittle zones for more efficient drilling and completion campaigns. The predictive power of sequence stratigraphy is used to obtain spatial trends of deposition in combination with trace attributes to aid in the detection and interpretation of complex tectonic events that confine sedimentological parameters are additionally useful for rock physics modeling. This methodology closes the gap between seismic information (phase and amplitude), drilling events, and wireline log data. The model, calibrated with borehole evidence of the

mechanical properties and lithology distribution, helped to discern favorable zones for well landing and sweet spot detection, identifying potential units for re-stimulation in the area.

2.2 Introduction

The area of study is located geographically in the southwest portion of Osage County, in the northern part of Oklahoma (Figure **2**-**1**). Osage County is bounded to the north by the Kansas state line and to the south by the Arkansas River, which represents the boundary of Osage County and Pawnee County. Osage County extends east to Kay and Noble counties and west to Washington, Pawnee, and Tulsa counties. Geologically, the study area is located inside of the Cherokee Platform basin, east of Nemaha uplift and west of the Ozarka Uplift.

Oklahoma's oil industry presents an opportunity to collect evidence of subsurface petrophysical properties such as water/oil saturation, permeability, porosity, and other mechanical properties. Northern Oklahoma, in particular, Osage County has been intensively drilled. The first borehole drilled in the area was in 1896. By 1982, Osage County was the second largest nationwide for wells drilled, due to the combination of low cost/low-risk projects that allowed investments with low-production rates (5-10 barrels per day per well). This long history of hydrocarbon exploration has resulted in more than 35,000 drilled wells and produced more than 450 million barrels of crude oil and 305,000 million cubic feet (MCFs) of gas. As of 2018, Osage County is ranked at 66th place in Oklahoma oil production, and 899th national overall production. Sixty-nine companies operate within Osage County and produce 120 MCFs per day and less than 50 OBD. Saltwater disposal (SWD) boreholes in Osage County represent around 8% of statewide saltwater

disposal volumes i.e., 120 million barrels in 2014 (Murray, et al., 2014), with increasing rates that mimic hydrocarbon production volume. The seismic activity associated with SWD near strike-slip faults, primarily when the faults are oriented in optimal directions along the regional stresses (Chen et al., 2017; Goebel et al., 2017).

During the Oklahoma oil boom oilfields in Osage County were under the misleading concept of a flat carbonate shelf with no structural traps present in the area, causing hundreds of dry holes to be drilled on a misleading concept. Beckwith (1928) documented the petroleum exploration potential of the Osage Indian reservation lands. Dott (1942) conducted a study of Pennsylvanian paleogeography using borehole information to illustrate the distribution of seas during Pennsylvanian age and to tie his observations to neighboring tectonic events, using the already drilled wells to input the lithological information into a comprehensive study, preceding major oil discoveries. Bass (1940) and Tanner (Tanner, 1956) documented the subsurface geology and petroleum resources in Osage County, specifically in the northeastern part of the County, highlighting the trap configuration and documenting mostly stratigraphic traps in platform carbonates due to minor folds present in northern Oklahoma.

Since 1990, efforts made to rejuvenate oil exploration in the area resulted in an peak-oil production of 4 million oil barrels in 1993. In 1998, the U.S Department of Energy (DOE) established a policy to reverse declined hydrocarbon production base. The objective of this program focused on re-igniting exploration and production activities and abated domestic oil dependence. The principal beneficiaries of this program were small independent operators. The DOE shot a series of 3D seismic surveys in Osage County, to encourage exploration and drilling

of new plays (Reeves et at., 1999), promoting more aggressive domestic production by smaller independent companies. These exploration efforts yielded a sustained growth of gas production with a peak production of 2.7 MCFs in late 2014.

Due to the long history of hydrocarbon exploration and production, Osage County is one of the most analyzed and drilled areas of oil and gas in the United States. In this study, I integrate 3D seismic data and borehole data within different critical elements. I exploit the benefits of seismic data laterally, extending the range of investigation of the borehole information. I compute impedance inversion and correlate well-log data with post-stack seismic attributes. Among the attributes computed Curvature and Coherence are sensitive to lateral changes of the structure, while impedance inversion tied with a rock physics is sensitive to lithology. Moreover, I use geomechanical models to calibrate the elastic properties to understand the complex interplay of brittleness with elastic properties and lithology that could potentially be useful for completing SWD wells or hydrocarbon wells. The combination of these data analyses, that employ multiple datasets allow a more thorough and complete understanding of rock properties that control fluid distribution. The mechanical properties that have a large effect on rock frackability, specially on non-conventional plays.

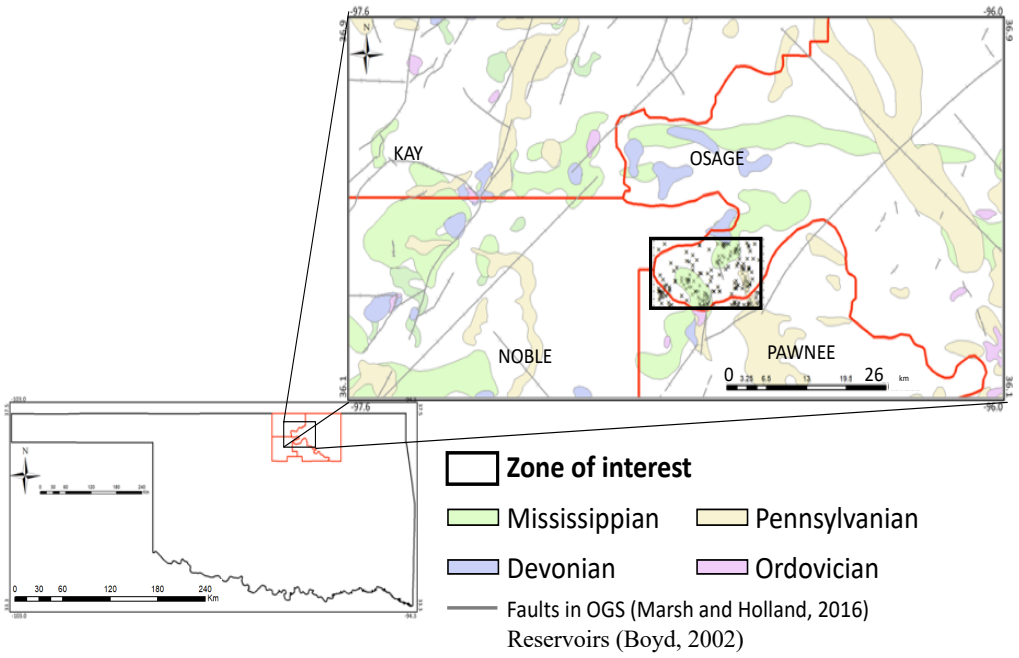

Figure 2-1. Location of the study area enclosed by a dashed line. Black dots represent the borehole locations where information considered for this study was obtained and the black rectangle indicates the location of the seismic survey.

The production context is important to highlight the mature stage of Osage county oilfields. The vast amount of information that has gathered over the last century. The integration of different streams of information is the main goal of this thesis work, that seeks to create a framework to process the information using different techniques.

It is located geologically in the southwestern portion of the geological province of the Cherokee platform. The reservoir unit deeply studied in this area is known as the Mississippi Lime (Boyd, 2002), a diagenetically altered carbonate reservoir. I used a variety of information from 234 wellbores to build a mechanical model and gain understanding of basement properties. The calibration of my results with information from the shallower sedimentary sequences boosts my confidence in predictions made for Cambrian and Precambrian lithologies.

Osage County has four reservoir units present; Mississippian, Ordovician, Pennsylvanian and Devonian, this last one is the most restricted. Osage County produces mostly gas and condensate at a depth range of 800 meters to 1050 meters (Sebaa et al., 2006; Trumbo, 2014 ; Reeves et al., 1999; Evans & Suneson, 2016). The area was reinvigorated in early 2003, due to buoyant oil prices. The most prospected stratigraphic levels in the study area were the Mississippi Lime, Pennsylvanian and even some production was reported from a Cambrian sandstone, the Reagan sandstone. However, the exploration efforts to establish continuity of the proliferous Woodford shale to the northeast were insufficient.

To activate and establish production from the Woodford shale in north central Oklahoma, up to seventeen wells were drilled. Production from these wells was low gas flows and lower oil rates, around 17 OBD. (Bass et al., 1941; Williams, 2013). The low hydrocarbon production rates from the Woodford shale contrast to the highly fractured Mississippi Lime and most a prolific oil and gas producer in northern Oklahoma. Moreover, just recently, oil reserves were documented and estimated of ultimate recovery of more than 50 thousand barrels of oil equivalent per well with thirteen boreholes programmed, this discovery is reported to take place on the Mississippian (Sea River, 2018).

As exploration and drilling campaigns resumed in recent years, the need to have a better understanding of reservoir extension and net thickness has become paramount. While most of the exploration activities utilized 3D seismic technology to discover and develop oil and gas reserves, limited attempts were made to study the lateral changes of mechanical properties. (Dowdell et al., 2012; Elebiju, et al., 2009; Matson et al., 2011; Elebiju et al., 2011). Blain (2014) focused on

imaging and mapping stratigraphic units of interest and faults that potentially can be either prospective or challenging during horizontal drilling. Although, these studies have largely ignored a reasonably good configuration of faults and Paleozoic units present in the area, the mechanical properties have bypassed. Also, some efforts have been made to characterize and understand the deep fault architecture and its impact on shallower stratigraphic reservoirs (Elebiju, Matson, Keller, et al., 2011).

Other studies (Dowdell et al., 2012 ; Dowdell et al., 2013; Roy et al., 2013) have focused on mapping of a highly porous tripolitic chert within the highly fractured Mississippian siliceous lime reservoir (chert), using impedance inversion and making the correlation with post-stack seismic attributes and well log information. West of Osage County, a characterization of Mississippi Lime production using only acoustic impedance and seismic attributes with production wells showed the relationship with high porous cherts (Trumbo, 2014) but failed to explain the productivity index. This study in particular did not include porosity and mechanical characterization of the Mississippi Lime. Also, the study did not considered the effects of overburden, stress fields, or mechanical stratigraphy of the circumvent rocks. In 2018, a statistical correlation of structural seismic attributes with mechanical properties (Lame constants and porosity) was performed, aimed to better assess the rate of penetration (ROP) (Qi, 2018) in drilling campaigns. This study used 51 boreholes at the northern portion of the Nemaha Uplift in Woods County to estimate Mississippi Lime mechanical heterogeneities and its relationship with rate of penetration and brittleness. Yet, a rock-physics model was missing to calibrate amplitude to elastic properties or pore pressure, mechanical stratigraphy, estimation of horizontal stress and more than 30 engineering factors; such as bit and bottom hole assembly, weight on bit, drilling fluid and

formation temperature to name some, were taken into the statistics, to soundly evaluate the mechanical properties.

In the quest of understating the mechanical shale properties of unconventional shale plays is important to have a complete study on how mechanical stratigraphy impacts productivity by improving the efficiency of hydraulic fracture jobs (Slatt et al., 2011). The sequence stratigraphy dominates the brittleness distribution in shale units; an integrated approach, focused on understanding sequence stratigraphy increased the efficiency of hydraulic fractures. Zhang et al. (2016) documented how shale deposits models control the growth pattern of induced fractures, identifying shale deposited under particular facies environments is helpful for discerning brittle beds versus ductile beds.

Brittleness is a measurement of stored energy before failure and is primarily a function of rock strength, lithology, inner rock texture, effective stress, temperature, fluid type, diagenesis, and total organic content (TOC) (Slatt et al., 2011). In these studies, mineral proxies analyses merged with shale sequence stratigraphy predict the distribution of microseismic events. However, this approach is limited to in-field production or near-field exploration since it relies heavily on element characterization to obtain brittleness models or does not take into account space variability of the sequence stratigraphic model. Applications of this work is related to the design of frack jobs in an already drilled wells, making it difficult for budgeting and resource allocation beforehand.

Studies on shale reservoir have shown the advantages of data integration in unconventional reservoirs (Dicman & Vernik, 2012; Sayers, 2013; Sayers & den Boer, 2018; Sone, 2012; Vanorio et al., 2008; Vernik & Liu, 1997; Vernik & Milovac, 2011; Zhao et al., 2016) to comprehensively

understand the sequence stratigraphy depositional model of shale reservoirs and their impact on mechanical properties, not only from the standpoint of element proxies, but, its space distribution at seismic scale level. This integration could potentially yield a better definition of natural resources and the complex interplay of hydrocarbon production from a brittle formation and water injection into a brittle formation.

Additionally, rock physics models have shown their importance in closing the gap between borehole information and seismic data, and just recently the effect of organic matter and in general shale rock physics models have been gaining research interest. Rock physics builds the bridge from elastic properties with amplitude information, and geomechanics offer calibration points, especially in areas with a dense distribution of wells. Thus, a framework that encompasses the distribution of mechanical properties and stresses of the reservoirs is most needed to gain an understanding of the complete stratigraphic column and potentially explain reservoir links with deeper structures throughout the faults that have controlled the deposit architecture and migration pathways.

In this work, I study the link of elastic properties in the stratigraphic column with the tectonic configuration using seismic amplitude seismic information to interpret major events and structural seismic attribute fault mechanics with the Paleozoic stratigraphy. This resulted into a mechanical earth model that is employed to extrapolate borehole facies and log information. The mechanical stratigraphy and stress field conditions generate a geomechanical model using information from 234 wells to gain an understanding of the subsurface mechanical heterogeneities and monitoring unconventional reservoir mechanical properties.

Finally, I compute a 3D seismic inversion for unconventional reservoir properties combining statistical rock physics and geostatistics using thirteen wells with wireline digital logs to calibrate acoustic impedance with the rock physics model that was created with a methodology to deliver a Brittleness Index model (BI). This BI model is then calibrated with sequence stratigraphy and mechanical stratigraphy using the 3D seismic survey. Combining these attributes with the extrapolated facies model with higher frequency information from the P-Impedance and the geomechanical geocellular models better describes reservoir properties that are not discerned through brittle-ductile couplets.

2.2 Tectonic setting

Seismic imaging of the subsurface is a common task to explore for natural resources. However, an unintended benefit of the 3D seismic shot in Osage County is imaging the Precambrian granitic basement and the fault distribution. Basement and faults in the strata directly control features in overlaying sedimentary formations and mechanical properties. The paleotopography generated by the irregular granitic subsurface and a contrast in mechanical properties generates a weakening subsurface (Suneson, 2012). Core from boreholes in northern Oklahoma had evidence of hydrothermal alteration in Precambrian granitic basement (Schwing et al., 2016). Basement rocks are highly altered granitoid, alteration vary from diabase dikes rocks to hydrothermal alterations and pyrite emplacement. Basement rock in Osage County is described by the borehole Sunray S-3. Cuttings recovered at 980 m described a Rhyolite with mottled alterations (Denison, 1966).

The study area has suffered several tectonic events from the Ozark dome, which is an asymmetrical uplift, and two rift-like events, correlated with the Ouachita orogeny. The first tectonic event related to the study area is the collision of the Yavapai-Mazatal superior and Grenville Precambrian provinces, occurred in the late Precambrian about, 1.1 billion years ago (Keller & Stephenson, 2007; Alrefaee et al., 2012). The southern Oklahoma Aulacogen was the second tectonic rifting event that was not able to break up the North American continent (Chenoweth et al., 1968; Denison 1981, 1981; Nelson et al., 1982 ; Stein et al., 2018). The Bouguer anomaly map shows some evidence of the Precambrian rift anomaly (Figure 2-2.). The age span of this rift was from the Early to Middle Cambrian and began from Wichita Mountains and Southwestern Arbuckle mountains of southern Oklahoma. The formation of the Ouachita Mountains in southern Arkansas and southeast Oklahoma was the result of the Ouachita upward displacement; this tectonic event folded rocks from Precambrian to Pennsylvanian, the Pennsylvanian system was the period of tectonic activity and most of the mechanical changes on rocks. The potential data interpretation suggests a regime transition, from a passive to an active margin, this transition began from Late Mississippian and Early Pennsylvanian. This tectonic events in northeastern Oklahoma could have influenced the basement rocks (Nelson et al., 1982; Suneson, 2012; Khatiwada et al., 2013)

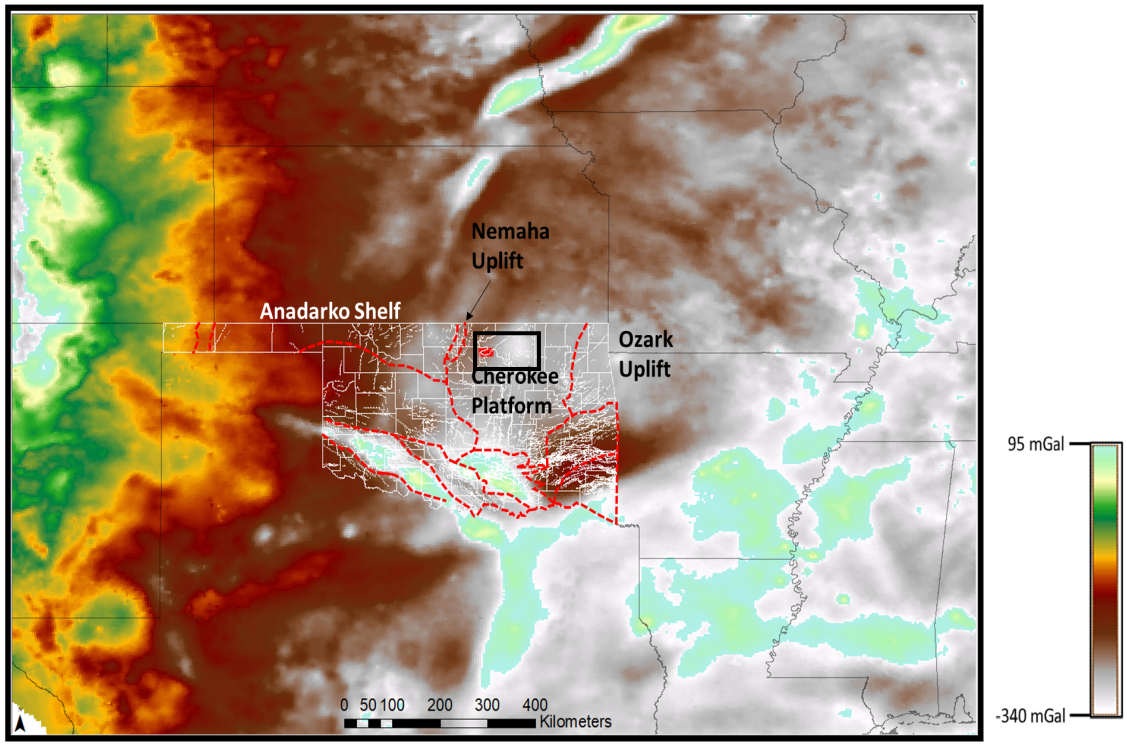

Figure 2-2. Bouguer anomaly map from the USGS national potential survey. Green values represent higher Bouguer anomalies, typically associated with shallower, more dense geologic units, such as granite rocks. (USGS, 2016)

The current maximum horizontal stress in this portion of Oklahoma has a preferential direction of N78°E, however, the stress azimuth changes with depth (Alt & Zoback, 2015), up to N80-90°E (Alt & Zoback, 2017). Stress magnitudes transition from strike-slip faulting in central Oklahoma to strike-slip and normal faulting in Oklahoma. The maximum horizontal stress azimuth is almost perpendicular with large faults observed on the Bouguer gravity anomaly map, the first vertical magnetic derivative interpreted, and faults interpreted on the seismic amplitude information (N 5-10 ° E). This could represent a possible explanation of the reduce seismicity in the area (Figure 2-3). Minimum horizontal stress is perpendicular to the maximum horizontal stress.

a) b)

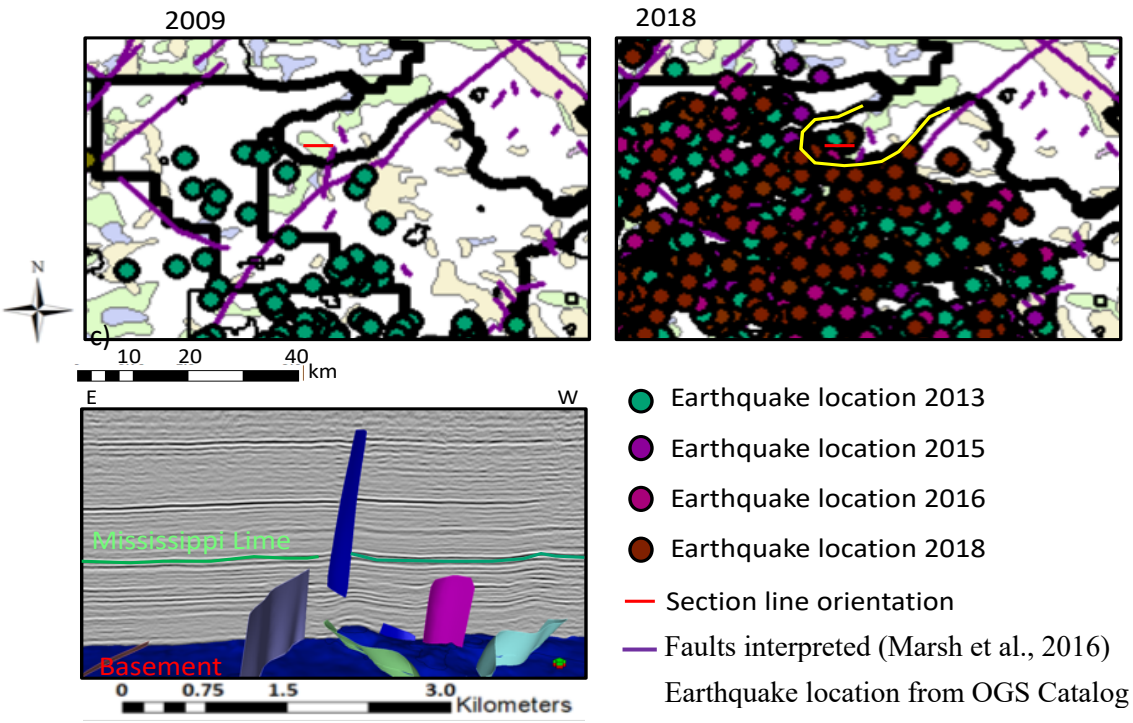

Figure 2-3. A), B) show the contrast in number of detected earthquakes with magnitudes M_w>2.5 between Osage County and neighboring counties. In the area of study only three events are reported in the OGS. C) Interpreted faults on the basement and upper strata. Fault direction is N 5-10° E.

2.3 Stratigraphic setting

One of the most important units, from the standpoint of view of the oil industry (Bass, 1940; Branson, 1958) in the study area is the Mississippi Lime deposited on a single third-order transgressive-regressive cycle (Benson, 2014). The difference of facies in the limestone is given by the paleo-topographic anomalies that controlled carbonate facies deposition, water level, and posterior tectonic forces caused diagenetic events that altered the top of Late Mississippian surfaces, leaving karst and sinkhole shreds of evidence that resulted in modified mechanical properties. The deposited carbonate thickness ranges from 70 m to 120 m in Osage County. The formation is a dark brown siliceous and dolomitic medium to fine-grain crystalline limestone.

XRD studies show deep marine element proxies, hence the rich siliceous nature of the limestone (Suriamin & Pranter, 2016). The dolomitic portion corresponds to a later diagenesis process. The late Mississippi gamma-ray response in the area depicts an intermix of terrigenous elements, Mississippian rocks are intermixed with large fragments of sandstone and shale from the lower Pennsylvanian, sand fragments consisted of angular to sub angular associated brecciated chert, tripolitic chert, unaltered limestone, sandstone and shale lying in a mud matrix (Zhang et al., 2016). The depositional environment represented by the sediment-distribution patterns in wireline log indicates that most chert-conglomerate reservoirs occur in coarse-grained deltaic system, a north-progradation system, composed of main distributary channels, secondary distributary channels, splays, and over bank deposits (Puckette & Al-Shaieb, 2008; Shepherd, 2009). Numerous basins report similar sedimentary rock interaction as the impact of paleo topographic heights weathered and meteoric groundwater (Lueschen et al., 2014; Johri et al., 2014; Goldstein & King, 2014).

The borehole response of Mississippi Lime in its chert unit appears as a low resistivity, low density (1900 – 2200 kg/m^3) and high porosity (25-37%) zone. The implication of low density and high porosity have a direct effect on the mechanical earth model. Also drilling events associated with this formation include partial drilling fluid losses. Reservoir characterization studies (Minor, 2013) have described a permeability range of 5-20 mD. This formation has a natural outcrop in northwest Arkansas; samples report up to 95% composition of silica (Liner, 2015).

The upper stratigraphic unit of the Mississippian system has to the south the Mermac formation, in the northern portion of Oklahoma. The origin of the Mississippian tripolitic chert is controversial (Manager et al., 2014; Bensons, 2014; Jennings, 2014; Mazzulo, 2013). The most

accepted hypothesis to explain the origin is related to diagenetic processes that modified the rich-silica water fed to the limestone, catalyzed the carbonate-silica replacement, and increased porosity, thus tripolitic chert is latterly variable and highly heterogeneous. From the standpoint of drilling, the Mississippian tripolitic chert is challenging. Mechanical earth modelling of the area in this study takes into account the lower fracturing pressure and lower pore pressure. The porous system and fluids in the porous impact the matrix skeleton and in general the effective measured medium, the increase of secondary porosity due to diagenesis promotes a convoluted porosity system that ranges in vugular porosity, fracture porosity, microcrystalline porosity. The different porosity systems account for more substantial oil accumulation in the porous system.

The Woodford shale represented the maximum flooding surface and was deposited in the Devonian. It is strongly radioactive due to high amounts of organic matter and has a distinct gamma ray log signature. The deposit of the Woodford took place during the Southern Oklahoma Aulacogen and was deposited upon predominantly carbonate sediments of the first stage of the South Oklahoma Aulacogen (Feinstein, 1981). The thickness of the Woodford in my study area varies from 3 to 30 m.

The Ordovician Simpson group represents a third-order sequence deposited on an HST, and it is composed of thin sand sheets interbedded with shale deposits and dolomite. Eventually, the sea rose rapidly covering the northeastern section of Oklahoma. Due to a rapid regression and the structural highs present in the area, shallow-water carbonates were deposited creating a thick carbonate self with bioclastic build ups. A global sea transgression created a carbonate drowning and deposited a rich shale sequence; secondly, a rapid sea regression in synchrony with structural

reactivation created a stable period for shelf-like carbonate deposits, most likely bioclastic accumulation with inter-crystalline porosity. This process resulted in sedimentary features such as karst, sinkholes and collapse structures in the Arbuckle Group. Porosity generally increased as a secondary process due to the subaerial exposure of the North American midcontinent (Thomas, 1963). Shallow carbonate deposit conditions were transformed by a steady sea transgression during the Middle Devonian, were thick deposit layers of shale that are known as Woodford shales.

The Arbuckle group is Cambrian-Ordovician in age and rests conformably on the Reagan sandstone in this portion of the study area. The Arbuckle group thickness ranges from 0-300 m (Bass et al., 1941; Denison, 1981; Reeves et al., 1999). In the study area, the thickness ranges from 100 to 300 m, where the thinnest deposits are from the lowermost Arbuckle beds, deposited on shore of the Precambrian islands, and have lower porosity and are rich in feldspars and quartz. This explains the high-velocity values of these units. Reeves et al. (1999), reported granite fragments ranging from fine to coarse grains, derived from old monadnocks (Reeves et al., 1999).

The Arbuckle formation, a hydrocarbon productive unit, is affected by the complex interplay of tectonic forces and other diagenetic events. Chenoweth (1968) described how subtle Precambrian basement movement changes sediment thicknesses of overburden layers. Elebiju et al. (2011), using a 3D seismic study conducted a study on basement faults, using 3D seismic curvature and potential field data; gravity and magnetic anomaly map to characterize the Arbuckle connection to basement faults. He showed amplitude seismic evidence of basement topography that controls and connects compressional strike-slip faults with the Arbuckle formation. Also, this work focused its analysis in Arbuckle and Mississippi Lime intervals, showing with seismic

attributes an overburden unit, however, the seismic attributes, and potential maps failed to explain the mechanical and stress conditions of these fractures and a quantitative background of the connection. The Reagan sandstone, a Cambrian quartz-rich sandstone overlaying an unconformity upon Precambrian basement altered (erosion and diagenesis) rocks, and represents the clastic unit covering the intricated basement topography of northern Oklahoma (Reeves et al., 1999). Reagan deposits during transgressive system tract (TST), basal sandstone was deposited to the north, and the complex interplay between tectonic and eustatic sea level controlled the dolomitic Arbuckle (Bass et al., 1941; Dille et al., 1956). The Reagan sandstone exhibits, according to wells analyzed in the area, a porosity range of 12-18-21 % (P10-P50 -P90). The Reagan sandstone in many parts of the south-central Midcontinent makes an outstanding reservoir (high porosity-high permeability) yet is sporadic and controlled by basement topography, thinning to structural highs in Osage County (Reeves et al., 1999); however, a minor gas fields are reported in Reagan formation.

The first study of the basement rocks in Northeast Oklahoma was in 1860 (Owen et al., 1860), linking the basement rock to lead-bearing rocks of northwest Arkansas. Ireland (1930) described basement in the Spavinaw outcrop in Mayes County as a coarse granite with some copper staining, and dated the basement as Precambrian, (Reeves et al., 1999). Moreover, 3D curvature attributes examined the irregular erosional upper surface of the basement, and the relation of the deep basement faults with hydrothermal fluid flows located on the Mississippi Lime of southeast Kansas (Goldstein & King, 2014). Deep basement faults connecting hydrothermal fluids as in southeast Kansas could be possible evidence of a low-density/low-velocity feature of constant thickness interbedded in the granitic basement, and wells that penetrated the basement

testified. Basement around Osage County is estimated (Elebiju , et al., 2011) around 1000 m to 3000 m. The basement surface, from the depth-velocity model in this survey is located around 980 to 1150 meters depth in this portion of the study area. Wells in the study area penetrated the basement at around 1100-1300 m; borehole Masham 1-15 reported the basement rock as granitic rocks with coarse to very coarse-grained quartz, orthoclase, coarse grains, and plagioclase feldspar and amphiboles, spread-out pyrite. Hydrothermal veins commonly deposit pyrite. Also, pyrite is a known mineral of metamorphic processes. In the early 1960's Denison, (1966) conducted a petrology and isotropic age determination of the basement and (McKnight & Fischer 1970) concluded the granitic basement and the mineralization was likely due to deep-seated hydrothermal alteration of limestone.

2.4 Dataset description

While borehole information provides a good vertical resolution (from 2 -15 cm), it has limited horizontal range of investigation (0.5 -2 m). On the other hand, seismic information provides a densehorizontal resolution, but a limited vertical resolution that is a function of frequency, depth, and formation velocity. As a data integration methodology, my objective is to establish a comprehensive relationship between the borehole information (mechanical earth model, petrophysics, drilling information) and the amplitude from seismic data using rock-physics.

2.4.1 Borehole information

In the study area, there are 234 boreholes drilled, that in conjunction with the acquired seismic data provided insight to characterize brittleness of the subsurface, and in particular of the

Woodford formation and Late Mississippian (Figure 2-4). Borehole information obtained from the IHS database was used to build a mechanical earth model. The total depth range of these wells goes from 320 m to 2500 m. These wells were drilled from 1899 to 2011. The available data includes information on well locations, completion zones, logs, operators, casing points, drilled fluid density profiles, extended leak-off test, hydrocarbon shows, rock description from cuttings, cores, geological formations, wireline logs, and formation tops.

Drilling information is essential for determining the ease of drilling, stress direction and mechanical properties. The borehole drilling process is unintendedly a mechanical rock test at every borehole. The subsurface rock properties are tested while drilling in terms of the hardness, temperature and pore pressure among other parameters. I analyze drilling operations from 98 wells to extract the following information; casing point depths, perforation depths, production formation depths, leak-off test, and mud density used while drilling. Different drilling parameters relate to various mechanical properties; leak-off test provided inference on the minimum horizontal stress magnitude since it correlates with fracture initiation. Mud-weight profiles shed insight into pore pressure and other drilling parameters such as ROP can be an indicator of brittleness/hardness. In the area, 81 wells are hydrocarbon producers, 50 wells produced from Mississippian units, 13 wells produced oil, the remaining wells produced gas, average initial production in the Mississippian unit is 50 oil BPD with 200 BWPED. Gas to oil ratio (GOR) for wells in the area range from 2:1 to 15:1, depending on type of drilling. Typically, horizontal wells have a much more favorable production rate than vertical wells, around 2:1 for an average of 600 m extended the length. 31 wells out of 81 wells are producing from different stratigraphic units. Only seventeen wells of the 81 produced in the area are plugged and abandoned. In the area, 5 wells are water injectors wells,

and two wells are injecting to the Arbuckle formation. From the 234 wells in the study area, 200 overlap the seismic amplitude data. This large number of wells in the area results in a borehole density of 3 wells/km^2. The wireline data came from the wells in the area as a part of the IHS database. I use geophysical logs for formation evaluation, the log dataset I use consists of a combination of digital wireline logs and raster logs (115 wells). The logs available for this study are caliper, gamma ray, spontaneous potential, micro-resistivity, and double lateral resistivity tools.

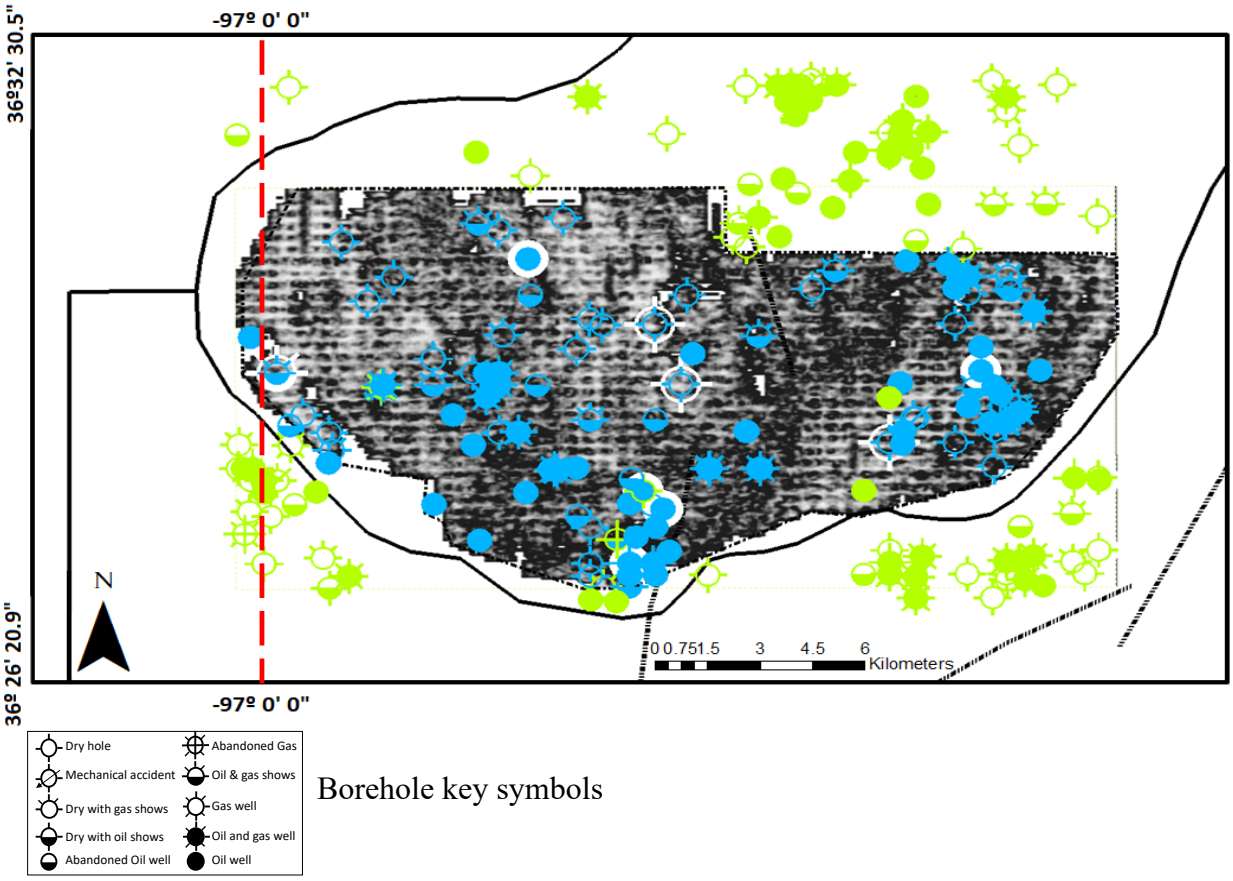

Figure 2-4. Boreholes drilled in the study area. Approximately two hundred boreholes are drilled inside the amplitude seismic information (cyan boreholes), the remaining of boreholes are outside the amplitude information (green symbols). White symbols overlap with blue symbols, but the difference is the presence of wireline logs

In Figure 2-4, the distribution of borehole information helps to contextualize the importance of wireline information. While with symbols have a full suite of wireline data (gamma ray, density, velocity logs), its properties/information can be expanded to the green symbols are boreholes that contributed by interpreting the drilling and completion information with formation tops. Boreholes inside the amplitude data (Cyan symbols) are prioritized to build the mechanical model. Borehole outside the survey, also contributed to the model due to the fact the relative null structural difference or flatness of the horizons.

2.4.2 Seismic dataset

The Ceja seismic volume has an irregular rectangular shape as necessity of the processing; however, the amplitude information is bound by the Osage County limit. In Figure 2-4, the extracted amplitude information corresponds to a time slice at 200 ms to exhibit the acquisition footprint. The footprint ought not to be confused with any geological item. It is essential to discern the depth limit of its effect to not interpret it as a sedimentary or structural feature.

The Ceja seismic survey has an area of 94 km^2. Seismic information is used to and understand the interaction between sedimentary features of Paleozoic sediments and the Precambrian basement. The seismic survey has a two-second record-length sampled at every 2 ms and has a bandwidth frequency from 15 to 92 Hz, with a dominant frequency of 50 Hz. Seismic resolution is a function of frequency and depth, in addition is affected more particularly by the velocity of the sediments. Seismic information suffers from acquisition footprint up to 100 ms (Figure 2-4).

To estimate the vertical and lateral resolution profile, I use the dominant frequency of the shallowest reflector for the dominant frequency of the basement, that is 90 Hz to 18 Hz respectively and the velocity information extrapolated from borehole velocity information to the data was conditioned to improve interpretation and subsequent amplitude extraction and further amplitude analysis such as trace amplitude attribute. I create the velocity distribution from wireline sonic log information. The information included up to 200 meters in the Precambrian basement. This distribution is 2700 m/s to 7200 m/s. Using Rayleigh vertical resolution criteria, defined as wavelength over four, I estimated the vertical resolution ranges extends from 20 m to 120 m (Figure 2-4). The average lateral resolution is 50 m, from the 90 m resolution at one-kilometer depth with a frequency of 20 Hz, to 200 meters depth with a dominant frequency of 70 Hz.

The seismic volume was provided by Osage Nation has an In-line and Cross-line distribution from 1-400 and 1-290. The inlines and crosslines have a north-south, and east-west direction, common midpoint fold is 30.

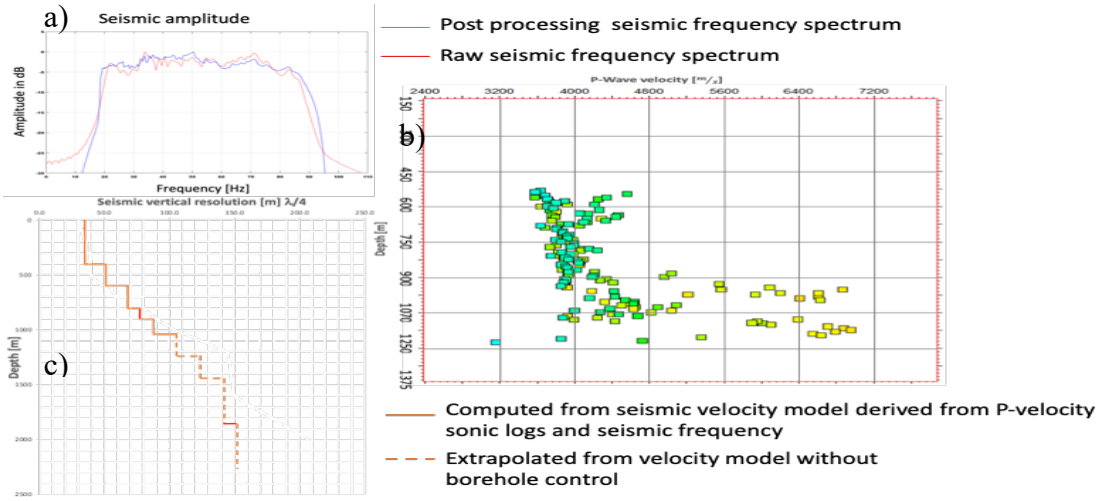

Figure 2-5. A) Amplitude spectrums of the 3D seismic frequency distribution. Red curve is the power spectrum from the legacy processing. B) shows the P-velocity distribution from borehole information. C) Vertical resolution plot from frequency distribution and P-velocity.

The seismic information I use in this study has a narrow frequency distribution, and the lack contribution is low-frequency impacts the structural character on the seismic information. The original amplitude spectrum (Fig. 2-5a) has a wider range but higher frequencies (above 90 Hz) represent seismic noise and low frequencies (below 10 Hz) as well. The blue line represents the amplitude spectrum after conditioning (band-pass filter and radon transform). The frequency bandwidth is restricted from 15 Hz to 90 Hz; however, the seismic conditioning yielded a sounder amplitude distribution. From borehole information, I extract low-frequency component of the P-wave velocity on the panel b), it exhibits a gradual increase on the velocity on the Cambrian sediments. There is a significant increase in the Precambrian rocks which corresponds to basement velocity composed accordingly to core reports to pink to pinkish granite, possibly with metamorphic alterations. I extract from the time-to-depth frequency attribute and velocity the vertical seismic resolution on Fig 2-5c.

2.5 Methodology and results

From shear and compressional sonic logs, I derived the mechanical properties, but also from the geomechanical model. In this study, only thirteen boreholes were used to derive a rock-physics model elastic constant, but more than 200 drilling parameters feed the geomechanical model to estimate, elastic properties. In this methodology I integrated the high number of boreholes drilled to extract useful information, especially in areas where wireline information is not available.

I interpreted formations and faults in this project using a combination of seismic principles and seismic attributes; I incorporated the formation tops from the dense-well control using the calibrated time to depth relationship constructed for the area.

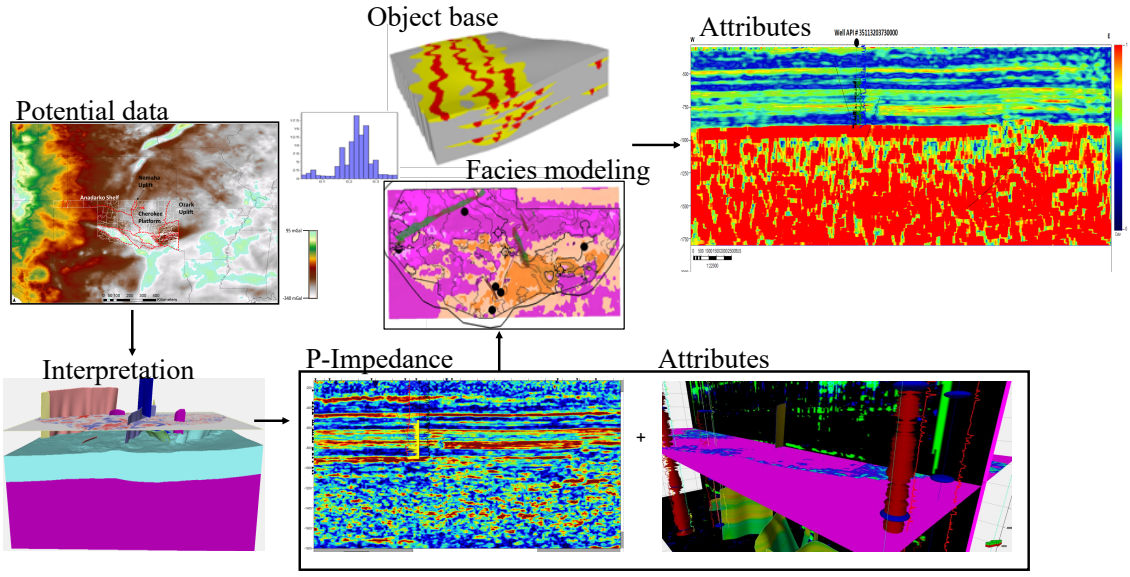

Figure 2-6. Methodology workflow to integrate data from different streams of information. Potential geophysical data assist interpretation. The selection of discrete facies helps to determine the distribution of P-impedance and attributes.

This velocity model was constructed firstly with sonic information of nine boreholes distributed throughout the area (6). Secondly, I trained an artificial neural network to compute derived P-wave velocity from resistivity logs where the P-wave profile was absent. I derived resistivity information from other boreholes, but also the volume of clay, density, and porosity. These factors are the most important factors when computing P-wave velocities (Avset et al., 2005; Vanorio et al., 2008). I used blind wells to corroborate the quality of the trained network. I derived a pseudo P-wave velocity profile and compare the derived synthetic log. The correlation yielded a R^2=0.94 correlation on the predicted sonic log from resistivity and other logs. This value resulted

from cross-correlating the predicted sonic to the in-situ sonic. A schematic of the workflow is present on Figure 2-6.

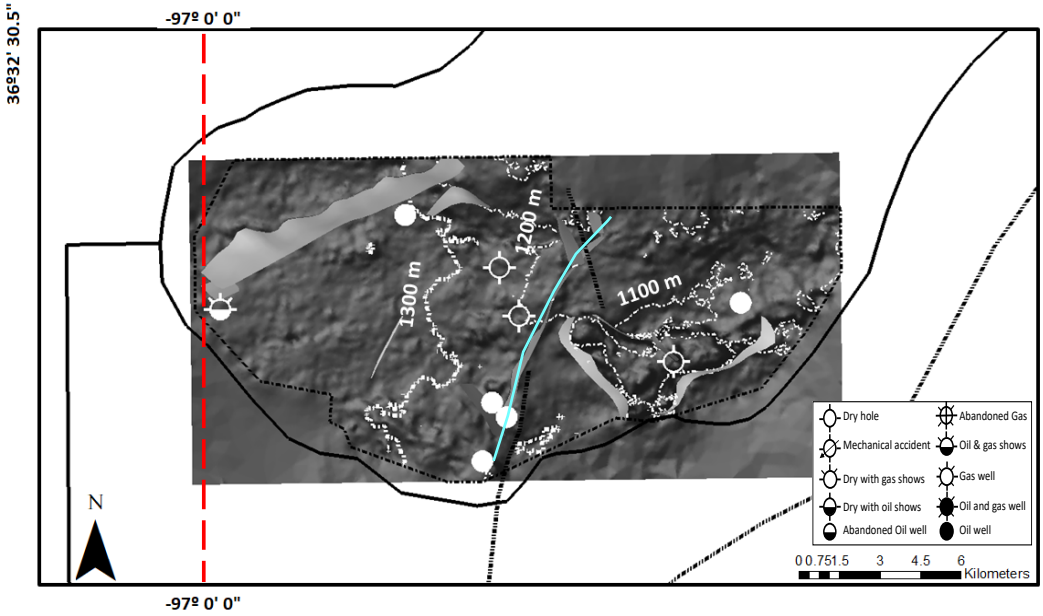

Figure 2-7. Precambrian basement surface used in the geo-cellular model along with the boreholes with sonic information that helped translate the basement location from time to depth.

The depth range of the top basement in this portion in Oklahoma varies from 900 meters to 1300 meters. I used the P-velocity profiles from boreholes in Figure 2-7 to build the velocity model to convert from time to depth the basement surface. The gray items on the basement are interpreted faults. Faults to the west of the survey extend thru shallower stratigraphic units, including the Arbuckle, and Mississippi Lime. The fault at the center (cyan line) of the survey correlates with the faults reported on the OGS report (Marsh & Holland, 2016). Boreholes white symbols have velocity and density wireline information. These boreholes are used in the acoustic impedance seismic inversion. Also, these boreholes help build the 1D geomechanical model which

was later on used to guide the mechanical properties using the neural network and geocellular model that resulted in facies classification.

Formation tops were picked from the borehole reports and well log response. I used the Oklahoma Geological Survey wireline log catalog (OGS) to correlate borehole gamma-ray response type of each formation top to pick wireline formation tops. I computed synthetic seismograms using a zero-offset ray-tracing algorithm to evaluate and correlate well log and formation tops response in depth to seismic information in time. I first used a synthetic zero-phase Ricker wavelet with a dominant frequency of 30 Hz to perform a convolution with the reflectivity coefficients from the impedance at each borehole location. This helped to translate wireline picks into seismic representative picks. From the synthetic seismic borehole response, I concluded that the most representative events, such as erosion, carbonate limestone and sand deposits. That is that its character is evident at borehole scale and in the seismic information, correspond to; Mississippi Lime, tripolitic chert, Woodford, the Arbuckle group, basement top and a low-velocity layer 100 meters below the top of the basement (Figure 2-8).

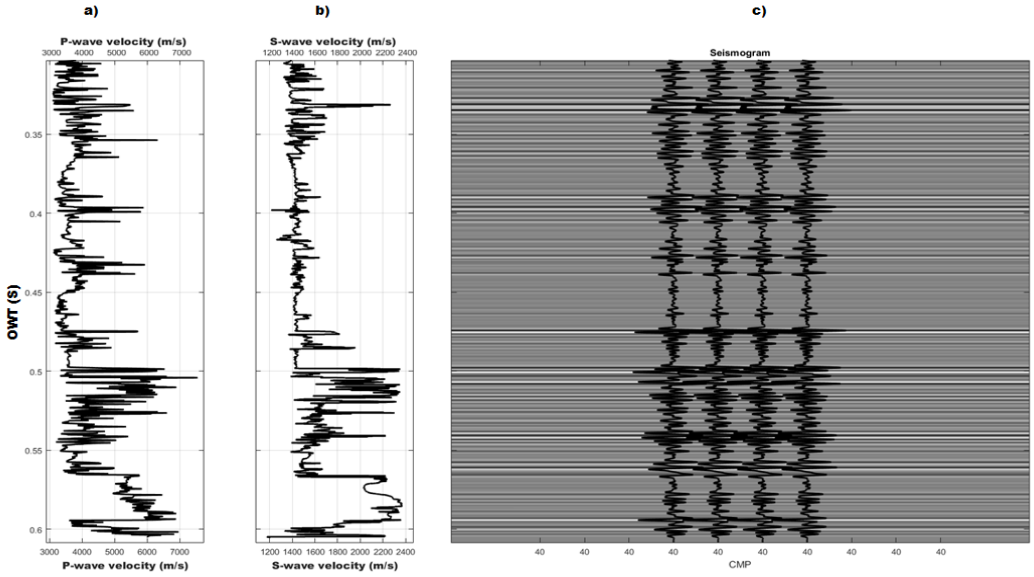

Figure 2-8. A) Borehole API: 35113200030000. A) P-wave B) S-wave velocity help derive the reflectivity coefficient information. C) The reflectivity coefficient is computed from the P-wave velocity profile. C) The synthetic trace in the left panel is the result of the reflectivity coefficient profile convolved with a 35 Hz Ricker wavelet.

The convolution of reflectivity series in Fig 2-8c with a zero-phase wavelet provides sharp reflections from the principal lithologies, these reflections are also present on the seismic survey, however it is not as clear as in the ray-tracing. One of the reasons is that seismic processing was accomplished under the assumption of having a ubiquitous invariant time wavelet; however, in reality, this wavelet is time and laterally variant due to attenuation of highly heterogeneous shallow strata local site effects, a product of different acquisition parameters that is exhibit in an shallow depth slices with a strong acquisition footprint I estimated different wavelets at each borehole location to correlate and estimate time to depth relationship and extract wavelet at the time-range of interest (average 200 to 900 ms). The selected well-tie showed that a 0.72 correlation is achieved with an eight-degree phase delay wavelet of 140 ms length. (Figure 2-9).

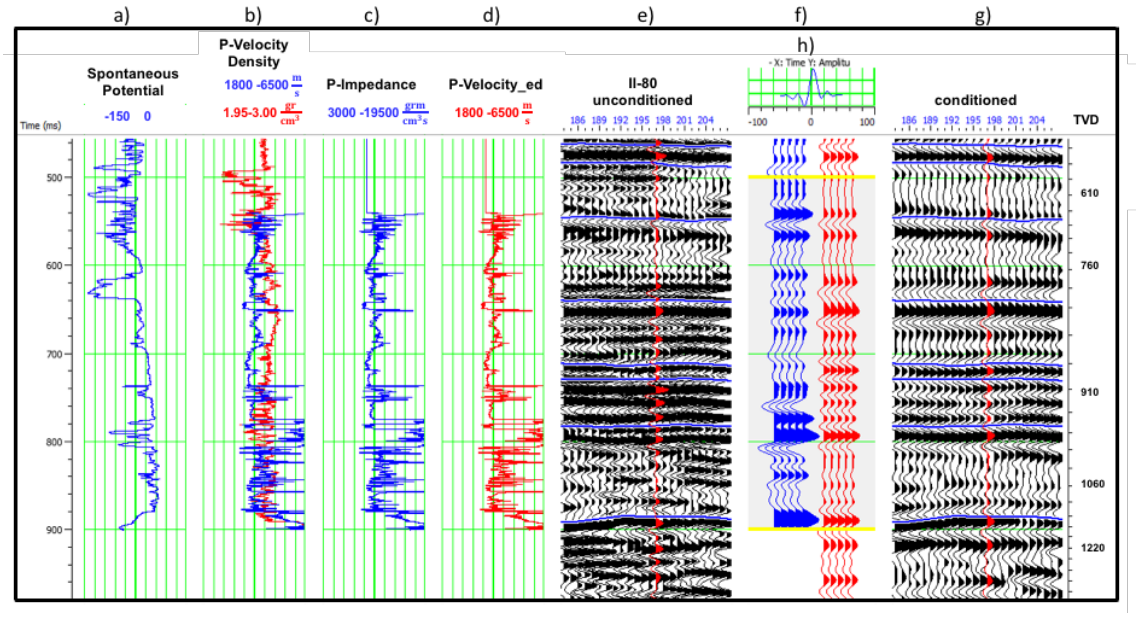

Figure 2-9. Well-tie and seismic comparison between the conditioned stack and the legacy amplitude information. A) SP log as a lithological indicator. B) P-velocity and Density log used as mechanical and lithological logs. C) P-Impedance is the product of P-velocity and Density. D) The equivalent P-velocity after time-depth drift correction. E) The legacy seismic information on the borehole position. F) The extracted wavelet and the synthetic seismic trace used to correlate the observed data with the synthetic trace. G) The conditioned seismic trace. H) The wavelet extracted from the seismic data (8 degrees phase).

Figure 2-9 shows the contrast of using legacy seismic information versus conditioned seismic information to perform time to depth matching. I used the lithological wireline indicator in the Fig 2-9a to correlate the lithologies to its seismic representation and position in time. Due to the high variability of wireline logs available, in this figure I chose spontaneous potential. The spontaneous potential log helps to discern lithologies. The basement response is clear across the wireline information.

Figure 2-9b shows the P-wave velocity and density logs. P-impedance plotted on Fig 2-9c is the product of density and P-wave velocity. To honor the seismic response of lithologies and its position on time, the time-to depth correction represents a velocity change, this edition in the

velocity profile should not exceed 20 % difference versus the original velocity profile. The Figure 2-9d is the product of the edited P-impedance curve after the time-to-depth computed shift from the correlation of the synthetic trace. On Figure 2-9e shows the raw seismic data, it is observed the high frequency character on the seismic trace, this makes difficult a clear identification of the basement. Figure 2-9f shows the extracted wavelet, an eight-degree wavelet that is used to generate the synthetic seismic represented by the blue trace. The cross-correlation coefficient between the synthetic seismic (blue trace) and the conditioned seismic (red trace) is 72 %. The correlation coefficient indicates how similar the synthetic trace is with the observed seismic. A high correlation can be interpreted as a correct time-to-depth relationship. Drilling cuttings from the borehole reported granite cuttings. The borehole drilled twenty meters into the basement and stopped.

Ray tracing is an essential tool for the exploration geophysicist since it provides the reflection characteristics of the main lithological changes, and what is its response to the seismic domain. For this borehole, most individual reflectors correspond to tripolitic chert, Arbuckle group, Woodford, basement top, and low-velocity interval inside the basement. This low-velocity is located at 1160 meters, 150 meters below the basement top. I used a Backus filter to reduce the variability of the acoustic and density borehole log responses and re-computed the seismic response to account sampling frequency difference of log information and seismic records, add random noise to have a closer response to the observed seismic data.

After filtering the borehole logs, only three events are represented at a seismic resolution; the Mississippian/Devonian top, represented by Mississippi Lime, Ordovician/Devonian,

represented by the Arbuckle group and the Cambrian/Precambrian contact. At this frequency, the low-velocity layer inside the basement is not discerned since it is below seismic resolution, which explains the reason it is not evident on seismic information (Figure 2-10).

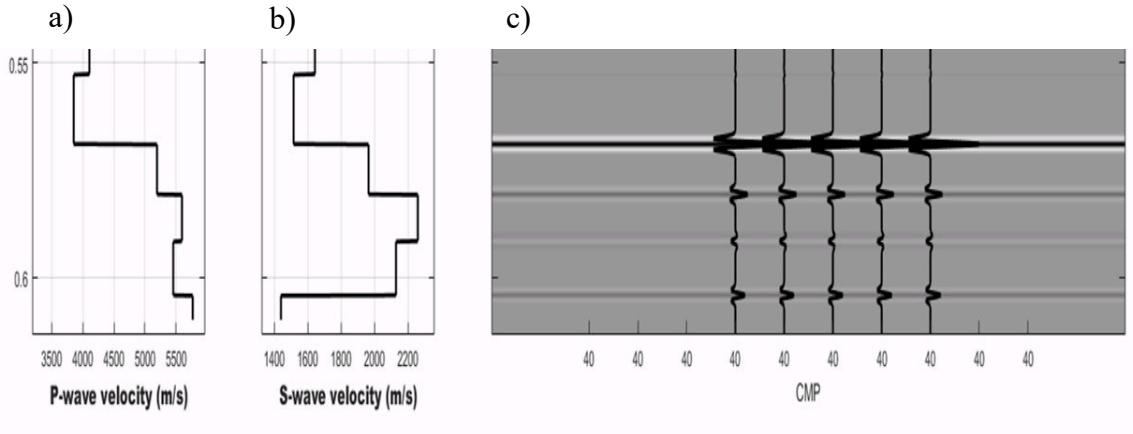

Figure 2-10. 1-D Ray-tracing at seismic frequency from borehole information. A) P-wave profile. B) S-wave profile. C) Equivalent synthetic seismic response at 20 Hz resolution, which is the resolution of seismic information basement depth.

To generate the figure above, I Backus filtered the P-velocity and density wireline logs to compare the ray trace response at the wireline log resolution against the seismic resolution. The seismic frequency at this depth is close to 20 Hz. The P-wave and density logs show a clear response. The synthetic seismic basement top response using ray tracing is a clear peak, the basement response is inside the seismic resolution. Although, the internal basement low-velocity anomaly has a vertical thickness of sixty meters, however at the seismic resolution it shows a null response. Despite the low-velocity anomaly, it is not evident at seismic resolution; it can be detected using the geocellular model. The vertical size of the geocellular model is 25 meters and combined with the P-impedance that enhances the vertical resolution the effect is observable.

The petrophysical model I used to compute volume of clay, water saturation and porosity is the dual water model, this is a modification of the Simandoux equation. A porosity trend from Zoback (2012) as guide, a tortuosity exponent of 0.4 (unitless) a constant initial bound water of 40% (due to the high water cut) and I used shallow and deep resistivity as inputs for computing cementation index, water resistivity, shale resistivity (Athy,1930, Finkbeiner 2001, Zoback et al., 2001). From P-sonic and density I computed the effective and useful porosity. From petrophysical interpretation charts (Schlumberger 2008) I used equivalent resistivity.

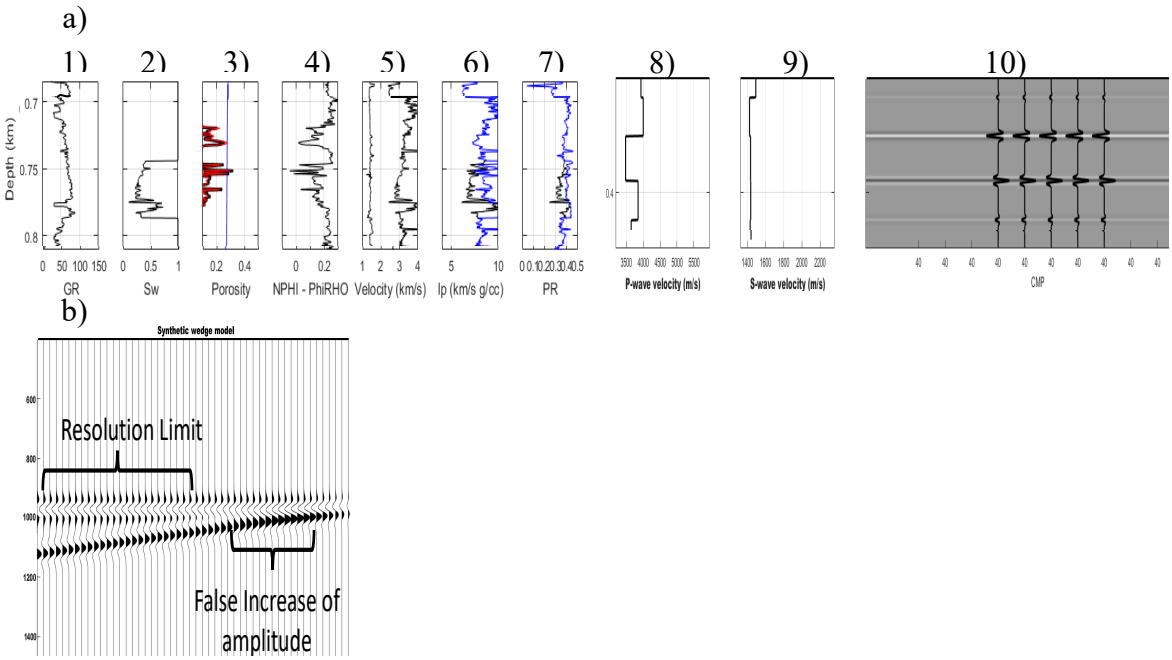

Figure 2-11. A) Petrophysical curves to represent the model and fluid substitution in the Mississippi Lime. First panel shows the GR variability and second profile is water saturation curvature. B) is the synthetic seismic wedge model to investigate the tuning thickness.

The petrophysical model and wireline logs shown in Figure 2-11a-1. exhibit the gamma ray response with a thin dolomite bed at 780 meters. Figure 2-11a-2, exhibit a low water saturation, this model produces gas and condensate. The effective porosity profile for this borehole shows the intraformational seals, a high porosity interval followed by a low porosity and continued by a higher porosity lithology from 720 meters to 790 meters. The total porosity, a model that contains the porosity from neutron and density logs shows a higher porosity and a more continuous porosity profile than the Fig 2-11a-3. The profiles for the mechanical parameters (Fig. 2-11a from 2-11a-4 to 2-11a-7) helps to use Batzel modified version of Gassmann fluid substitution (Simm, 2007).

In Fig. 2-11b I used the tuning thickness definition to evaluate the horizontal and vertical resolution, for this I used the ray tracing with a 20 Hz wavelet and build a wedge model to evaluate the reflected model. The results helped to evaluate amplitude sensitivity to tuning. This plot shows us the that seismic events below 35 meters will exhibit a false increase in amplitude.

The porosity distribution, as determined from of nine boreholes shows the variability in the porosity systems and the lithologies. The three different porosity distributions agree with the principal facies. Mudstone facies shows a porosity distribution from 2 to 5%. Fractured mudstones and grainstones are lithologies with porosities from 10-15%. The highest porosities correspond to diagenetically altered mudstones into cherts. Dolostones would be less than twelve percent (Figure 2-12).

This plot shows the different porosity systems present in the dataset. The maximum concentration porosity could potentially correspond to fracture porosity. The second-high porosity concentration is most likely associated with vugular porosity and diagenetic altered cherts. The histogram distribution better shows the high variability of the porosity systems, in this reservoir

(Fig. 2-12b). The bi-modal distribution of the porosity distribution exhibits the difference in porosity systems.

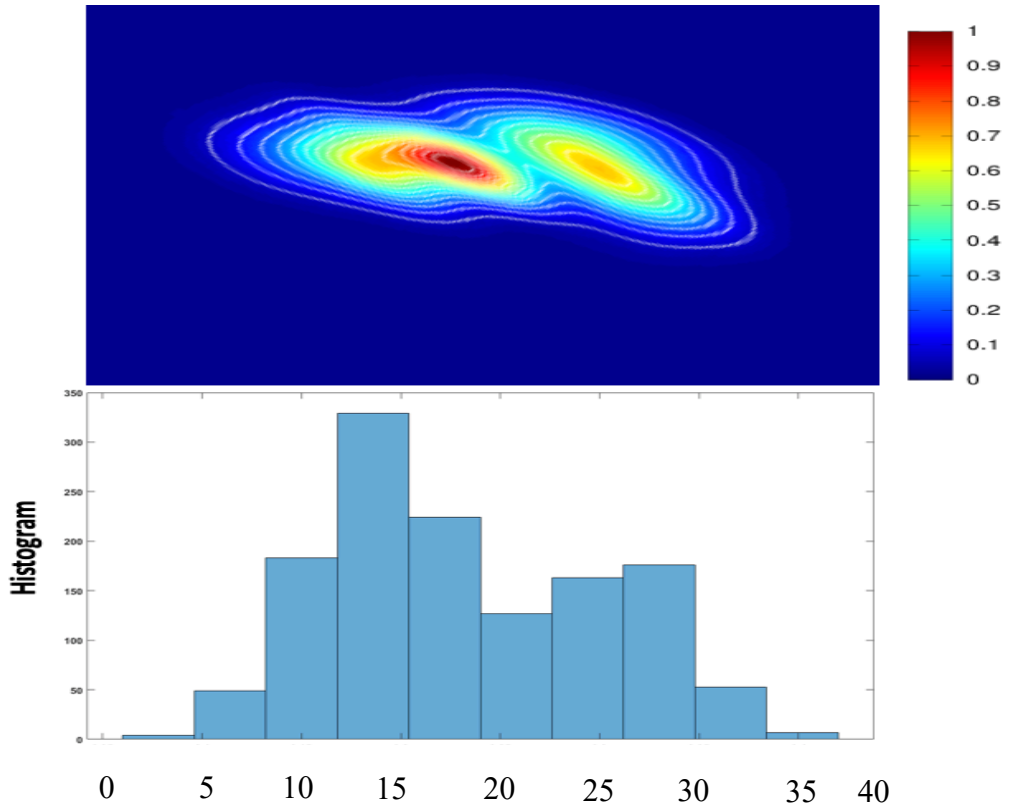

Figure 2-12. Porosity distribution on the Mississippi Lime. A) Density distribution function. B) Histogram distribution.

It was important to discern the extent of the resolution and the representative picks of the stratigraphic column that are evident on the borehole and the seismic. From this analysis I defined most of the apparent faults first using the 3D amplitude seismic dataset and secondary faults arose from combining trace attributes. The importance of defining the tectonic framework is to identify the skeleton of the area. Faults provide the structural framework for the sequence stratigraphy and latter examinations. I bandpass filtered seismic data to image, with more confidence, fault plane reflections and enhance their response on seismic attributes. The suitable bandwidth, chosen from

the filtering stage guides the selection of the attribute response, since undesired noise is removed making the reflector offset and dip change clearer. The multi-trace attribute is a valuable tool to guide the interpretation and the mechanical properties extrapolation. The attributes I used to assist and guide the interpretation were RMS of amplitude, the variance of amplitude, ant-track, chaos, envelope, energy ratio, principal curvature, principal component, and fault likelihood (Figure 2-13). These attributes are known from previous studies to aid in structural interpretation (Marfurt et al.,1998; Gersztenkorn & Marfurt,1999; Marfurt, 2006; Marfurt, 2014 ; Hale, 2013; Wu & Hale, 2016).

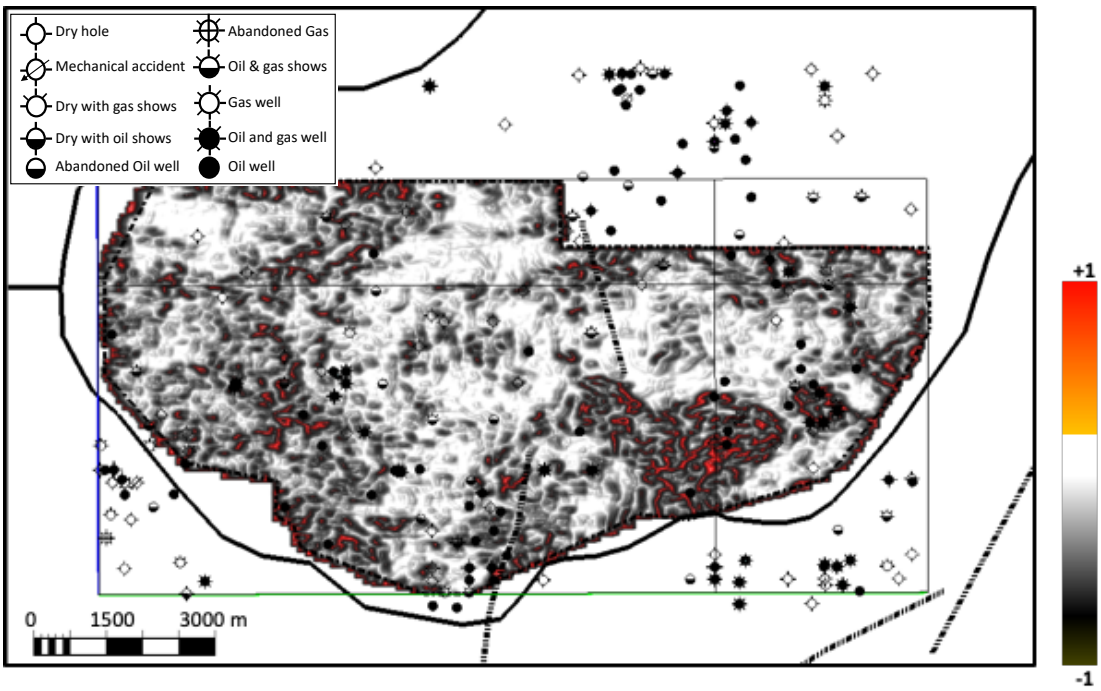

Figure 2-13. Maximum curvature attribute extraction on top of the basement.

The curvature, that can be mathematically expressed as the quadratic fit from a grid measurement as: $z(x,y) = ax^2 + cxy + by^2 + dx + ey + f$. Where the most-positive and most-negative curvatures are defined as:

$$k_{pos} = (a + b) + \sqrt{(a - b)^2 + c^2}$$ **Equation 1**

$$k_{neg} = (a + b) - \sqrt{(a - b)^2 + c^2}$$ **Equation 2**

Were a and b, c are the sides of the search grid defined on the quadratic surface z(x,y) (Roberts et al., 2011)

One interpretation of the curvature attribute on a basement, is that high curvature values are ought to be a compact and brittle materials (Aktepe et al., 2008) is that a close to zero value represents horizontality and higher compressibility. The positive curvature on the basement top is interpreted as lower brittleness index. The basement structural high in the southeast of the amplitude seismic survey enclosed by the green light shows a positive curvature on the basement due to a transpression event on the basement. i.e., a strike-slip movement with a compressive component.

While performing seismic trace attributes, I discarded zones, both vertical and horizontal, due to lower signal to noise ratio, also attributes that showed dependency linearly and which results showed ambiguity, this was done to reduce false interpretation by discerning constant features present in independent trace attributes from artificial geological-like event product of seismic migration or noise remaining from the filtering step.

I applied fault mechanical stratigraphy once the interpretation of the visible faults was completed. Fault mechanical stratigraphy defines the media as a perfectly elastic isotropic media. Thus, I relate the age of the fault and the strata using Steno's law of superposition (Figure 2-14).

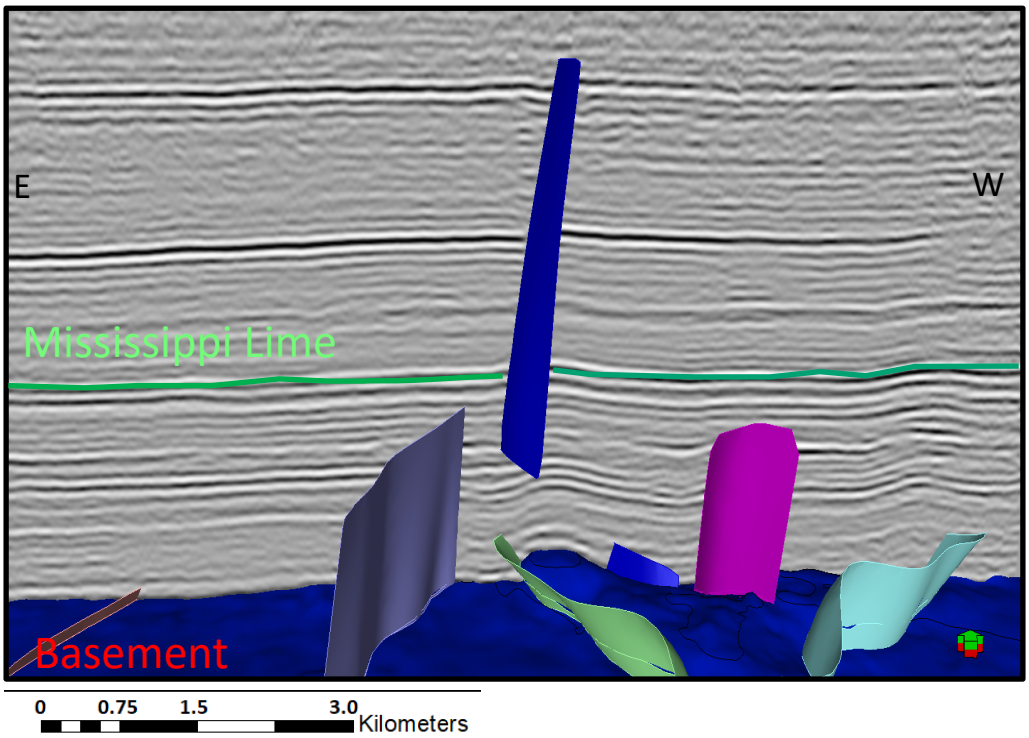

Figure 2-14. Representative tectonic framework on the seismic generated from seismic interpretation. Different fault colors represent the variety of faults orientation, depth and age. Green horizon represents the Mississippi Lime. Blue surface is the basement interpreted in the survey and affected by the tectonism. The vertical extension of blue and violet faults suggests a possible connection between shallower strata and the granitic basement.

Once the age of faults is assigned, older rocks appear to be stronger and less prone to brittle deformation (Pigott, et al., 2016). This concept is important because once I have converted the interpretation to depth, I relate the normal stress to the bulk modulus as a function of depth and its effect on faults as:

$$\boldsymbol{K(z) = \frac{-P}{Ev}},$$ **Equation 3**

where K is the bulk modulus, E is the Young's modulus and, v is the Poisson's ratio. Ev represents the volumetric strain. If we consider the derivative of volume dV to represent small relative changes of volume (V)

$$\boldsymbol{Ev = dV/V},$$ **Equation 4**

In this case, v is a fixed parameter to the lithology dependent on transverse deformation, unconfined compressive strength (UCS) and internal friction angle. However, the Young's

modulus is related to the uniaxial compressive strength of the rock. I interpreted the basement surface location from borehole information and following the basement amplitude response in the seismic data where possible. Depth to basement is around 900 meters to 1300 meters and tectonic style of the area created almost vertical faults. This resulted in two different diagenetic events that influence on the stratigraphical column. The first event potentially created water input thru the Pennsylvanian/Mississippian unconformity. The second diagenetic event was probably during the Ouachita orogeny, which created faults and possible fractures that connected the basement with shallower stratigraphic units. As a consequence of this orogeny, hydrocarbons migrated from Woodford shales deposited on the south (Higley et al, 2013).

In my study area, eight wells extend into the Precambrian basement, and three of them drilled up to 300 meters into igneous rocks. In multiple structural zones, where the imaging quality is not good enough, gravimetric data aided the interpretation and set the geological trend to guide interpretation of the deeper faults; this is particularly useful where reflection events are challenging to image with conventional migration algorithms.

I interpreted the seismic data using sequence boundary definitions. Sequence unconformities are; top-lap, erosional truncation, apparent truncations, donwlaps and onlap (Vail & Mitchum, 1977; Posamentier & Allen, 1999). Bundled elements of these unconformities define the lithostratigraphic units and a conformable succession of genetically related strata. Also, sequence stratigraphy is a powerful method that takes into account relative sea level, tectonics, unconformity surfaces, substrate and marine, and riverine inputs (Slatt, 2013). Sequence stratigraphy calibrated with wellbore logs provides lithostratigraphic units observed in the well

control, well-tie correlate time significant reflectors in the seismic data to the borehole response. Using sequence stratigraphy, I can predict or translate seismic clinoforms to coarsening grains closer to the deposition input and finning towards less energy system (Figure 2-15).

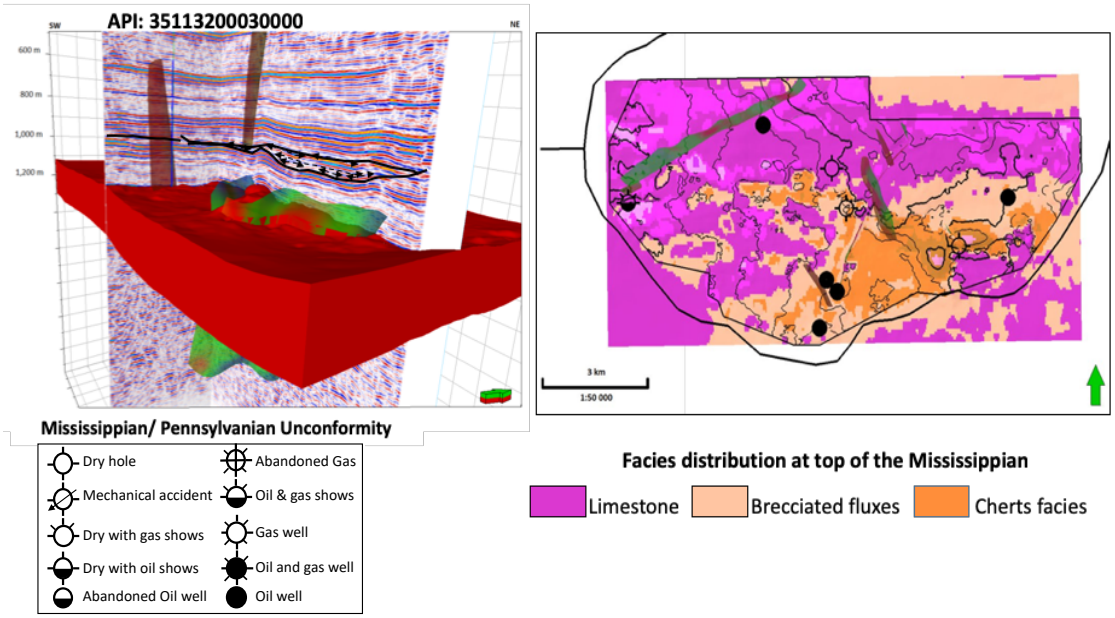

Figure 2-15. A) 3D Seismic inline and crossline to show down lap terminations. These patterns guided the mechanical property extrapolation. B) Discretized facies distribution on top of the Mississippi Lime. The mechanical pattern represents the three different lithologies observed in the boreholes.

The classification was done using type of terminations on top of the Mississippi Lime. Attributes aided the interpretation in confirming lateral extension on lithology-like features. Coherence and variance attributes were extracted on the Reagan Formation. From my observations I concluded that the Reagan sandstone showed in attributes the LST sequence where basement highs control the meandric systems observed on RMS volume. Curvature and chaos attributes were computed to identify sinkholes and karst futures in the Arbuckle group. The Arbuckle formation presents two configurations, toplaps against the basement and sandy deposits overlaying the Reagan sandstone. The combination of these attributes helps discern model mechanical facies distribution for the varying facies.

The Arbuckle onlap displays truncations against basement highs. The Arbuckle group is Cambrian-Ordovician, with the carbonate presence suggested a sea-level regression to Middle Ordovician (West, 2015). Enhanced porosity in a carbonate matrix suggests erosion and weathering of the Arbuckle group, this corresponds to a major-rapid interregional sea regression (Roy et al., 2013). Rapid regressions effects are commonly collapsing structure, karst and sinkholes, exemplified by seismic attributes (Curvature, Chaos). By the time Arbuckle group is deposited, Oklahoma was a sizeable thick shelf, comprised primarily by thick and extensive shallow-marine carbonates interbedded with thin marine shales and sandstones (Denison, 1981). The Arbuckle Formation is also affected by fault and fractures in the basement. Mapping fractures from attributes can be inferred by analysis of anomalous curvature, proximity to faults. The impact of fractures on attributes can be detected by anomalous low impedance, increased scattering, lower frequency response. Fault likelihood is an attribute derived from self-oriented filters and the energy ratio and semblance attributes (Hale, 2013; Wu & Hale, 2016). The faults depicted by the fault likelihood attributes, correlate with the interpreted faults in the OGS report. The fault direction in this seismic volume is close to north to south (Figure 2-16).

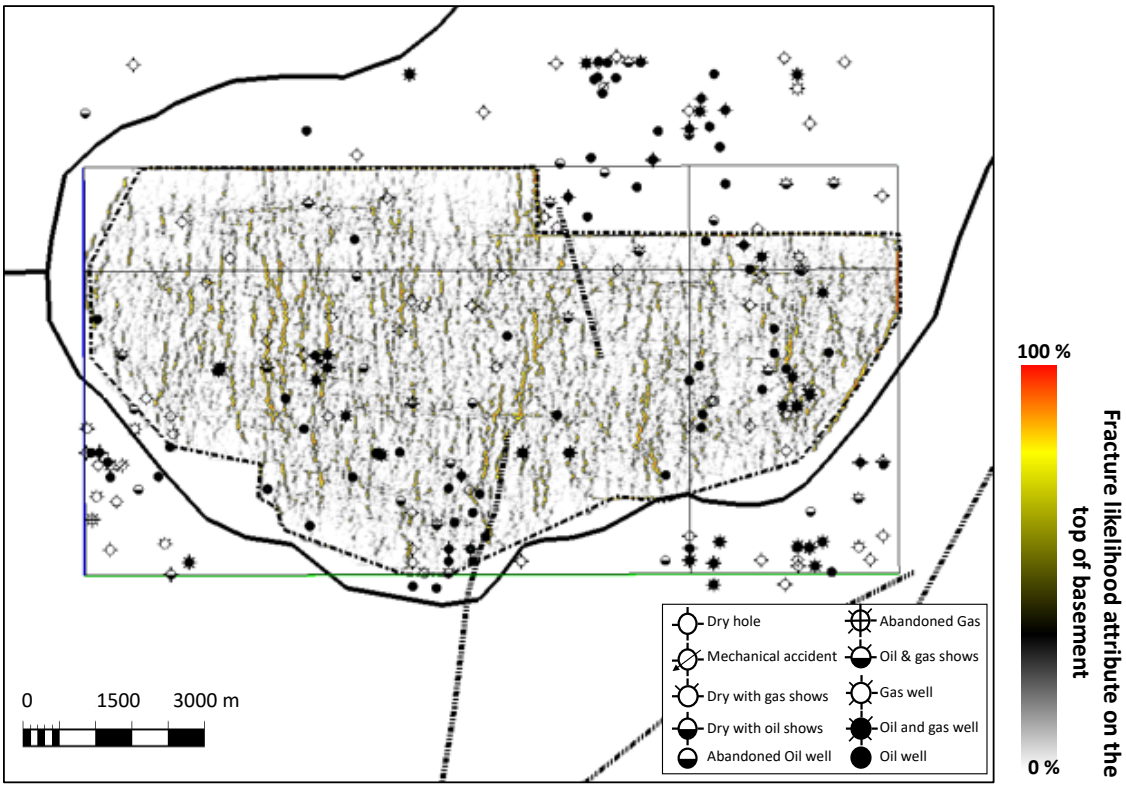

Figure 2-16. Fault likelihood attribute on the top of the interpreted basement. The attribute shows a North to South fault set trend on the top of the basement.

It is noteworthy from Figure 2-16, the correlation on the main fault in the center of the Ceja survey with the documented in OGS geological report (Marsh & Holland, 2016). By including more attributes into the facies classification, fault-fracture distribution could be better discerned. A zone close to a fault would be potentially weaker or less brittle in contrast to a high brittleness zone. The areal fault density on the top structural high is higher to the west. At any rate, the Arbuckle is placed in an environment that was favorable for hydrocarbon preservation, observed by gray to dark gray limestone, indicative of restrictive riverine inputs created by isolated sinkholes (McCullough & Slatt, 2014). During the Upper Ordovician, a significant flooding surface stage was onset which allowed the Sylvan shale deposits over the Viola lime and Simpson groups; the

latter is characterized by a higher energy environment (Keller & Stephenson, 2007) variance and spectral decomposition helps identify the sandstone systematically interbedded with shallow marine limestones (Liner, 2015). Hence, mechanical stratigraphy was implemented to discern the difference using seismic attributes as guides. I guided the lithology indicator by understanding the depositional environment. I correlated the differential compaction detected in the seismic attributes to identify the difference in the irreversible volume change that rock suffer under pressure, i.e., overburden pressure.

Attributes and identification of volumetrically strained areas helps to extrapolate bulk modulus in the modeled facies (Roy et al., 2013). Channelized facies, for example, are identified by their meandric behavior. Positive curvature anomalies over channels features indicate that these channels are filled with a lithology that is less compactable than the surrounding matrix, suggesting the presence of sands. On the other hand, flat structures suggest a more brittle behavior. To discern compaction patterns and correlate them to the geometry of reflectors (oblique or flat) I used a differential compaction correlation, this attribute uses a spatial gradient correlation of dip curvature and strike curvature, energy ratio and envelope (Figure 2-17). Low values suggest incompressible materials, hence more brittle lithologies deposited, values close to one means compaction or soft material, that is clays and clay-supported rocks. The incompressibility attribute has a value range from 0 to 1 and assist in the interpolation of the mechanical properties from boreholes.

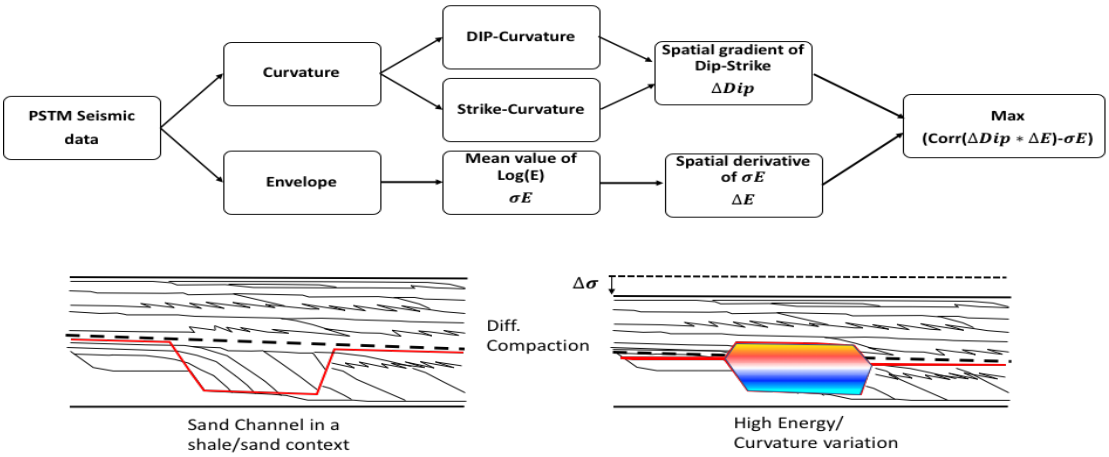

Figure 2-17. Scheme to compute pattern recognition attribute. Attribute computed and used for flat structure classification and correlation of the selected mechanical stratigraphy.

Borehole log information was used, and mineral descriptions from cores outside the area of study to create a velocity model and time-to-depth conversion guided by the tectonostratigraphic framework. Twelve surfaces that represent the significant unconformities were generated, and I highlight four significant faults with the basement are highlighted.

In eight of the wells in the area, I computed water saturation, porosity, the volume of clay, and bulk volume of water using simple petrophysical models was computed. The results of this computation aided the rock-physics models and the geomechanical model in the area, the petrophysics model.

Rock-physics is the link between rock properties and its effect on seismic amplitudes, using petrophysics and well log data. A rock-physics model was assigned to each lithostratigraphic unit and defined the rock-physics constraints in the area. The shear wave equation for the eight wells modeling the S-wave response as a function of the volume of clay, water saturation, depth and lithology (Figure 2-18).

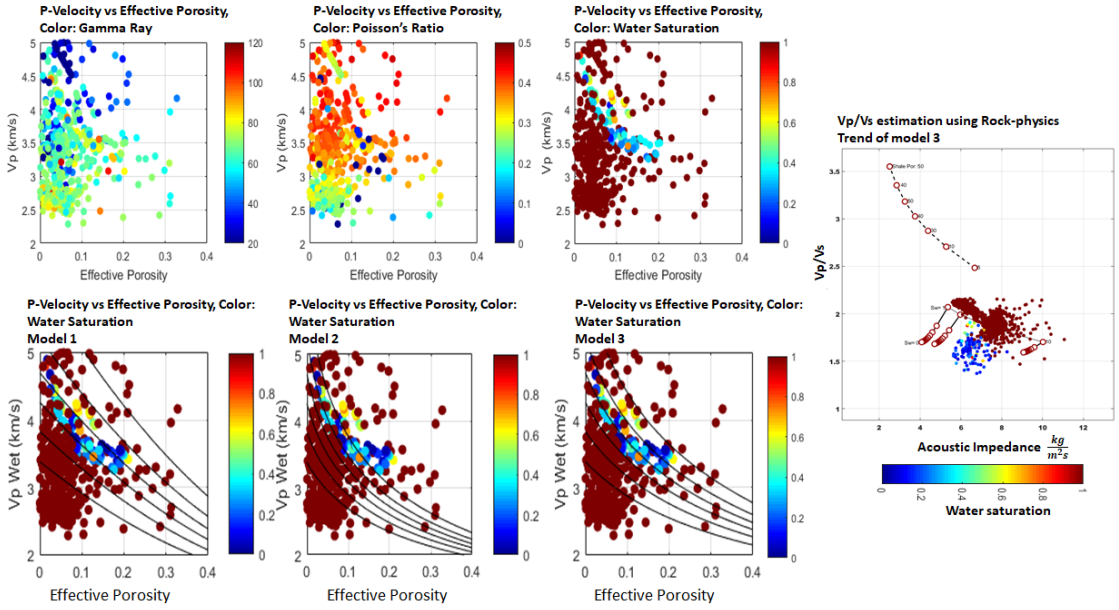

Figure 2-18. Rock-physics model of the Mississippian Limestone calibrated from lithological information and water saturation.

Petrophysical analysis showed that better quality porosity and possibly permeability correlated with chert and quartz content, whereas clay, and limestone tended to be impacting the reservoir quality. The rock-physics model calculated on the Paleozoic sediments showed a large contrast with the basement rock-physics response. Effective porosity versus P-velocity in color, Gamma-ray, where the reservoir is not easily differentiated. Effective porosity versus P-velocity in color, Poisson's ratio. Effective porosity versus P-velocity in color, water saturation. On a selected model, I used the elastic parameters (bulk and shear modulus) selected to calibrate S-Wave velocity.

The results show that as clay content increases, Poisson's ratio varies rapidly as a function of facies distribution. Shale distribution is dominated by facies distribution. Shale lithologies are highly anisotropic and complex linked to microstructure. Different research conducted on shales (

Slatt & Abousleiman, 2011; Zhang et al., 2016; Galvis & Slatt, 2018) showed the Brittleness Index as a function of mineralogy and the role of sequence stratigraphy in computing brittleness, this was used on Woodford shale. Facies distribution controls Poisson's ratio behavior. The geomechanical properties, correlated with rock-physics models from borehole information, helped extrapolate the elastic constants using the high drilled holes density. The boreholes with wireline information show a rapid decay of the shear modulus and Young's modulus as a function of clay volume. Shear modulus has a larger variability with water saturation and porosity. Bulk modulus also reduces as water saturation increases. The limits of the rock-physics modeling I used are restricted to quantity mechanical properties from water saturation, porosity and clay content. I needed minerology logs to estimate a more robust rock-physics model.

Brittleness is a measurement of stored energy before failure, and is a function of rock strength, lithology, fabric, effective stress, temperature, etc. In-situ stresses and lithology are the dominant factors affecting the brittleness distribution of the rock. Wang et al (2009) defined the Brittleness Index originally in 2007 as a function of hard minerals (quartz and calcite) and the soft components (clay minerals and TOC) the BI computation as a mineralogic function is:

$$BI_{Wang(2007)} = \frac{Qz+Ca}{Qz+Ca+Cly+TOC}, \qquad \textbf{Equation 5}$$

Where Qz= Quartz; Dol= Dolomite; Ca= Calcite; Cly= Clay, and later modified the equation was modified

$$BI_{Wang(2009)} = \frac{Qz+Dol+Ca}{Qz+Ca+Cly+TOC} \qquad \textbf{Equation 6}$$

After (Wang, 2009), a mechanical model was constructed using different mechanical functions per lithology and per facies distribution, i.e., carbonates in restricted lagoon versus deeper water carbonates, or buildup carbonate on top of paleo high. The mechanical model consisted of a series of concatenated computations that were calibrated and linked with borehole drilling operation and other mechanical properties. Extended leak-off-test and FIT test were used to estimate the minimum horizontal stress or the fracture gradient. Mud weight profiles guided the pore pressure estimation (Dutta, 1983; Dutta, 2003), which is an extrapolation of the Eaton equation (Eaton, 1975) in the sense that includes different pore pressure mechanism and porosity trends.

Given the borehole density control, the pore pressure profile was extrapolated from the wells using a petrophysical facies model. Different production regimens and the great difference in time of the information available is sets a large offset difficult to update, since the pore-pressure state is dynamically changing with fluid interchange in the subsurface and other stresses present, especially where disposal wells modify even more the fluid distribution in the porous system.

The proposed geomechanical model of the area is a calibrated model of the area. It exploits the high-density drilled wells to assess formation integrity and mechanical properties as a function of the lithology and fluids in the area, hence depositional environment and stress field state. Geomechanics is helpful for perforation design, bit design and bit selection, reservoir compaction and fault activation. Geomechanics links various natural phenomena with human-made activities, for example, it correlates drilling and completion results and other engineering parameters to the in-situ stress fields, temperature gradient (measured up to the total depth of the well), and elastic properties of the rock. To accommodate the engineering parameters of study area wells, the

mechanical earth model represents the average values of the borehole information, including rate of penetration of the bit (ROP), mud-density and Leak-off test points of calibration. The mechanical earth model of the project, this model is the cornerstone of the geomechanics study on the area and represent the rock mechanics prediction of nine borehole log information, including a 114 mud-weight profile average and 44 leak-off test pressure points (Figure 2-19).

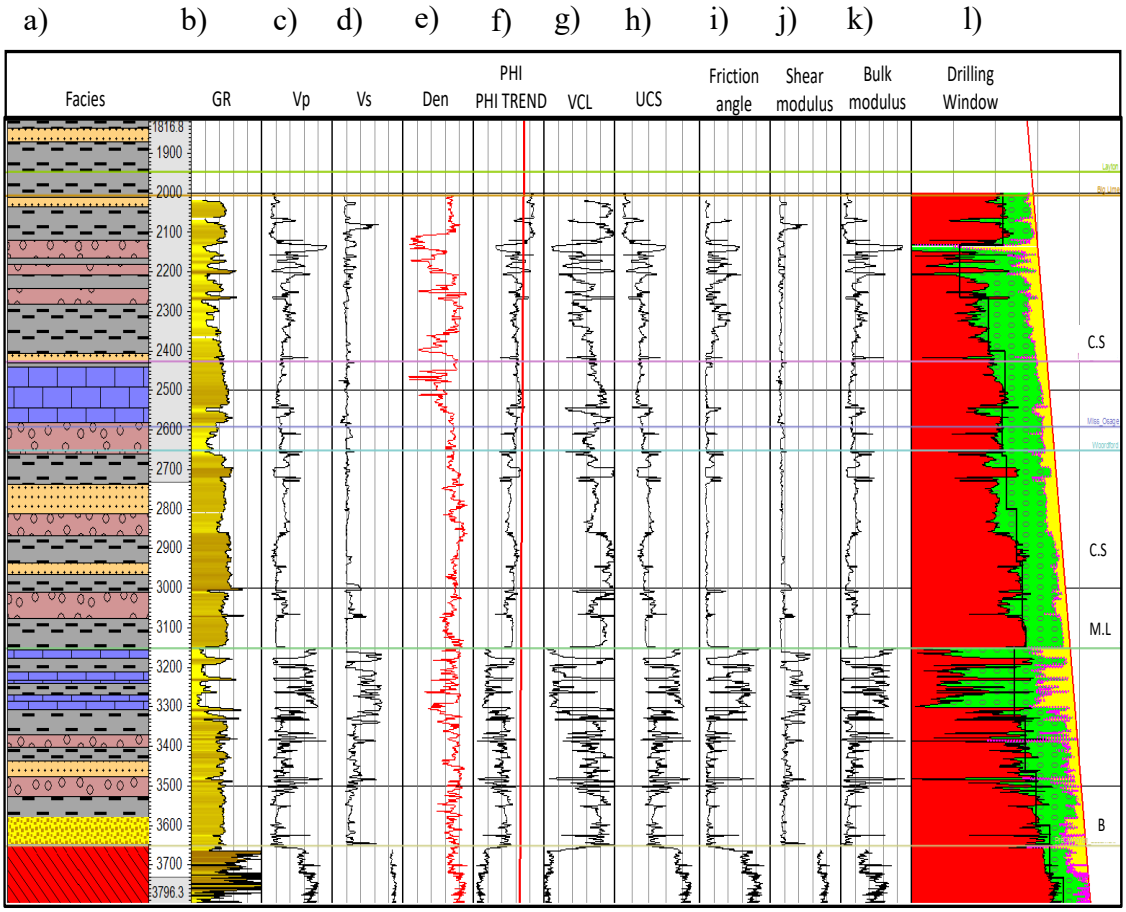

Figure 2-19.

Geomechanical model representative of the borehole information. A) Discrete mechanical facies used on the model. B) GR profile, C) P-Velocity profile D) S-velocity from the rock-physics model. E) Density profile F) Total Porosity and Porosity trend G) Clay volume H) Unconfined Compressive strength from the mechanical model I) Friction angle curve from the poro-elastic model J) Shear modulus K) Bulk modulus L) Drilling window.

In the Fig. 2-19a discrete mechanical facies classification derived from the GR curve in Fig. 2-19b and color filled to emphasize the lithological changes within the section. The compressional and shear wave velocities in Fig. 2-19c and Fig. 2-19d helped guide the facies classification. For example, compacted shales are different than wet shales. S-wave was computed from derived from the rock-physics model. The density profile on the Paleozoic strata standard deviation is which represents the small variabilities of the compaction in the strata. Panels f, g, h, and i in Fig. 2-19 are the output curves from the petrophysical model. Panel (i) is the water saturation curve; it is important to notice the high water cut these reservoir shows. The lowest water saturation is around 30% with an average of 50%. Panels j, k, l and m show the mechanical curves that were used to compute the geomechanical model; j) unconfined compressive strength (UCS), k) friction angle panel and shear modulus (l) and bulk modulus (m). The pore pressure curve is in panel n) and is color filled on red. The pore-pressure curve was derived using total porosity trend and P-wave velocity (Bowers, 1995). The porosity pressure profile was calibrated with the mud-weight profiles read from drilling reports or wireline logs. Shallow mud carbonates showed partial mud losses due to the drilling pressure surpassed the initiation of fracture pressure and were used to calibrate the stress profiles as in (Zoback, 2007). The drilling window represented by the green zone on Fig. 2-19 l is bound by the pore-pressure profile and the minimum horizontal stress profiles. The lithologies and in-situ stress represent the mechanical responses of the subsurface.

To build the 1D geomechanical model of the area, wireline information and drilling calibration points. i.e., leak-off test, mud-weight profiles were used. The irregular normalized accumulative oil production in this portion of Osage County helped to calibrate the porosity-

pressure trends. The framework model is the extrapolation of the structural and stratigraphic interpretation done on the seismic information, time to depth relationship of the wells allowed us to calibrate drilling events and look and its response in seismic data. I used petrophysics results to apply different mechanical properties to each lithology to compute the dynamic elastic moduli; Young's modulus, Poisson's ratio, shear modulus, and bulk modulus. Five distinctive mechanical facies with clear differences in petrophysical and mechanical properties were analyzed. The lithofacies I selected in the model are; coarse grain sandstone, fine grain sandstone, shale, carbonate, and granite.

The mechanical stratigraphy is heavily dependent on the facies properties derived from the rock-physics model. The acoustic impedance seismic inversion and the trace attributes assist the classification of these five different lithofacies into four mechanical facies. The classification combined with the geocellular model helped to distribute the mechanical properties as a function of depth and lithofacies. For example, in the geocellular model, a sand facies at a given depth will follow the RMS value extracted on the top of the basement. Thus, the sand facies have a lateral distribution and a position in depth, or any other of the 5 lithological facies. This classification helped me to expand the borehole results via the geocellular model, as a function of lithology, attributes and, interpretation. Once the lithological properties are assigned at each cell, I classified the brittleness of the rock per sequence with the geomechanical model.

To compute the dynamic elastic moduli, wireline log response was used. Then from the dynamic modulus, I computed the static modulus and Biot's constant. The basic inputs for

computing the dynamic moduli were P-wave velocity, S-wave velocity, density, effective porosity, total porosity, discrete facies log, and volume of clay.

Due to the distinct mechanical behavior of grain supported lithologies versus matrix/mud, the properties of clay-supported and grain supported need to be considered as zone parameters for each facies (Plumb, 2002; Zoback, 2007). The dynamic elastic moduli were calculated by:

Shear Modulus

$$\boldsymbol{G_{dyn} = 13474.45 \frac{\rho_b}{(\Delta t_{shear})^2}},$$ **Equation 7**

Bulk Modulus

$$\boldsymbol{K_{dyn} = 13474..45 \left[\frac{1}{(\Delta_{compressional})^2}\right] - \frac{4}{3} G_{dyn}},$$ **Equation 8**

Young's Modulus

$$\boldsymbol{E_{dyn} = \frac{9G_{dyn} \cdot K_{dyn}}{G_{dyn}+3K_{dyn}}},$$ **Equation 9**

Poisson ratio

$$\boldsymbol{v_{dyn} = \frac{9G_{dyn} - 2G_{dyn}}{6K_{dyn}+2G_{dyn}}},$$ **Equation 10**

The dynamic to static correction in sandstones and grain supported lithologies is considered by Plumb et al. (1994). I also used the critical porosity to classify the porosity of response. The critical porosity in siliciclastic sediments is the porosity above which the rock can only as grain flocculating and surface contact tangent (Dvorking & Nur, 2000; Mavko et al., 2009). In sandstones the critical porosity is 36% -40%, that is the porosity of a random close pack of well-

sorted round quartz grains. The critical porosity for carbonate lithologies is not defined due to matrix definition (Plumb, 1994).

Static Young's modulus:

$$E_{sta} = (-2.21\emptyset_c + 0.965)E_{dyn}, \qquad \textbf{Equation 11}$$

Whereas for shale like lithologies; lithologies which clay content surpass 30%, I chose equation 9 to compute the static Young's modulus from the wellbore response (dynamic) due to Woodford shale rock sample experiments constant derived a better calibration with a coefficient of 0.64. Equation 12 is the one that best correlated the dynamic behavior with static elastic experiments in the Woodford shale and is stated as:

Static Young's modulus:

$$\boldsymbol{E_{sta} = \left(0.032E_{dyn}\right)^{1.64}}, \qquad \textbf{Equation 12}$$

I estimated the Biot's coefficient from effective porosity and Bulk modulus calculated previously. The α constant assumes the skeleton of a rock sample with null interaction other than grain contact (no chemical interchange or diagenesis) (Biot, 1941). The bulk modulus can be correlated without considering the chemical interaction of the fluids contained in the effective porosity and the solid Bulk of the rock module as;

$$\boldsymbol{K_{skeleton} = K_{solid}(1 - \emptyset_{eff})^{\frac{3}{1-\emptyset_{eff}}}}, \qquad \textbf{Equation 13}$$

Then Biot's elastic constant α can be derived as:

$$\boldsymbol{\alpha = 1 - \frac{K_{skeleton}}{K_{solid}}},$$ **Equation 14**

Plumb (1994), calculated the uniaxial compressive strength (UCS) as a function of porosity and shale volume. I used this equation and modified per facies based on a total porosity derived from sonic measurements; this model is close for carbonates for boreholes with compressional velocity information. The UCS equation for Grain-supported rocks is:

$$\boldsymbol{UCS = 243(1 - 2.858\emptyset_{Total})^2},$$ **Equation 15**

On the other hand, for clay-supported rocks, where the stress is distributed among the grain contacts, and the behavior is less brittle, the UCS can be approximated in Mpsi as:

$$\boldsymbol{UCS = 70(1 - 2.222\emptyset_{Total})^2},$$ **Equation 16**

For granite rocks in my study area, UCS was computed using shear modulus and porosity, since UCS is a property dependent to the lithology not to porosity. The in-situ stress affects the UCS, specially the maximum stress in the area and the history of deformation. It is a close approximation in Mpsi in Equation (17).

$$UCS = (.13G_{dyn})^{2.3},$$ **Equation 17**

The clay-supported rocks are more resistant to uniaxial compressive stresses than grain-supported. The grain contacts are highly deformed and prone to thermal and chemical interchanges, which makes a stronger bond that translates into higher Brittleness Index (Yilmaz, et al., 2009). This property is a function of facies and shear behavior. From the UCS calculation,

friction angle and tensile strength are calculated using (Plumb et al., 2000), which consider clay content and porosity correction into tensile strength computation.

I computed the vertical stress, from extrapolating density logs and performing the summation over depth, this is possible due to the depth geocellular model made from the time-to depth conversion. For wells without density log, I used extrapolated density model using Gardner empirical equation from velocity to density (Gardner & Gregory, 1974). I also included the velocity model as guide to extract seismic velocities from the Earth's model from thirteen acoustic borehole information located spread-out the study area. Boreholes with density logs and resistivity logs served as calibration points.

$$\sigma_{V(i)} = \sigma_{V(i-1)} + g\rho\sigma_b(i) \cdot (TVD_{(i)} - TVD_{(i-1)}) \qquad \textbf{Equation 18}$$

Since integrating density should start from the surface (depth =0), 2100 kg/m^3 was used as a constant density from ground level to 60 meters. Sediment gets compacted with depth, as a natural consequence of this compaction, there is a loss of porosity and increase of rock density. Many other factors can change the compaction trend, to mention a few, mineralogy, grain size, burial history of the basins, diagenetic history (mechanical compaction) (Bjørlykke et al., 2008). The total porosity is a result of this changes. I computed a total porosity trend to calibrate the compaction equation as a function of overburden. In its purest form, pore pressure is the pressure of the fluid contained in the pore spaces of rock; it is a function of depth and many other factors. In general, if the registered pore pressure is below or above the normal trend, pore pressure is abnormal pressure. I analyzed the pore pressure regime using the equivalent depth method; this analysis uses information from the different well logs that are available and mud-weight profiles,

mud density profiles are the evidence of the pore pressure of the formation as a gradient with depth, it is used to contain the influxes while drilling or completing the well. From the analysis, I concluded that the direct method, developed by (Bowers, 1995) was the most suitable for this low pore pressure regime, since this method accounts for overpressure generated by both under compaction, and pore-fluid expansion and sub-pressure. This method does not account for pore pressure in carbonates, especially for the Arbuckle, Mississippi Lime, and the Precambrian granite.

On the other hand, Bower's method (Bowers, 2001) overcomes the limitation of two different empirical relationships between the measured compressive velocity and effective stress. I discarded the Eaton method since it is most valid for shale lithologies (Dutta, 2009). The pore-pressure estimation is a static estimation of the pore-pressure regime at the moment of drilling.

In summary, I used Bowers (1995) for estimating the pore-pressure in siliciclastic formation. For carbonates I used spline interpolation from values above and below Mississippi Lime. I calibrated the model with mud-weight densities from the wellbores in the area. Drilling parameters are crucial to calibrate the pore-pressure. It would have been ideal to have pressure data from reservoir pressure, but these data are not available in IHS database. The pore pressure curve was used as an input into Terzaghi's compaction theory (Terzaghi, 1960), which defines the effective stress, which defines the formation compaction as the main factors, rather than overburden stress. The effective stress is:

$$\sigma_V' = \sigma_V - P_p, \qquad \textbf{Equation 19}$$

The poro-elastic theory proposed from Biot's model latter defined as Terzaghi compaction included into the Terzaghi's equation yields into a poro-elastic compaction theory as:

$$\boldsymbol{\sigma'_V = \sigma_V - \alpha P_p},$$ **Equation 20**

It is necessary to highlight the large temporal range. The most recently drilled borehole is from 2017 and the oldest is from 1929. There is a long production/injection history which makes it difficult to create a normalized pressure datum. The pore-pressure model only captured a static behavior in the pressure model, which is unrealistic due to the dynamic hydrocarbon withdrawal and water injection. However, the initial pressure from the producing reservoirs showed a good correlation with the porosity system described.

Vertical stress is only one of the principal stresses applied to the rock formation; they together describe the stress field the rocks are exposed. The minimum and horizontal stress complete the in-situ formation stress. The stress field is as a complicated geological process where an elementary volume is affected by overburden deposits, repeated cycles of elevation and depression, diagenetic changes where matrix could be chemically substituted, tectonic forces and other thermal effects.

Well log information and leak-off test pressure was used to calibrate and define minimum horizontal stress using Mohr-Coulomb failure criterion as:

$$\boldsymbol{\frac{\sigma_H - \alpha P_p}{\sigma_h - \alpha P_p} = tan^2(\frac{\pi}{4} + \frac{\emptyset}{2})},$$ **Equation 21**

σ_H Maximum Horizontal Stress; α Biot's constant σ_h Minimum Horizontal stress; P_pPore pressure $\emptyset$ Maximum Angle (Gholami et al., 2014; Vernik & Zoback, 1992)

To represent the irregular hydrocarbon production, initial pressure production into the geomechanical model was included where available. The initial production pressure calibrated the pore-pressure model.

Mohr-Coulomb criteria encompasses the three classic fault regimes: normal, thrust and strike-slip (Anderson,1905; Simpson 1997). In the area the stress regime is a strike-slip regime, where $\sigma_H > \sigma_v > \sigma_h$. For calculating the minimum and maximum horizontal stress, I used (Plumb, 2002) to account the fact that horizontal stresses are a linear function of pore pressure and vertical stress.

$$\boldsymbol{\sigma_h = AP_p + B\sigma_V + C,} \qquad \textbf{Equation 22}$$

$$\boldsymbol{\sigma_H = A'P_p + B'\sigma_V + C',} \qquad \textbf{Equation 23}$$

Where A, B, C A', B', C' are zone/facies-based constants. The geomechanical model of borehole UWI # 3511303730000 shows the average geomechanical model of the area, minimum horizontal stress, and pore pressure values. The maximum horizontal stress was calculated using constant stress ratio:

$$\boldsymbol{\sigma_H = \sigma_h K',} \qquad \textbf{Equation 24}$$

Using drilling results, and considering the geology of the area, lower and higher stress regimens were defined. I used the fluid loss to calibrate the minimum horizontal stress magnitude. I interpreted the amount of drilling mud to discern loss severity (Edwards, 2002), to understand why a loss has occurred. I defined a severe loss of circulation and a total loss of circulation as a consequence of long section of unconsolidated sediments or fractures (Smiley, 2014); also caverns or high porosity reacting carbonates and large fractures in the events highlighted in Figure 2-20.

In order to perform the acoustic impedance inversion with conditioned amplitude spectrum, I calibrated with wavelets extracted for each well. The low-frequency model was conducted using variance attributes as extensional constraints - acoustic impedance results from seismic inversion versus well acoustic impedance response. East and west borehole data are left outside the amplitude response inversion to use them as blind test wells. The amplitude impedance showed a correlation with the geomechanical model of the area; the logs were modeled using the rock-physics modeling parameters, sequence stratigraphy is used as spatial constraints to overcome the existence of critical borehole log data to predict the elastic response of the area. The acoustic impedance section shown in Figure 2-20 has good lithological constrains from 200 ms to 1000 ms. The borehole recorded logs were within this two-way time range. Seismic impedance processing removes the wavelet effect from the seismic amplitude in the process of deterministically make the convolution of the best P-impedance model with the characteristic wavelet to generate a synthetic seismic that minimize the misfit between the observed data and the synthetic seismic information. The result of the seismic section increases the resolution of the resulted attribute.

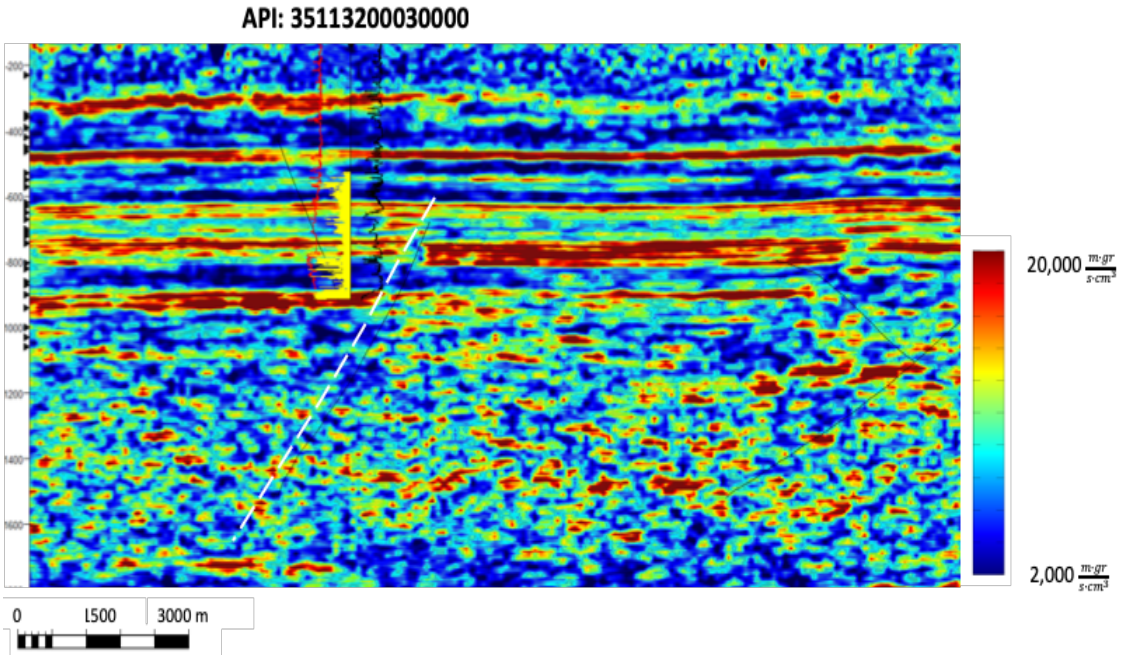

Figure 2-20. P-Impedance distribution in a W-E section from the post-stack seismic inversion.

The fault discontinuity evident on the P-impedance attribute shown in Figure 2-20 is 150 meters east of the borehole. This wellbore showed evidence while drilling of a major loss of circulation. Given the severity on the mud loss, and the proximity of the fault, it is possible that the fault acted as a fluid pathway connecting basement with shallower stratigraphic units. The basement reflections are highly discontinuous due to quality of the reflection from seismic.

After determining the mechanical properties, they were linked to the Brittleness Index per horizons zones as:

$$BI = \frac{\left[\frac{100*(E-E_{min})}{(E_{max}-E_{\min})}+\frac{100(v-v_{max})}{(V_{min}-V_{\max})}\right]}{2} \qquad \textbf{Equation 25}$$

Where E is Young's modulus, and v is Poisson's ratio calculated from the mechanical properties, which were derived from petrophysics/rock-physics and drilling parameters. From the Brittleness Index (BI) equation it can be derived that is unitless since it is a coefficient of pressure units divided by pressure units. Brittle index (BI) from Equation 25 exhibits a measurement of stored energy before failure since takes into account Young's moduli differences as a factor and the maximum velocities. It also relates the elastic moduli and subsurface properties such as depth and pressure, but also lithologies. In other words, Brittleness Index sets the strain-stress slope in a plane-shape as the range Young's modulus (maximum – minimum) on the uniaxial case and also from the Poisson's ratio range.

The BI is a measurement that also unintendedly takes the deformation history also into account, since materials with a long history of deformation need higher stress rates to deform. The BI also allows measurement to discern the brittleness of material, where the most distinctive characteristic is the lateral strain yielding of the material (i.e., a ductile material yielding due to a uniaxial force yielding) (Yilmaz et al., 2009). The internal cracks would re-arrange, collapsing the inter-mineral space, then the minerals would increase its surface area, and the strain would continue until the elastic-plastic limit. On the other hand, when a brittle material is under uniaxial stress, the stress-strain slope would be more pronounced, reaching higher stress with lower strains, however where the elastic-plastic limit is close, the framework of the rock starts to collapse creating internal fractures from the porous grain architecture (Abdulraheem et al,. 1992).

Concerning the Mississippi Lime related carbonate deposits; however, fractured chert diagenesis is associated with semi-vertical fractures that input silica and impacted the porosity

(Vandervoort, 2011). These heterogeneities, impact reservoir brittleness. The interplay between the paleo-topographic highs and carbonate deposition. Higher structural features in the basement promoted fractures in the Mississippi Lime in its chert lithology (Zhang et al., 2016). Furthermore, the third and fourth sequences marked a rapid regression that accelerated weathering and erosion on the elevated carbonate buildups, which catalyzed in sinkholes and karst formation. On the flanks of elevated buildups, the erosion accelerated the brecciated fluxes into open water.

In open water settings or temporally open, the Mississippian Limestone deposition continued until early Pennsylvanian (Kirkland, 1992). Mississippian Limestone and more in specific the tripolitic chert exhibit a transition from ductile to brittle in four different lithological behaviors (Figure 2-21). The classification shows four different mechanical classifications, the most brittle lithology carbonates (limestone-dolomites) and igneous rocks correlate with borehole lithology descriptions. The most ductile lithology corresponds to siliciclastic lithologies (shales-sandstones). The intermittent values represent lithologies with a higher shear modulus and higher Young's modulus. The mechanical curves were derived by combining the information from the rock-physics models and the geomechanical model. The basement low-velocity anomaly had an evidence inn the borehole that was less than 200 meters west to the vertical low brittleness anomaly, this low velocity could be connecting the basement top and upper strata with the low brittleness anomaly inside the basement. The basement top is clear and shows two distinctive less brittle zones, the horizontal anomaly to the east of the section and the almost vertical lower brittleness anomaly to the west (Figure 2-21). The Reagan sandstone lies unconformity on top of the basement. On top of the Reagan, sandstone is the Arbuckle carbonate group represented by the blue horizon. The top of the Mississippian Limestone group is around 500 ms.

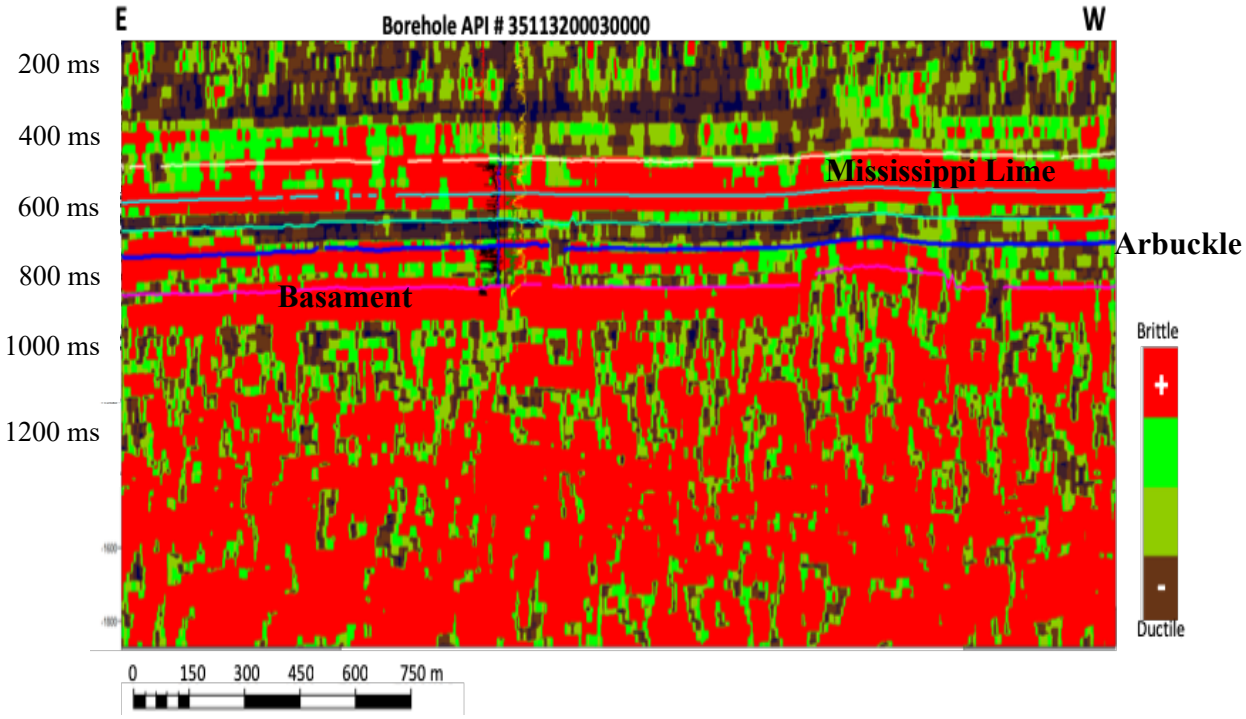

Figure 2-21. Mechanical facies classification (BI) using P-Impedance and the geocellular model section showing the discrete facies distribution with depth.

From the boreholes analyzed, the facies in the area were divided by the different petrophysical and geomechanical properties. Limestone facies showed lower porosity in comparison with the diagenetically altered carbonates, this mechanical behavior is corelated with the stratigraphy of the Mississippi Lime.

Brittleness Index correlates with the geological model of the Mississippian/Pennsylvanian unconformity. The mechanical properties (bulk modulus, shear modulus, Young's modulus and Poisson's ratio) helped classify, with more detail, four different facies (Figure 2-22). These mechanical properties are a function of lithology, minerology, and in-situ stresses. i.e. overburden, pore-pressure, minimum horizontal stress and maximum horizontal stress. Vertical discontinuities are observed in the basement, either due to faults, a product of tectonic effects (with lines) or

possible igneous intrusions because of the vertical tortuosity. Horizontal discontinuities are observed 200 meters below the top of the basement. Redlines on the Precambrian basement and the Mississippi Lime represent erosional surfaces (Fig. 2-22). These discontinuities create different alteration on overlaying stratigraphic units.

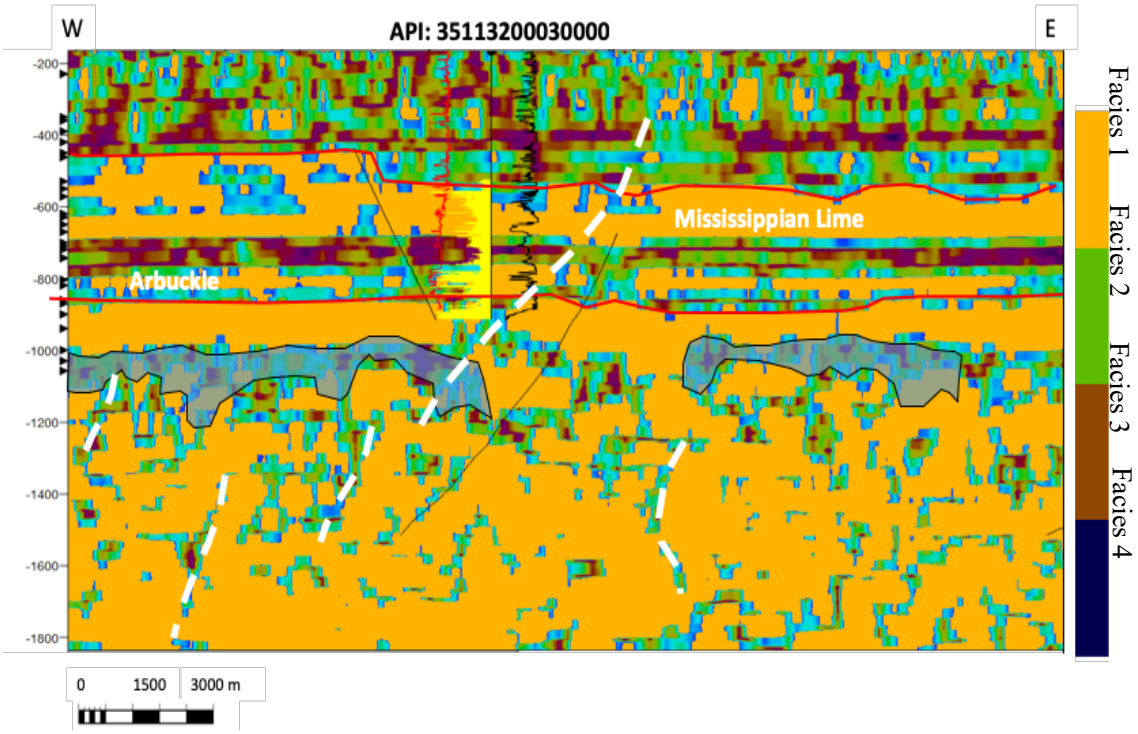

Figure 2-22. Basement and other irregularities on the brittle facies classification with fault likelihood and compaction attribute included.

As means to offer a workflow, the following table explains in detail the input and output and premises used to build up the brittleness index model.

Step	Raw Data	Model(s)	Data To	Preliminary Results
Data loading and seismic Interpretation	3D seismic volume Borehole information	Sequence stratigraphy Fault network	Geocellular 3D grid Attribute comp.	Stratigraphic/structural framework Reservoir stratigraphy
Object base simulation	Formation tops, faults, depth-slice surfaces	3D Geocellular model (#1)	Velocity modeling and T-D conversion	3D grid with cells of 35m by 35m, 35 m thickness
Single velocity function extrapolation	Wireline logs (sonic-density) Formation tops	3D Geocellular model (#2) Velocity model	Fault mechanical stratigraphy	Depth model of the principal stratigraphic units and faults
Seismic inversion (P-Imp) & Attribute analysis	3D seismic volume Geocellular model (#1) Wireline logs	Deterministic seismic inversion in Hampson and Russell	3D Geocellular model (#2) Rock-physics equations	P-Impedance calculation calibrated with borehole information
Compaction and deformation analysis from fault age	Faults and formation tops	Fault mechanical stratigraphy	3D Geocellular model (#3)	Stratigraphic/structural framework Reservoir stratigraphy
Petrophysics modeling	Borehole reports Wireline logs	Dual porosity(Sw, V_{clay} & ϕ)	Rock-physics model and Geomechanics	Water saturation, porosity, and clay content Per facies
Rock-physics modeling	Petrophysics logs & borehole inf. Wireline logs	Constant cement model	Integration of P-impedance & Brittleness	Elastic moduli relations as a function of clay content, water saturation and porosity
Geomechanical modeling and data integration	Drilling events (mud weights: FIT, LOT-E.LOT) Completion data &Wireline logs	Facies discrimination Mechanical earth model Elastic equations	3D Geocellular model (#3) Mechanical model	Elastic moduli from relationship to drilling parameters and wireline logs Such as SP, Res, and formation tops
Sequential Gaussian simulation	Rock-physics logs Petrophysics logs & Geomechanical data	3D Geocellular model (#3) Mechanical model	PCA analysis Structural attributes	Areal expanded elastic moduli
Principal component analysis (PC)	Attributes 3D Geocellular model (#2	Normalization/covariance and SVD	Maximum likelihood classification	PCA analysis and brittle facies identification
Mechanical facies classification	PC1, PC2, PC3 Structural attributes	Geocellular model (#3)	Correlate with the P-Imp, BI	4 Brittleness Index (BI) facies classified from the elastic moduli range and PCA
Correlation of P-Impedance with facies mechanical model	P-Impedance Discrete facies model Production data	Integrated P-impedance with for the 4 different brittle facies	Calibration with borehole data and production	Identification of relationship between BI and well As a function of the stratigraphic model and controlled by faults

Table 1.- Workflow summary as input, model, output and comments and the connection between different.

2.6 Interpretation

As mentioned on the methodology, brittleness is a function of mineralogy, fluid, porosity, grain cement, and grain contact (Yilmaz et al., 2009). Hence it is my interpretation that it is insufficient to characterize a complex mechanical property as a binary behavior i.e. brittle/ductile couplet. The Brittleness Index attribute (BI) computed presents a guide in assisting near-field exploration and production by understanding how porosity/permeability changes with facies and how the frackability properties changes as a function of stratigraphy changes and mechanical behavior. The methodology I am presenting is an integrated methodology that is used; it combines P-Impedance, attributes seismic classification and, geomechanical modeling, into a mechanical/stratigraphic Earth model in the form of a geocellular grid that captures a broader brittleness spectrum, not a binary behavior, and this is the principal and foremost finding. This methodology can receive multiple updates from boreholes, seismic re-processing, or seismic velocities. Indeed, to capture an absolute brittleness value is challenging, but the brittleness index is a relative attribute where values ranging from zero to one and where low values represent the least brittle material, and high values represent the most brittle material. Brittleness Index can serve multiple purposes to understand how rock frackability properties change with facies and with fluid and clay content. This would be my first finding, the correlation of higher production with higher brittleness index values in the Mississippi Lime. The importance of the Mississippi Lime is that, historically, the major reservoir in this area is from the Late and Middle Mississippian also known as Mississippi Lime.

The importance of correlating a high Brittleness Index with the accumulative oil production is that it could guide the near-field exploration looking for bypassed reservoirs in this formation. In the study area, the accumulative oil production is close to half a million barrels of oil. The Brittleness Index controls the production and not the structural trap style, and that is because the trap has a stratigraphic style with a minor structural component (Aisenberg, 2013; Vandervoort, 2011). The reservoir rock corresponds to highly porous limestones, where porosity ranges from 12% to 28 %, but connections are obstructed mainly by high variability in the lithology of the section. These variabilities create at least four reservoir facies. The inner reservoir discontinuities and the possibility of discerning the low brittleness lithologies acting as seal from the highly porous chert horizon functioning as reservoir rock is the third major finding of this methodology. The Mississippian Lime is a complex reservoir that faces two principal challenges, the first one, vertical and horizontal isolated discrete reservoir facies with different porosity systems. The second challenge is the oil-bearing fractures which are lithologically controlled, and its extension and geometry are deeply connected with mechanical properties - a BI cube deals with both these challenges Figure 2-23 .

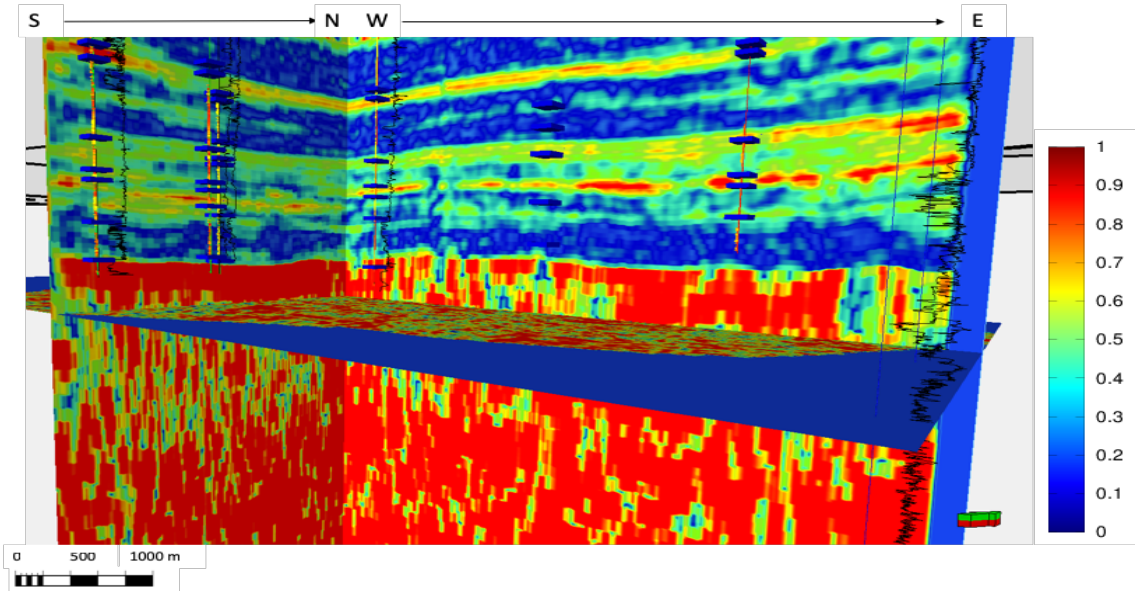

Figure 2-23. The 3D visualization of the inner basement low brittleness anomaly, this low BI anomaly could represent volcanic intrusions or a change on lithology.

The BI is a relative value of the brittleness without regarding its context. The BI attribute allows for better characterization of the mechanical characteristics on the Precambrian rocks and the Cambrian sediments. For example, the Reagan sandstone, which exhibits a channelized behavior, this characteristic is better identified by harnessing the high resolution from the geocellular model and the lower resolution of the mechanical properties distributed into four different facies in Fig 2-22. Although the BI model for the basement could be better represented as almost homogeneous basement, irregularities exists and come from different processes impacting the basement. The model in Fig. 2-22 shows the setting for the heterogeneous basement and the deposition of overlaying sequence. The schematic of subsurface model on northern Oklahoma (Figure 2-24) shows the basement on Osage County relatively higher shallower, which corresponds to the Osagean basement anomaly (Crain, 2017). This is important because it controls at all times the deposition of younger strata. The first important concept to have in mind is that the

Osage Basement high controls the Reagan sandstone deposition as for being a structural highs and sandstones are deposited on flat surfaces (Vail, 1971).

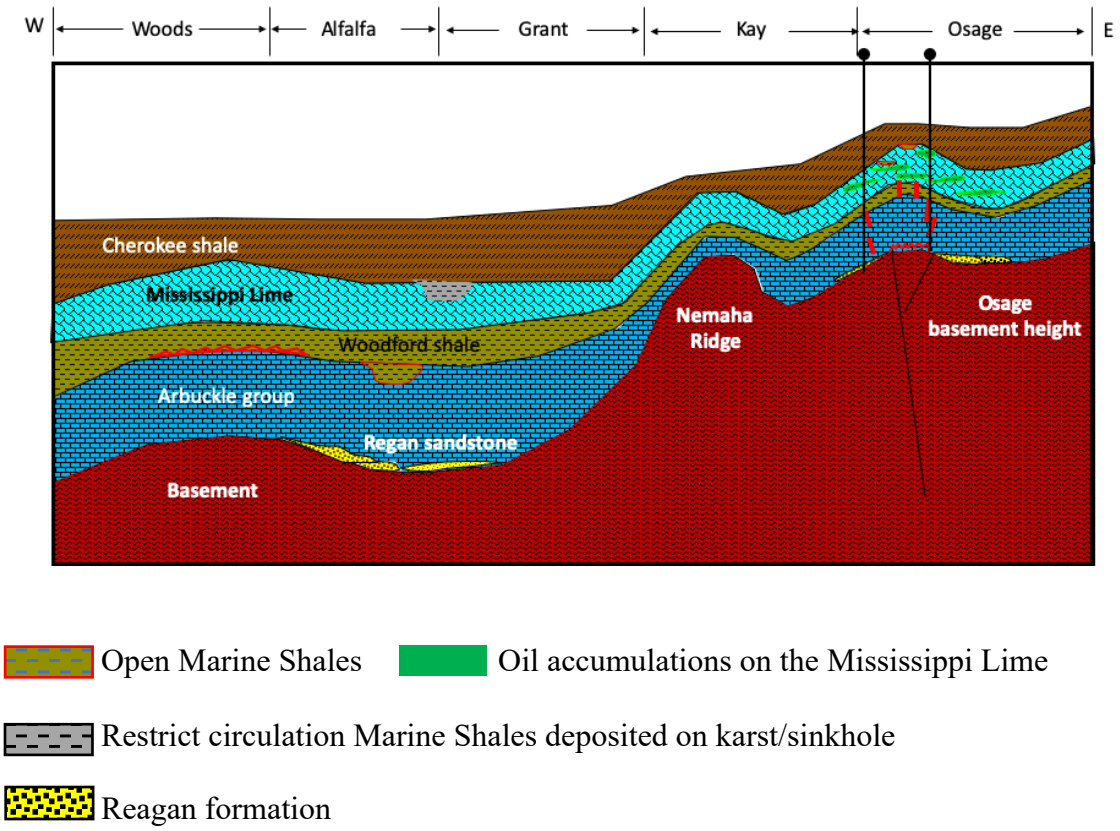

Figure 2-24. Schematic section on the different thickness as a function of structured basement along with other secondary deposition features. (Modified after an interpretation similar in Becerra, 2017)

In theory the basement could be better represented as an homogeneous igneous basement (Denison, 1966; Denison, 1981). However, the BI attributes calibrated with borehole log response suggest a low brittleness anomaly. This low brittleness anomaly has two different representations, the first, is attested by borehole API # 35113200030000 as a loss of circulation when the borehole drilled close to this low brittleness anomaly. The second representation of this discontinuity is a low velocity anomaly where basement velocity experienced a reduction of 40%. The third finding of my thesis is the characterization of the low brittleness anomaly inside the basement (Figure 2-

25) that I interpreted as granitic-micro granitic rock in contact with rhyolites most likely, a second plausible interpretation is an aging contact, that is a volcanic intrusion of different volcanic intrusions. The borehole drilled the basement, but wireline investigation is short, therefore the P-impedance does not show with confidence the values in the basement.

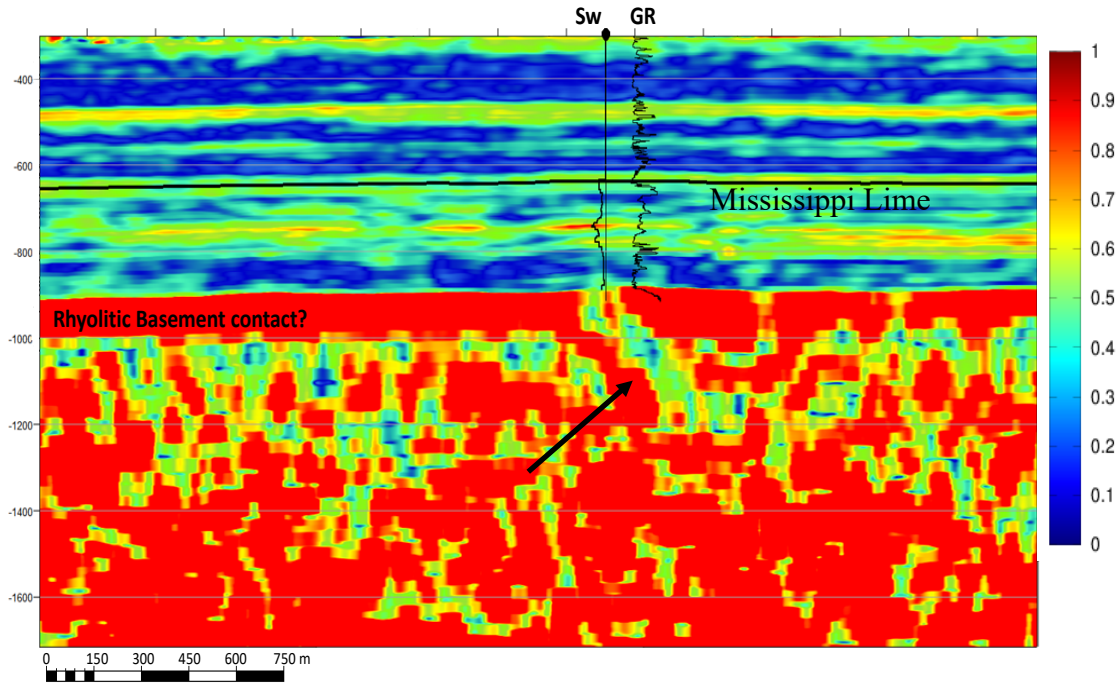

Figure 2-25. BI section shows a borehole that intersect a low brittleness anomaly on the basement. The borehole suffered a major fluid loss of circulation.

Once established the presence of a discontinuity in the basement, the principal reservoir description is a fine carbonate progradational deposit with intricated architecture affected by paleo structural highs, and sea level changes occurred during the Carboniferous. In this study, as I showed I separated lithologically three facies; The limestone differences in texture are; grained limestones (brecciated fluxes), argillaceous mud limestone, and cherts (silica diagenetic affected carbonates). Mechanically I classified four lithofacies accordingly. Also, the petrophysical model

shows a high water cut for the Mississippi Lime, and the high variability of the clay content indicates a rapid change from chert, limestone to dolomites. The rock-physics model from (Figure 2-18) shows an increase in shear modulus and Young's modulus as the volume of clay decreases. Litho-facies and water saturation guided the silica distribution.

To contextualize the different porosity systems latter, it is important to highlight the distribution observed at Figure 2-12 shows the different porosity systems in the Mississippian Limestone. The resolution limits and resolution difference between the multiple datasets. At borehole resolution, this discontinuity can be observed, however it is not evident at seismic resolution. The vertical trapping mechanisms or inter-Osagean unconformities have larger amplitude due to tuning thicknesses, the wedge model in (Figure 2-3) a show that below 30 meters, the trace can no longer discern the boundaries and the amplitude increases. However, these unconformities and seals are below seismic resolution (Fig. 2-2b). These unconformities impact the reservoir connection, creating a vertically stacked reservoir with large horizontal heterogeneities.

The petrophysical model results of the Mississippi Lime (Figure 2-11) shows that the acoustic impedance and Poisson's ratio are most affected by the lithology rather than water saturation and effective porosity. I can prove this by showing the large difference on the acoustic impedance when using a 24% porosity substituted with gas. The Mississippi Lime reservoir is a complex reservoir and exhibits multiple porosity systems and that changes rapidly between boreholes due to the diagenesis of its reservoir (Figure 2-11a).

The porosity systems (Vandervoort, 2011) potentially present in the study area are intercrystalline porosity, vugular, and bed bound fractures. Characterization of any these systems is below seismic resolution, however the combination of different geophysical methods can augment the detectability range to discern the average of different mechanical characteristics. For example, using classification algorithms, I built the initial brittleness facies classification. I used most positive and most negative curvature, sweetness, energy ratio, amplitude root mean square (RMS) and a low-frequency P-impedance cubes to train the facies classification. The brittle lithology classification is divided into four lithology mechanical classes (Figure 2-22). The mechanical classification represents the transition from brittle to less brittle behavior, that for example would correspond to karstification and sinkholes filled with shales surrounded by carbonates. The karstification deposition shown in the classification as an intermediate to low brittleness surrounded by a more brittle material. Karst geometries are subspherical and filled by fine grain sediments, typically by carbonate muds. Sinkholes are collapsed karst caverns on the limestone surface, are round-like geomorphology and have an irregular behavior. Sinkhole morphologies have a lower brittleness response due to the fill-ins on the surface, siliciclastic sediments deposited during sea level rise. The sinkholes create a form of small isolated basins with anoxic conditions due to restricted water accumulated and sediments deposited in a transgressive system track (Figure 2-22). The Mississippi Lime also exhibit important characteristics specially the highly compartmentalized Mississippian chert reservoir, both horizontal and vertically. The boreholes present in the figure contributed with formational picks and wireline logs. The BI attribute also on the Woodford show low BI values close to 0.1, but some prospective facies could be around 0.4 and 0.5. The structural paleo-high on the W-E section of the isometric figure shows

the impact to the Mississippi Lime, but the horizontality of the Cherokee limestone at 350 meters Basement and other irregularities on the BI (Figure 2-26).

Mechanically chert in the Mississippi Lime exhibits a high rigidity skeleton matrix. However, the high porosity - low permeability and low water saturation generate a highly fragile lithology, in contrast with the less brittle limestones that are characterized by low porosity / low permeability. Mississippian dolomite genesis was controlled by two factors, water interaction in the Late Pennsylvanian and tectonic genetic faults. The low brittleness, low porosity, and low permeability creates an effective seal that vertically separates the Mississippi chert. The seal performance can be interpreted from the high variability pressure points I used for in each well with available information. The considerable pore pressure variability indicates small reservoir interaction and fluid connection (Figure 2-26). The blue boxes in Figure 2-26 show the reservoir compartmentalization and how the BI attributes agree with the deposit model of erosions on the flank of the topographic high. The production also is affected by the chert lithologies that are discerned using the BI attribute.

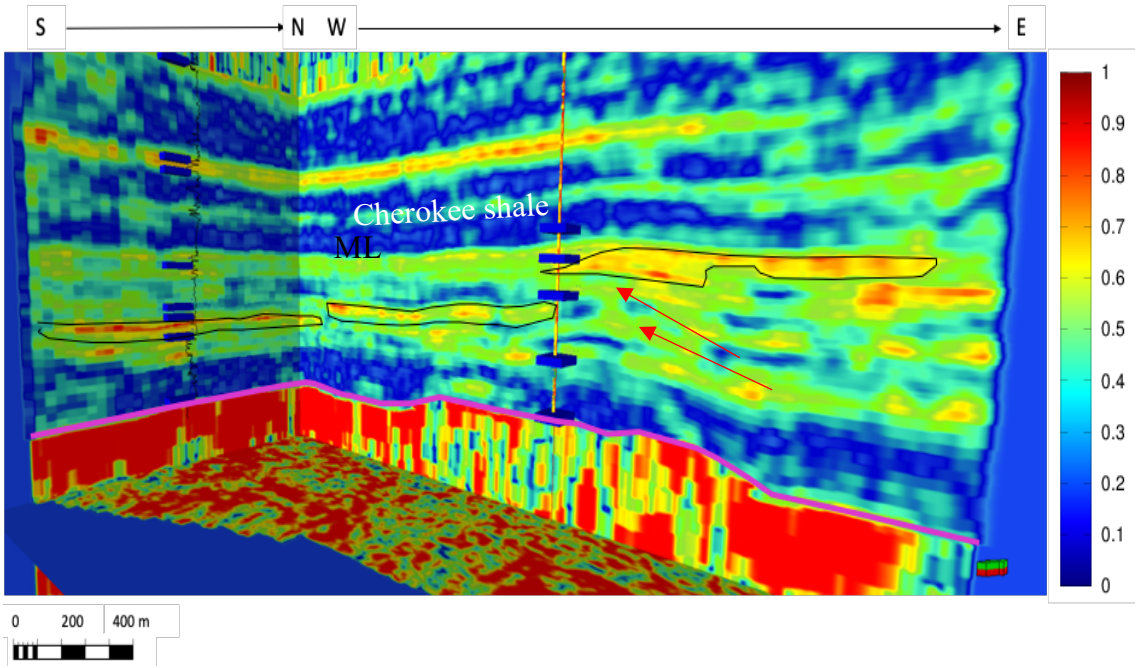

Figure 2-26. 3D visualization of the high values of the high Brittleness Index in the Mississippi Lime (ML). The vertical seals separate reservoir levels. Also the BI shows the inner basement low brittleness anomaly.

The geological and mechanical conditions of the reservoir also make it complicated to stimulate hydrocarbon production. The fractures make it challenging to connect the reservoir horizontally. The BI attribute shows vertical seals that compartmentalize the reservoir (Figure 2-26) on the red arrow.

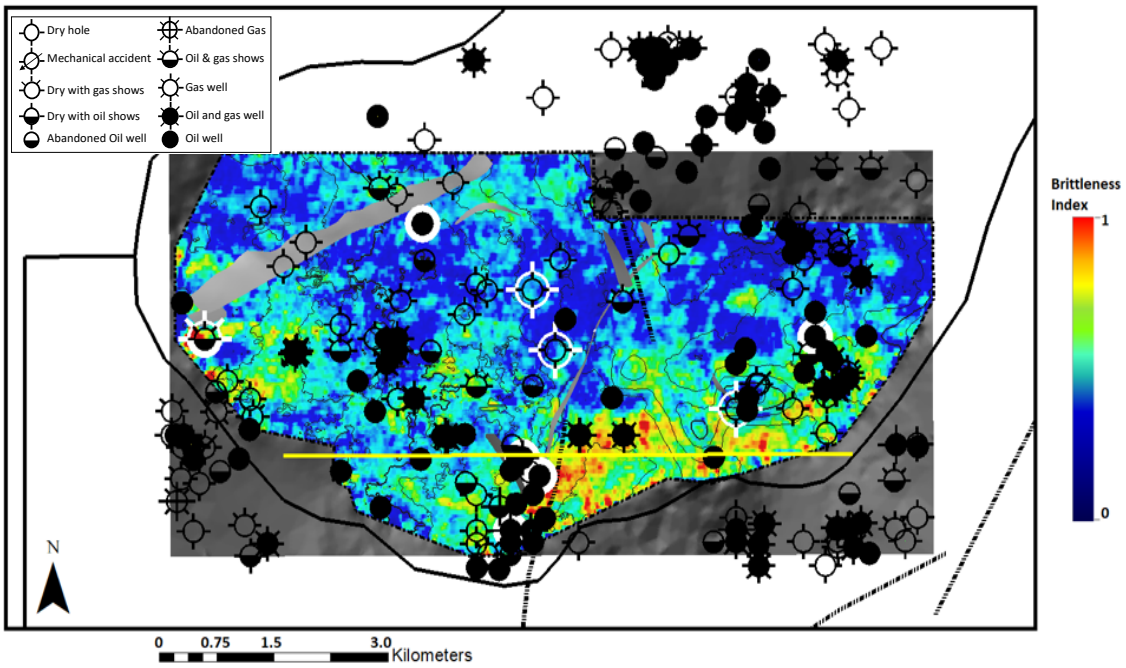

Figure 2-27. Brittleness index distribution on the Mississippian Chert. Polygons show basement topography via contour lines.

Maximum value extraction of the BI attribute on the top of the Mississippi Lime shows a good correlation of high BI values in the southern corner with the accumulative hydrocarbon production map of Mississippi Lime in chert facies (Figure 2-30). The correlation with the productive boreholes and the high BI extraction follows depositional model. It is noteworthy the structural high on the east of the red values of the Brittleness Index. The maximum accumulative production represented by the red circle and close to this, the second largest accumulative production contrast with the cluster of yellow oil productions and green productions, which are the fourth largest productions (Fig. 2-28). The variations on the accumulative production I interpreted comes from vertically seals and small extension of cherts, which are represented by high brittleness values.

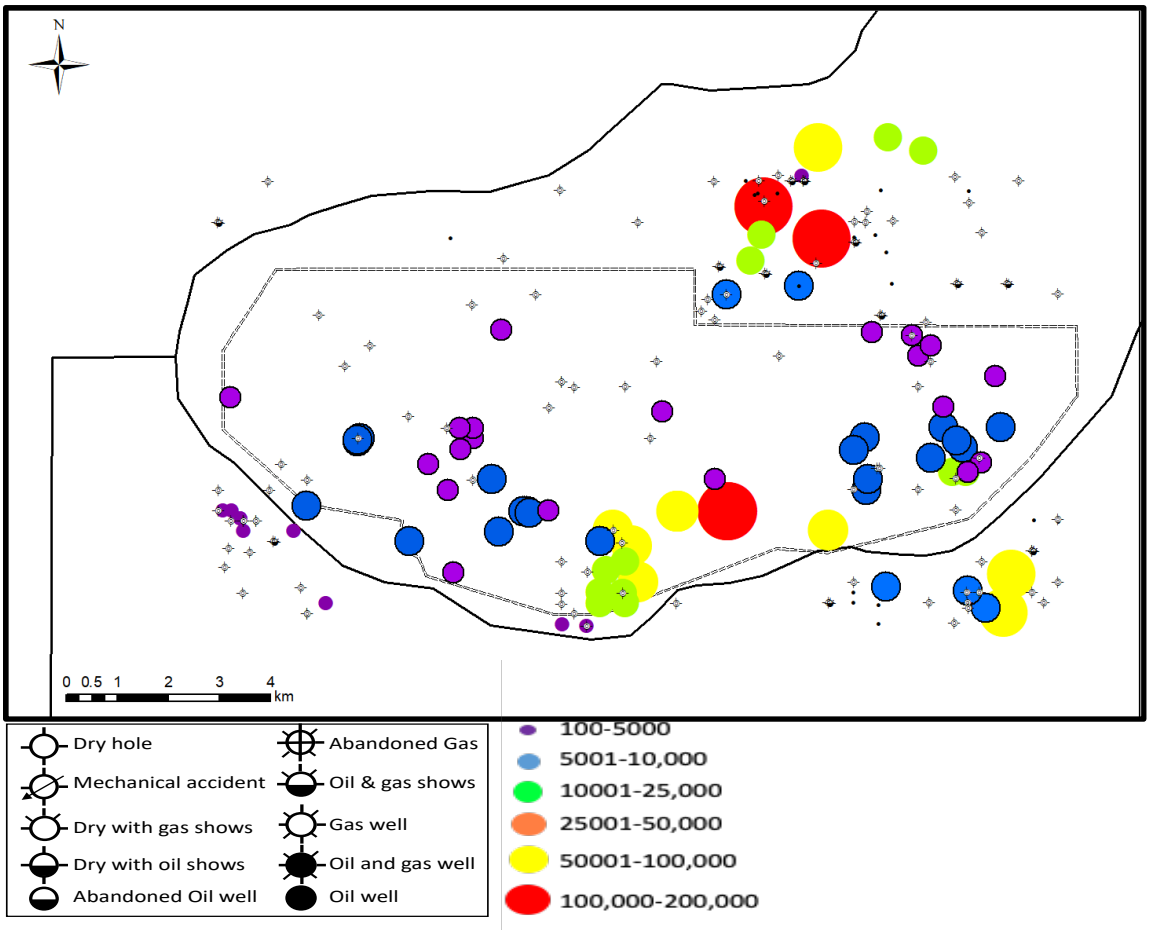

Figure 2-28. Accumulative oil production of Osage County. The highest hydrocarbon production accumulations correspond to higher values of the Brittleness Index.

In this portion of the study area, the Devonian Woodford deposited on the Cherokee platform, in particular in northeastern Oklahoma is thinner than other basins in Oklahoma. For this survey, Woodford thickness varies from 10 to 90 meters. The reduced thickness in the Woodford shale in this portion of the Cherokee platform corresponds a paleo topographic high that controlled the deep marine clay deposits the scheme on (Figure 2-24) (Becerra, 2017), shows the thickening to the West and South versus the thinning on the West and north.

As the Mississippi Lime, the Woodford shale's mechanical properties are closely related to the small changes in the depositional stratigraphy, mineralogy composition, and total organic content. The Devonian shale deposits reported south of the Cherokee platform and west of the Nemaha are thicker, more profound and with higher organic content. In the south, the Devonian shales of the Arkoma basin are in the oil window. Moreover, the hydrocarbon analyzed from boreholes outside the Ceja survey shows biomarkers that correspond to type II kerogen associated with the marine/deep marine organic matter of Devonian age (DeGarmo, 2016; Ekwunife, 2017).

The Brittleness Index in the Devonian Woodford shale shows a linear correlation with a thinner isopach. In this portion of the survey, the pre-existing topographic highs (controlled the Woodford deposit). At a borehole log scale, the Woodford shale has a low brittleness index response at the top and bottom (0.1-0.4). However, it has a higher response (0.4-0.7) at the center. The thickness in the Woodford is below seismic resolution at this depth (~60 meters) (Figure 2-29). To gain a better characterization at seismic scale, the geocellular model guided the extrapolation of the mechanical properties. The depth seismic section on (Figure 2-29), show the thin interval of the Woodford shale represented by the red envelope. Also, the seismic section converted to depth shows the irregularities within the basement. The parallel reflectors on the Mississippi Lime shows in contrast with the terminations on the center of the section the difference on deposition within the Mississippi Lime.

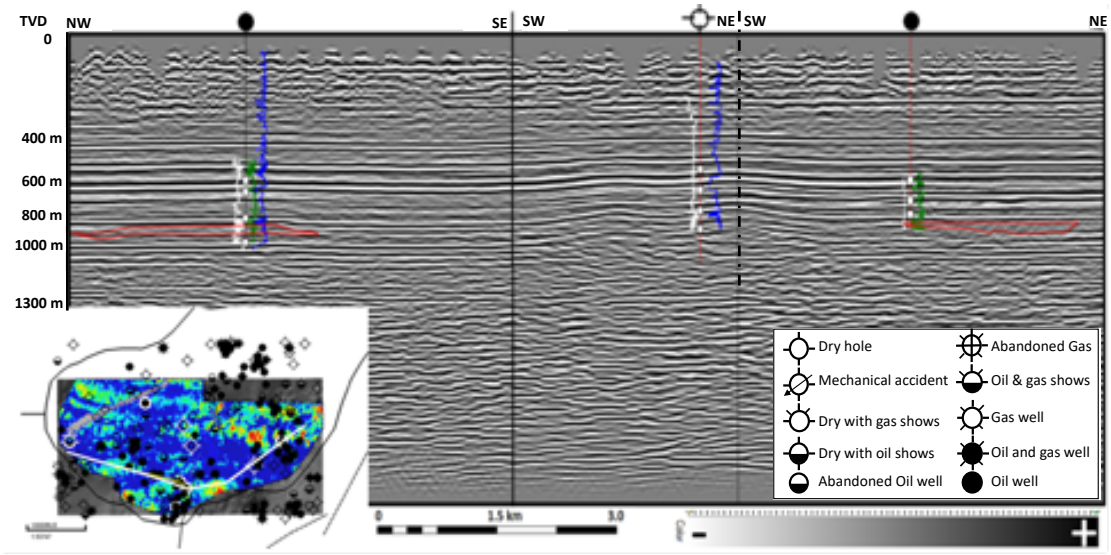

Figure 2-29.Woodford shale thickness in southwest Osage County with BI attribute extracted on the surface interpreted as the Woodford shale.

One possible scenario is the massive fluid migration from south to north thru the Mississippian/Devonian unconformity. Moreover, the Devonian Woodford shale is almost absent in this portion of Osage County, but west of the Nemaha Uplift and south of the Cherokee platform represents one of the most prolific plays in Oklahoma (Roy et al., 2013). In general, the Brittleness Index characterization of the Woodford shale in the survey shows low values associated with less brittle lithologies. The differences in fragility in the Woodford could that suggest fractured siliceous shales create matrix permeability (Slatt & Abousleiman, 2011). However, the natural characteristics of the limestone created by several cycles of deposition result in thin-beds of argillaceous limestones. The present vertical fractures can generate pockets in the Woodford shale. Without a doubt these fractures would be below seismic resolution and below wireline log resolution, but the lower contrast in brittleness index can described by the average effect on the properties.

Woodford shales in this portion of the study are sub-economical due to the maximum thickness (~30 meters). Erosion and local basement depressions can promote isolated basins filled with organic shales, but the lateral extension is controlled by the karstification and internal connections, which is appreciable in the Brittleness Index attribute (Figure 2-30) extraction along the surface equivalent to the Woodford formation suggest that drilling horizontally in this formation would not yield an extended increase of production. A campaign of horizontal drilling in these conditions suggest that the Woodford shale it is not a candidate for conventional horizontal drilling and completion.

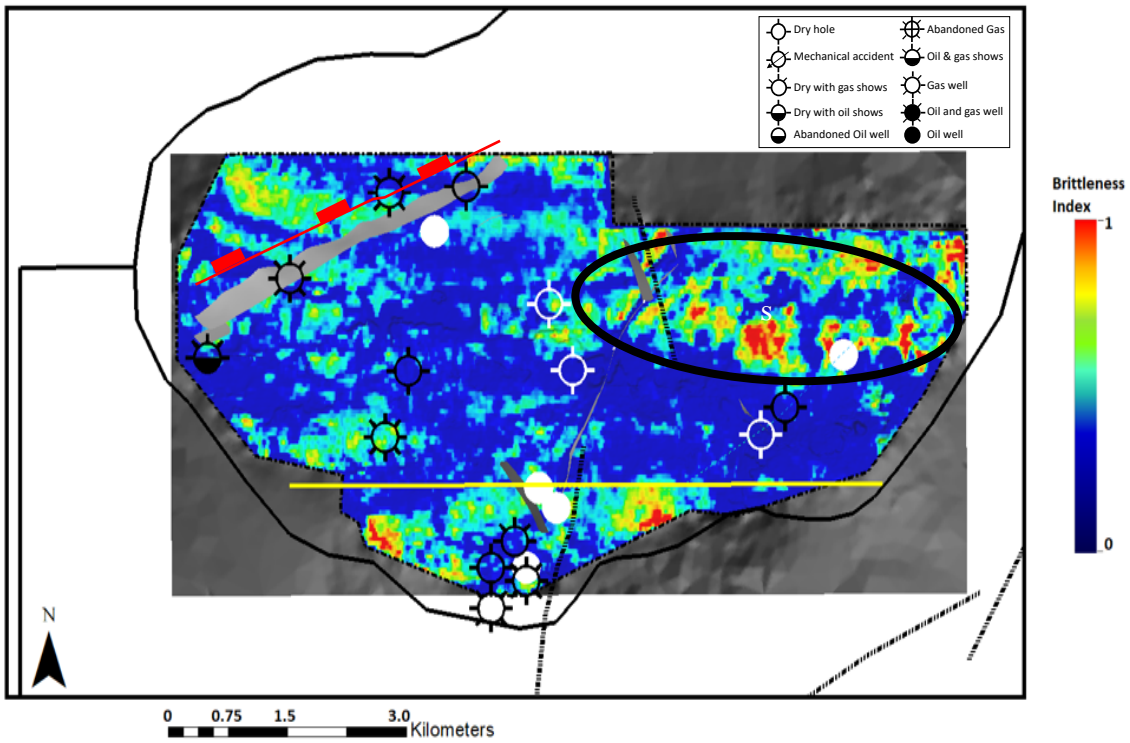

Figure 2-30. Maximum extraction of BI attribute on the Woodford shale. Displayed on the figure, the boreholes with reported production from the Woodford shale and a normal fault on the west portion of the study area.

The low brittleness values of the Woodford shale in Fig. 2-30 coincide with the results of the wells that have tested the hydrocarbon potential of the Woodford shale. Higher BI values (0.6-1.0) agree with the highest gas production from these wells. The extraction shows potential areas for drilling and completion. These potential areas are located northeast of the survey highlighted by the black ellipse. On the other hand, the results from the boreholes in the center of the survey correlate with low BI values, which suggest that production is partially controlled by mechanical properties. Another factor to consider is the impact of fault migration timing. The interpreted normal fault to the west accommodates large space to deposit shale sediments, the higher BI values show a good correlation with in this portion of the survey and with hydrocarbon production. In the east of the survey, the higher BI values show untested results on the Woodford shale that could potentially become prospective.

Brittleness Index attribute generated in this thesis also shows a weathered basement. We know from other studies and outcrop descriptions that the basement top is an irregular surface. The curvature attribute depicts these irregularities as a positive curvature value Figure 2-13. Below the basement top, a lower BI value would be higher than in the sedimentary layer but lower than its context, in the basement. The time to depth conversion sets the basement depth from 900 to 1300 m (Figure 2-30); the shallowest portion is located at the southeast of the survey, product of a strike-slip tectonic event which created a right lateral transpressive event that aborted the block and generated a series of relay ramps. The principal curvature shows a good correlation on the interpreted basement structure.

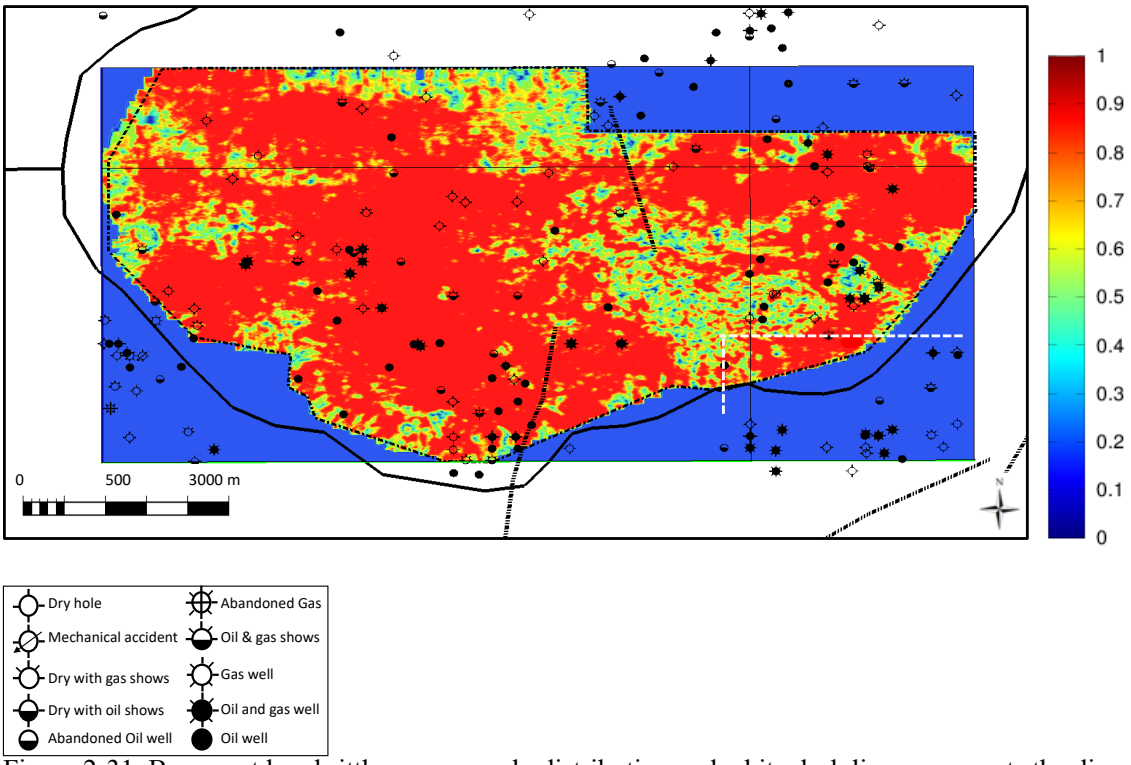

Figure 2-31. Basement low brittleness anomaly distribution and white dash lines represents the direction of the section on Figure 2-25. Location of borehole A and B shows the borehole result.

The fracture set in the basement has a general north-south orientation, and is represented by the fault likelihood attribute Figure 2-16. The faults are misoriented, since the maximum horizontal stress is oriented almost E-W. This orientation could be one of the reasons why nearby are significantly less earthquakes triggered in Osage County. One of the boreholes in the southeast of the survey found the basement top at 1090 meters; the top basement was profoundly altered. At 1160 meters the borehole drilled a low-velocity zone, and the pore-pressure profile showed a drop in the pore pressure. The thickness of this low-velocity and low-pressure anomaly is around 60 meters. The velocity reduction is close to half the basement velocity 3000 m/s to 3200 m/s. The distribution of this anomaly is represented on Figure 2-31.

The low-velocity anomaly also has low Brittleness Index that extends parallel the top of the basement, but also quasi-vertically that matches the fault interpretation with high angle faults (Figure 2-14). One of the advantages of including the drilling parameters is that there is direct evidence of the drilling performance. The borehole, API- 3511303730000 to the west structural high, drilled 70 meters in the basement with a sizable drilling mud loss. Mud losses during drilling are categorized to take mitigation steps; a severe loss of circulation is typically associated with fault reactivation. In this case, the borehole was drilled on the west flank which accordingly to the BI attribute potentially connected a low brittleness zone on the basement to shallower stratigraphical units. A loss of this magnitude likely requires a large cavern or fault plane to accommodate the fluid volume.

My calculations have a ten to fifteen percent error as the logs are recorded from different companies and at different time, plus the seismic inversion correlation has close 70% correlation, which suggest an extra error associated. The uncertainties are too many to mention, as each value would need to be calibrated from wireline logs. The petrophysics analysis I made helped to understand the water saturation and clay content on a reservoir unit given the limited information available. In order to further calibrate the porosity and carbonate content on the formation more information is required (Elemental capture spectroscopy logs, core information, multi dynamic formation testers, chemical analysis on the reservoir water, etc.)

2.7 Conclusion

Moving from regional, general observations to the site and physical property specific observations enhances the understanding a geoscientist can gain concerning the challenges of our current energy landscape. Significant uncertainties exist in the mechanical/ petrophysical properties that control production, both in the conventional Mississippi Limestone and the un-developed Devonian Woodford Shale.

In conclusion, I found the correlation of higher production with higher Brittleness Index. I also found that the faults connect the basement but the anthropogenic pressure disruptions (Petersen et al., 2016) are less severe as the faults are misoriented. The interpretation was validated through the use of potential data, seismic information and borehole wireline logs. Also, by translating drilling information into useful geoscience data.

The third important conclusion is that Osage carbonate reservoirs, in specially the Mississippi Lime have vertical seals that add to the heterogeneities of the reservoir rock and the production randomness. That is, high productive wells next to low productive wells. The fourth conclusion from this study is that even though there are two zones mechanically interesting for hydraulic fracture in the Woodford shale. The thickness in general in this portion of the Osage County might not be economical (thickness $\leq$ 30 m).

The lithofacies analyzed using borehole response shows the following summary; Brittle lithologies are associated with calcite-rich rocks and igneous rocks. An average behavior of the BI is associated with quartz-rich sandstone deposited as meandric facies in a regressive system track.

Coarser grain sandstone shows as a lower brittle lithology. Less brittle lithologies are associated with shales and transitional clay-rich sandstones. The boreholes drilled in the area attest to this kind of mechanical behavior.

Since brittleness is a function of mineralogy, stress conditions, and elastic properties the spatial constraints impact and control these parameters, i.e., shallow water carbonates exhibit a larger porosity system and are profoundly affected by erosion and other diagenetic effects than open water carbonates. Hence the facies per lithostratigraphic group controls mechanical properties and breakable behavior. The higher resolution brittleness index, a 3D attribute computed from the integration helps to better understand the Mississippian chert, one of the reservoir facies in the Mississippian Lime formation. The shallower play, the Mississippi cherts is complex. It is composed of diagenetically altered cherts deposited at the highpoint of the basement. The cherts exhibits a higher porosity in contrast with the limestone but lower/irregular permeability mechanisms. The chert diagenesis shows a local correlation with basement topography. Carbonate diagenesis is likely created due to the silica fluxes thru faults/fractures from the basement. Lithologically, the alternating beds of cherts and mudstones are responsible for horizontal and vertical discontinuities in the Mississippi Lime. Moreover, karstification and sinkholes collapse exacerbates the discontinuities. These heterogeneities make it a challenging play and a weak candidate for hydraulic fracturing to enhance permeability.

The advantage of creating a geocellular model that accounts for the procreational depositional architecture and differentiate stratigraphic facies from mechanical facies (i.e., small grain limestone vs. argillaceous muds) is that more information can be easily updated into this

model. Also, the geocellular model helps to generate several discrete reservoir facies with mechanical properties and extrapolate these facies, guided by seismic attributes, seismic inversion, and geostatistics.

Brittleness Index in this work makes it feasible to discern the impact of pre-existing basement structure and paleo-deposition environment on the complex interplay of sequence stratigraphy and mechanical properties. The BI attribute shows that high values correlate with higher production and are not always associated with structural highs but have an irregular distribution. In this thesis, I showed correlation of the current hydrocarbon production and borehole status, in the Mississippi Lime with mechanical properties. A higher BI correlates with larger production. Moreover, the ROP's in the Mississippi Lime changes as chert is harder than in the argillaceous limestone. The difference in drilling velocity could have several origins, but one of them could be the higher rock fragility that breaks with more ease thanks to the higher porosity and the stiff matrix of the chert (Qi, 2018). Drilling and completions engineers could potentially benefit from understanding the fragility of the formation of interest. The mechanical facies classification can assist in driving the appraisal campaign; the water injection well spacing, and evaluating the frackability of the formation of interest.

In particular in Osage County, as a conventional play, the Mississippi Lime does not need to be hydraulically fractured, mainly because the resources needed to create an active fracture would be uneconomical. My analyses show that areas of high brittleness are more prone to connect compartmentalized reservoirs by improving the water injection borehole location. Currently, the enhanced hydrocarbon recovery methods used in the area are; water well injections and artificial

lifting mechanisms (acidification treatment, gas lift, and reservoir electrical submersible pumping). However, water injection well location effectivity is tightly related to horizontal reservoir connectivity, but also to vertical seals. A less brittle formation would inhibit fracture propagation. The seals are fewer brittle shales whereas the reservoirs are fragile lithologies that have a stiffer matrix skeleton but high porosity, therefore the fracture displacement is more rapidly deaccelerated and dissipated in less brittle -shale-like lithologies. The BI accounts for this facies classification.

Currently, unconventional resource plays in other areas of Oklahoma are among the most active plays in the United States, with oil production ranking second/third in the most drilled-areas. Osage County has lingered, ranking 66th in production in the state. I showed an integrative approach to derive Brittleness Index for important stratigraphic units in this area. The BI attribute demonstrates the challenges developing the Woodford shale play might represent in this portion of the basin. First and foremost, the shale thickness in Osage County is almost a third in comparison with that in the Ardmore basin of central Oklahoma. Secondly, in portions of the study where the Woodford shale might be thicker (~90 meters), the BI extraction on the Woodford shale suggest a less brittle behavior (Figure 2-30). This mechanical behavior of the reservoir could potentially make fracture length sub-economical (Slatt & Abousleiman, 2011). To improve Woodford frackability, this work shows that the proximal facies of the deposited shales on karst-like features have a higher frackability index. A higher Brittleness Index makes the fractures grow along brittle beds easier than in less brittle beds. A less brittle lithology such as argillaceous muds with high total organic content. From the borehole production analysis, the values between 0.4 and 0.7 on BI scale are more favorable for connecting the larger reservoir (Slatt & Torres-Parada,

2014). Drilling and completing in facies with this BI value could potentially increase production if completed in this area.

Including the Brittleness Index computation in the set of elastic properties bolsters near-field development. The Brittleness Index represents the relative ability of a crack to propagate through a stressed medium. Oil flow rates in the area show low production rates in wells in the north portion of the seismic survey, where BI is low. On the other hand, higher BI in the south portion of the study area shows the potential of the rock to be completed by secondary stimulation, either acidizing the reservoir or hydraulic fracturing. The Brittleness Index shows higher values that potentially could suggest ease of fracture propagation; in other words, the higher value of BI the geometry of fracture could potentially be more extensive. Drilling and completion technologies remain the state-of the art, but the location of by-passed resources is a task for geoscience. In mature areas, different streams of information should converge rather than disagree. The geomechanical model from the borehole helps to set a common ground for the drilling and completion parameters.

Chapter 3 Velocity anisotropy analysis from an outcrop sample of the Woodford shale in southern Oklahoma

3.1 Introduction

Devonian shales, in particular the Woodford shale in Oklahoma have played a crucial role in the hydrocarbon landscape, first as a source rock and in the last decades as a reservoir rock (DeGarmo et al., 2016). Like most materials, the Woodford shale exhibits an anisotropic and heterogeneous behavior when evaluated at different scales (Vernik & Liu, 1997), especially at the scales of interest of completion and drilling engineers.

Shales shows different acoustic characteristics since it encompasses the most common causes of anisotropy; stress, layering and, fractures. In this work, I measure shear and compressional velocities at different frequencies to evaluate and characterize anisotropy in the Woodford shale.

Different studies have deepened our understanding of this complex reservoir. Since the early 1990s (Kirkland, 1992) the McAlister cemetery quarry has been serving as a field laboratory, due to its well-preserved exposure of the complete section of the Woodford shale. Different studies on this outcrop have served as analogies for subsurface correlations.

The outcrop has presented excellent accessibility that has helped facilitate different studies such, as X-Ray Diffraction. (XRD) (Degarmo , 2016). Organic chemistry TOC and rock-eval pyrolysis to determine organic richness, have help understanding on stratigraphic and sedimentological heterogeneities (Ekwunife, 2017), on mechanical properties (Becerra, Daniela, 2017; Galvis et al., 2018) and, geochemical heterogeneities (Serna-Bernal,2013 ; DeGarmo et al., 2016).

Incorporating frequency sweeps of ultrasonic measurements of the fractured lower Woodford shale could potentially discern and apply anisotropy effects in hydraulic fracture modeling. I measured seismic velocities parallel to the bedding, perpendicular to fractures, perpendicular to bedding and parallel to fractures. I estimated the dynamic and static elastic moduli(shear, bulk, & Young's modulus, and Poisson's ratio) accounting for shear and compressional velocity differences (Sone & Zoback, 2013).

I then generated a precise geomechanical model, which resulted in a numerical simulation that allows for the quantification of the differences in fracture effects and geometry. Also, determined are the modeled fracture geometry, height and width, and fluid pressure distribution within the fracture formation boundary. The results display the impact of correctly defining anisotropy to evaluate and budget efficient hydraulic fracture jobs. The Woodford shale is of particular interest since this is one of the most drilled and completed plays in our current energy landscape. Anisotropy characterization, combining geology and reservoir engineering is paramount for borehole placement and well landing. Correct estimation of anisotropy at different frequencies aids in discerning the causes of anisotropy that could potentially drive completion designs and better budgeting of financial resources.

3.2 Geological background

The outcrop is located at the southern edge of the Ardmore Basin close to the Marietta Basin in Carter County (Figure 3-1), which makes it an excellent location to correlate subsurface properties to the buried Woodford in these basins. Outcrop gamma ray measurements and other studies done

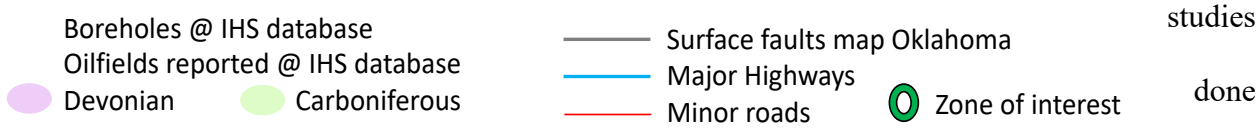

on the Woodford shale have allowed the correlation of physical and chemical properties to boreholes that have drilled the Woodford shale at other depths (Duarte, 2018)

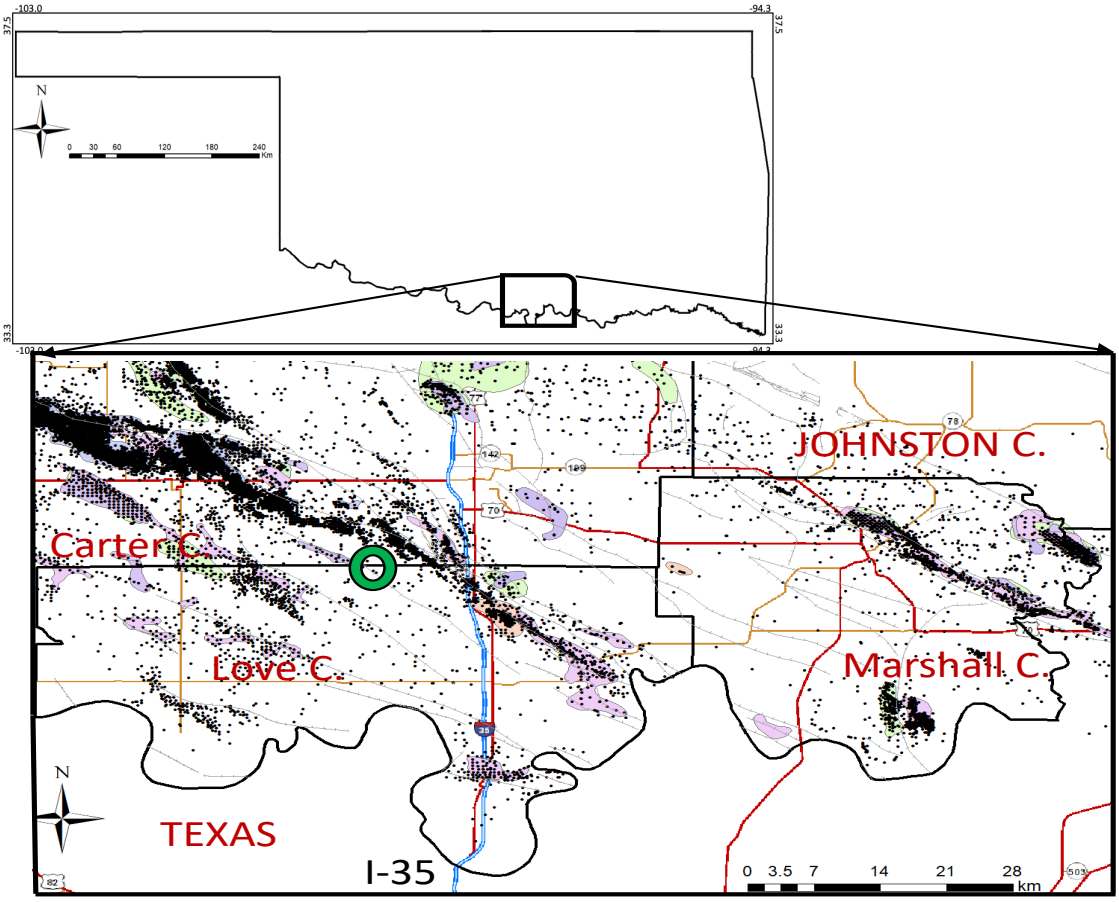

Figure 3-1. Location of the Woodford outcrop were the sample was collected. Abundant production has been documented from the oilfield's northwest and west of the outcrop.

The Woodford shale is an organic-rich, dark gray-dark green siliceous mudrock with sporadic horizons of chert and phosphate nodules, represented by light-colored shales (Galvis et al., 2018). The stratigraphy, is a 2nd order cycle deposited (Slatt et al., 2012) unconformably on the Hunton group (Figure 3-2).

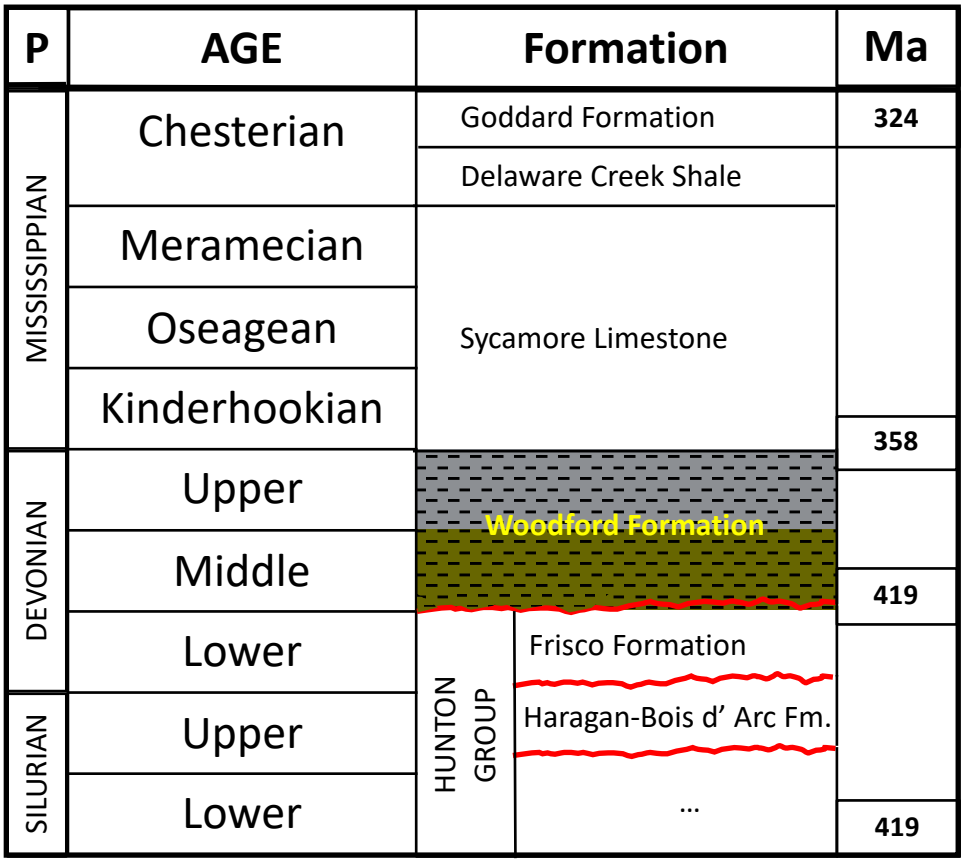

Figure 3-2. Stratigraphical chart of the organic Woodford shale deposited from 388 to 359 Ma(stratigraphic chart from (Johnson & Cardott 1992; Bernal, 2013).

The Woodford shale was deposited during the Devonian age at sub-equatorial/equatorial margins in a marine setting it is a 2nd order depositional sequence ~ 29Myr. As the proto continent was opening to the south, it had deeper waters towards the south as opposed to shallower marine waters to the north (Kirkland, 1992; Keller et al., 2007).

Typically, in the Ardmore Basin, the Woodford shale is underlain by the late Ordovician-Silurian, with a contact marked by a significant regional unconformity developed in the late Devonian (Beccera, 2017; Slatt,2018) (Figure 3-3).

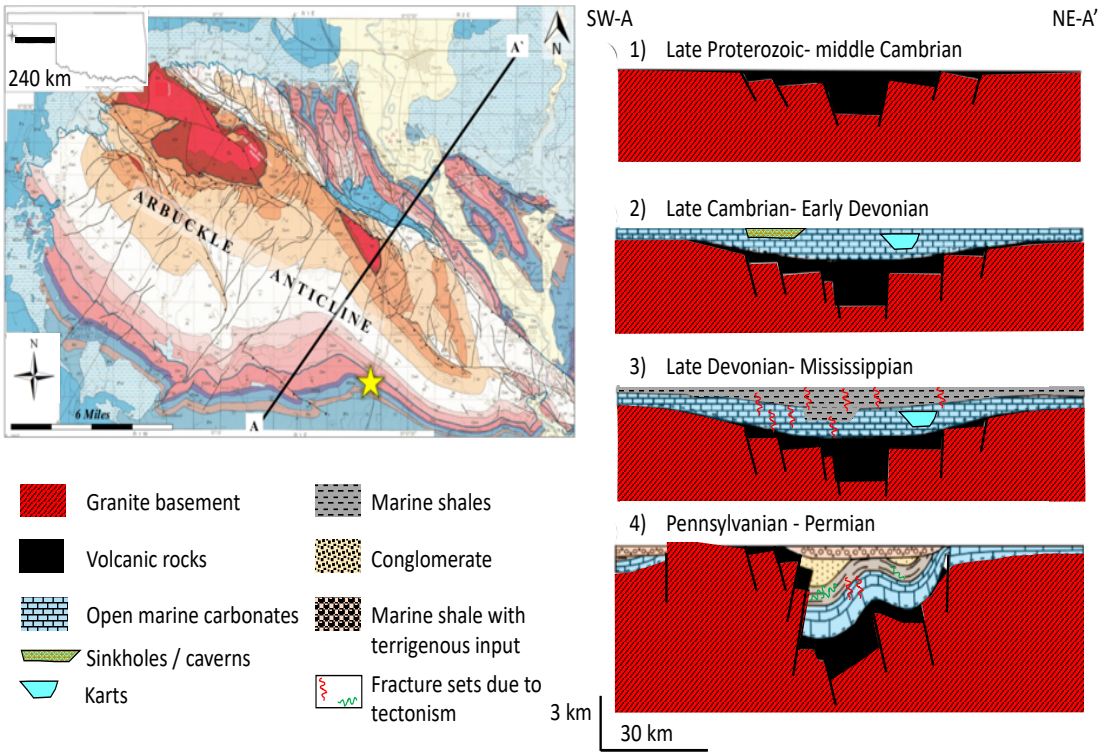

Figure 3-3. Structural schematic sections showing the evolution of Southern Oklahoma (after Ataman 2008; modified from Bixler, 1993).

Figure 3-3 shows the depositional stages of the Woodford shale. My interpretation from the Ataman (2008) is that the first stage (1) Graben stage, faulting and syn-rift deposits with volcanic rocks. (2) Subsidence and accumulation of open shallow marine carbonates on near the equatorial margin along with erosion and diagenesis of carbonate rocks (3) Subsidence and deposition of open marine shales, this deposition might also take place on the weathered carbonates deposited creating isolated basins and vertical fractures. (4) Folding and faulting (Wichita and Arbuckle uprisings) that intensified the fracture on the stratigraphical units. (map from Stanley et al 2012, section modified from Ataman 2008 and Bixler, 1993)

The lower Woodford shale is marked by clay-rich and fissile behavior whereas the upper Woodford is characterized by interbedded chert and fissile shales that contain variable amounts of

clays and carbonate minerals (Milad et al,.2018). Another critical difference between the lower and upper formation is the organic richness in the lower formation. The level of thermal maturity (Cadott, 1990), and its high gamma-ray response (Ekwunife, 2017). The sample I collected is from the Upper Woodford, with the beds striking N40ºW and steeply dipping 35 ºW (Figure 3-4).

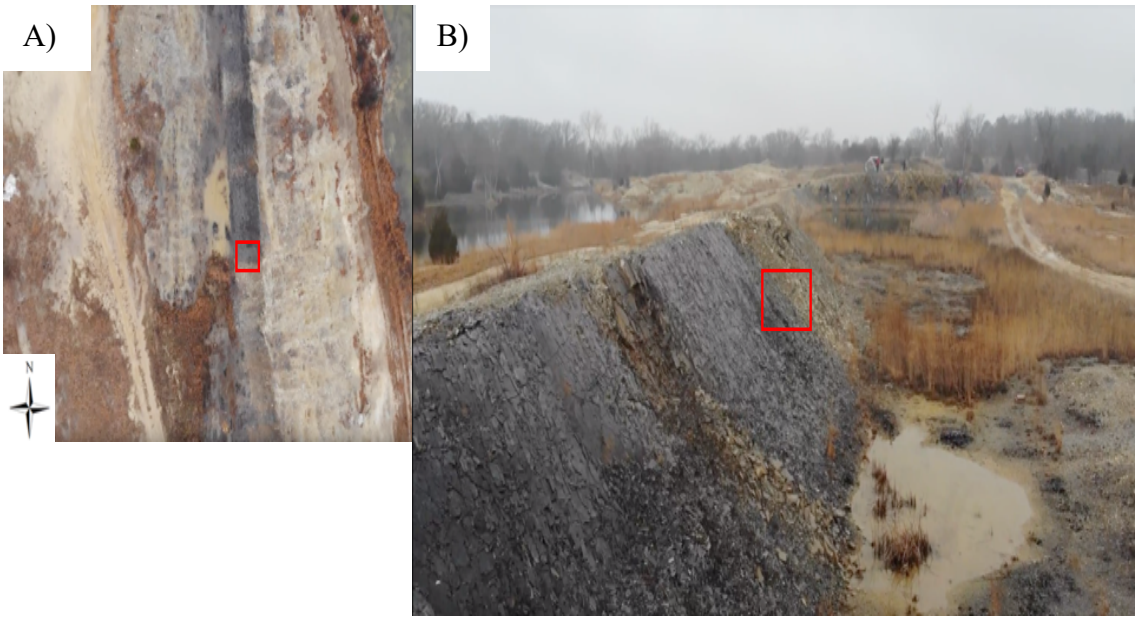

Figure 3-4 . A) Top view of the Macalister outcrop is from Google maps to show the color contrast between formation contact and dip of the formations. B) North-South view of the outcrop I took the photo during a field trip to the McAlister cemetery quarry. The red squares represent the area of where the sample was collected.

Fig. 3-4a shows a discernable contrast in rock color (dark gray versus light gray/greenish), the red square represents the location where the raw sample was collected for further laboratory preparations and measurements. Fig. 3-4b shows the side view of the outcrop. The dark shales are extremely fissile with layer thickness from 5 mm to 15 mm. The outcrop lithology is divided by mudrock (non-fissile/massive mudrock) marked by dark green with orange tones and clay shale (fissile clay rock) manifest by dark bituminous shale. It is noteworthy the contrast in color that occurs rapidly on the outcrop. Organic studies show that it is prone to kerogen type II, a rock

highly fragile in overlaying with the massive mudrock (Milad et al., 2018). This lithology exhibits papery stratification; the mudrock has a higher Young is modulus and higher Poisson's ratio which creates a more favorable pathway to propagate stress and have a massive bulk composition with no clear stratification. However, the mudrock exhibit a more brittle behavior and the fractures are present on this rock (Figure 3-4).

I showed a more competent outcrop in Figure 3-5, based on the different lithologies (Becerra, 2017) which accounts for the fracture sets. The contrast in the lithology within the Woodford shale creates three different characteristics besides color and stratification that are worthy to mention; First, the bitumen in the shale is embedded in the matrix. Studies suggest that bitumen in matrix reduces the stiffness of the rock matrix (Sayers, 2013b; Vernik & Liu, 1997). Second, the mudrock has bitumen embedded only in the fractures-oriented N-S. Third, the clayrock does not exhibit any vertical or oblique fractures, while the mudrock is highly fractured, and the intensity of fractures decreases with thickness. This difference in physical behavior and its components, becomes important when the reservoir rock is fractured using hydraulic fracturing.

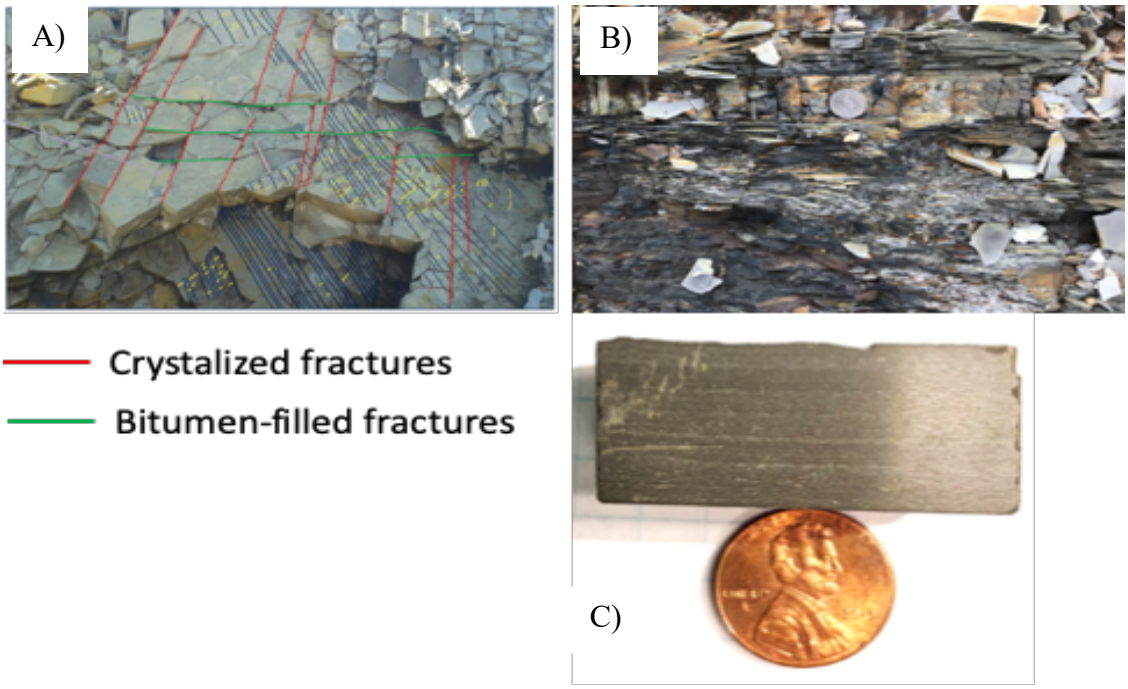

Figure 3-5. A) Fracture sets present in the mudrock on the top of the outcrop photo by (Ghosh, 2017). Two main sets are product of tectonic events, other fractures are post exhumation. B) A zoom on the outcrop, the siliceous mudrock is intercalated by shales, contains few to no fractures in core and outcrop hand sample, and exhibits a papery to platy stratification. The vertical fractures are only evident on the massive rock and are perpendicular to the clayrock. C) The massive texture on the mudrock with siliceous bed intercalated. (B and C) are pictures taken by me.

Due to the high contrast in elastic parameters of the rocks, the bitumen is emplaced by two different mechanisms in these lithologies. In the mudrock, the vertical fractures stop at less brittle layers, that is the clayrocks. The bitumen is emplaced in the vertical fractures. On the other hand, the stress is attenuated by the layering and the layers are strained and accumulating the bitumen in these horizontal layers.

In the outcrop, four fracture sets are visible. However, the principal ones are oriented to the north-south and east-west (Milad, et al, 2018). The smaller fracture sets are due to weathering and erosion, post exhumation. The fracture in the siliceous mudrock plane thickness is around (0.3 -1.0 mm) filled by dark solidified bitumen. The rock sample for this study is dark greenish, with a

light brown tone due to the weathering. The weathered rock sample is dark-gray with orange tones. The bitumen filled fractures are north-south and the crystalized fractures are all mostly east-west. The timing for the bitumen emplacement suggests two different fracture events, the first one being the bitumen filled fractures (Galvis et al., 2018). After I prepared the sample and removed all the irregularities and asperities on the surface to enhance the sensor coupling. The sample is dark-brown a cylinder with massive texture and with sporadic siliceous laminae (0.5 to 1 mm). A whole organic geochemistry and source rock evaluation from the upper Woodford shale shows TOC values ranging from 6.48 to 22.0 wt %, kerogen type I (Ekwunife, 2017; Slatt et al., 2014, 2018)(Figure-3-6).

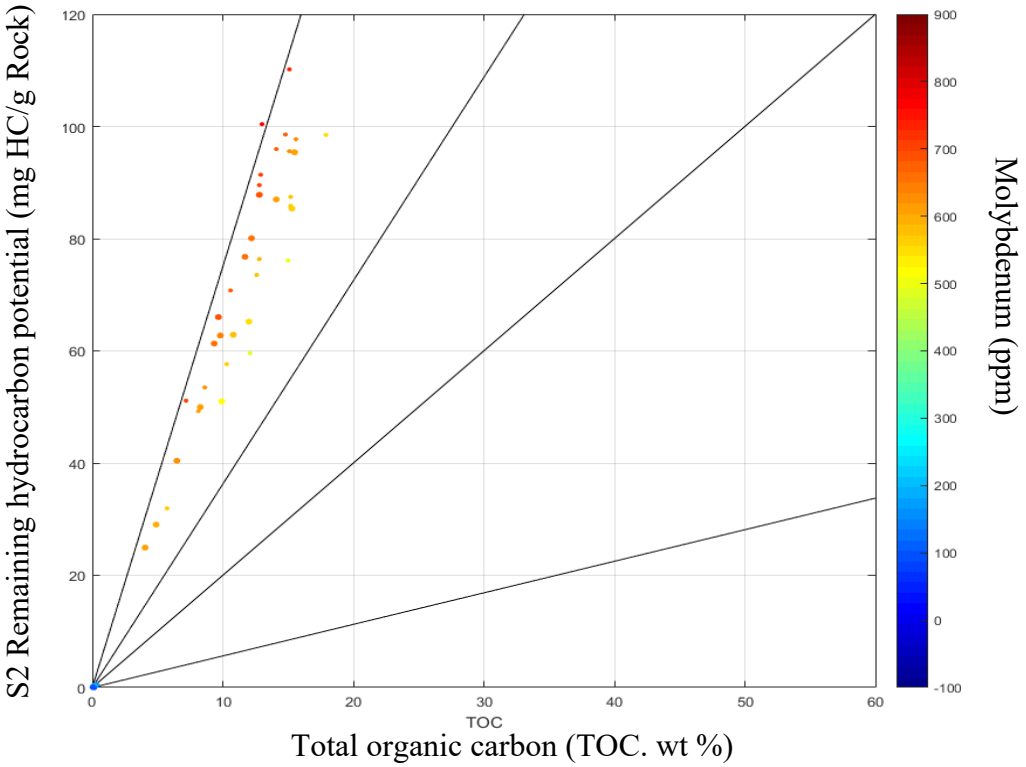

Figure 3-6. All organic matter plots on the type I kerogen, which is lacustrine kerogen. The high Molybdenum concentration (Algeo et al., 2009) suggest a less restricted depositional environment, typical of an open lacustrine environment with sporadically water input from outer sources (data collected & analyzed in (Ifunaya, 2017).

The Molybdenum vs TOC plot indicates a less restricted depositional environment for the plotted elements. Which could be explained by an open lacustrine environment where water inputs are transitionally inputting to the system. The Molybdenum is highly sensitive to redox environments and this is why it is useful here. Figure 3-6 shows the varying basin restriction during the deposition of the Woodford shale.

The thermal maturity assessment shows upper Woodford shale contains un-matured kerogen (Figure 3-7), Kerogen and depositional environment shows a trend to produce light hydrocarbon, gas and condensates (Galvis et al., 2018; Slatt et al., 2014).

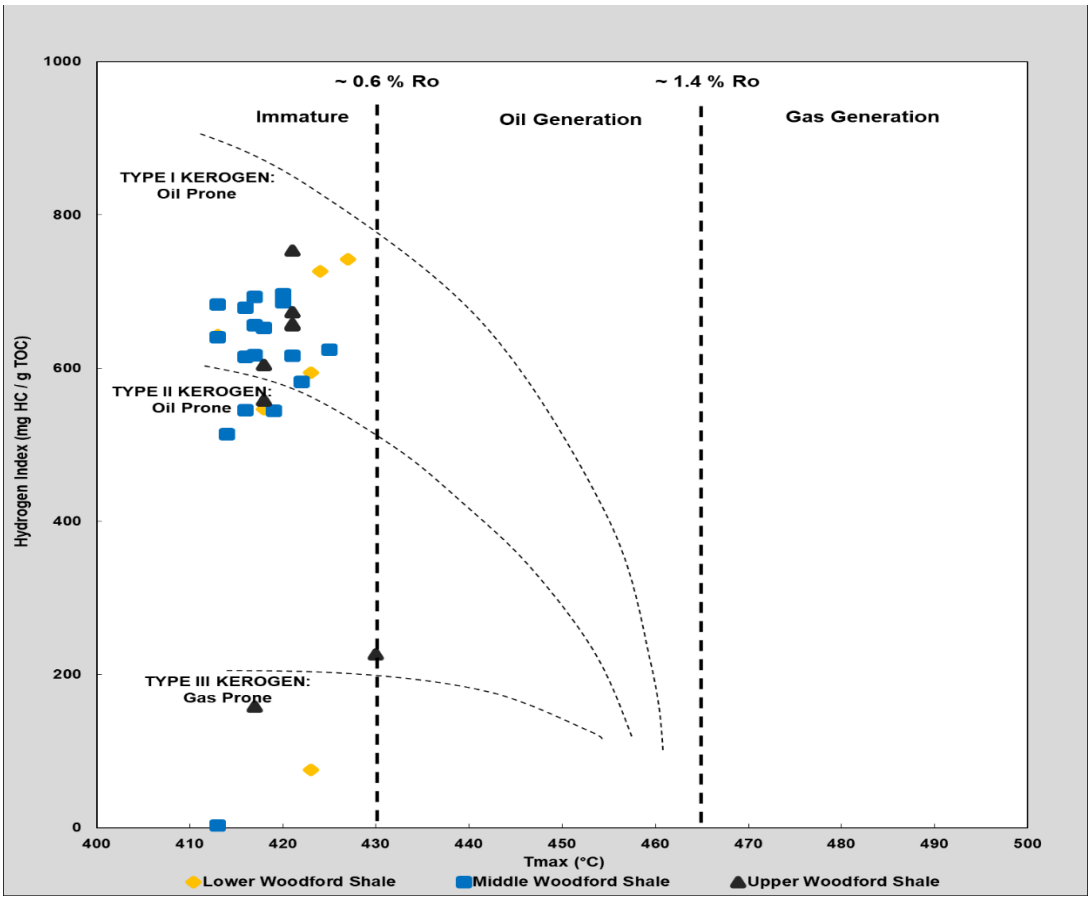

Figure 3-7. Kerogen type and maturity assessment of the Woodford shale of studies conducted from (Bernal, 2013). The type of kerogen present (Type I, II, and III) is dependent on the different hydrocarbon produced with increasing thermal maturity (Ifunaya, 2017).

Analysis from TOC and thermal maturity shows a predominance of Type II kerogen, the high presence of Molybdenum suggest a reduced in oxygen environment of deposition in Ardmore basin (Degarmo et al., 2016). Thermal maturity from Fig. 3-7 shows that the Woodford has not entered on the light oil window threshold.

3.3 Methodology

For screening anisotropy, I used three manufactured sensors made of Lead Zirconium Titanite (PZT) crystals of 18 mm diameter and 4 mm thickness. From those three sensors, two sensors are P- (compressional) wave and one was S- (shear) wave. The manufactured sensors have a corner frequency of 500 kHz and a polarization angle of 90° for the compressional sensors, and 180° for the shear sensor. The ultrasonic sensors are ideal for non-destructive testing and measurement of materials due to the short wavelengths they can detect.

The rock sample was prepared, and four different cylinders were created (Figure 3-8). Three of the cylinders have a size of 5.50 cm length and 2.54 cm diameter; the other one has 2 cm diameter and 7 cm length. The samples were surface grounded using a CNC surface grinder to remove imperfection up to 5 μm and to make the sample parallel (0.01 mm).

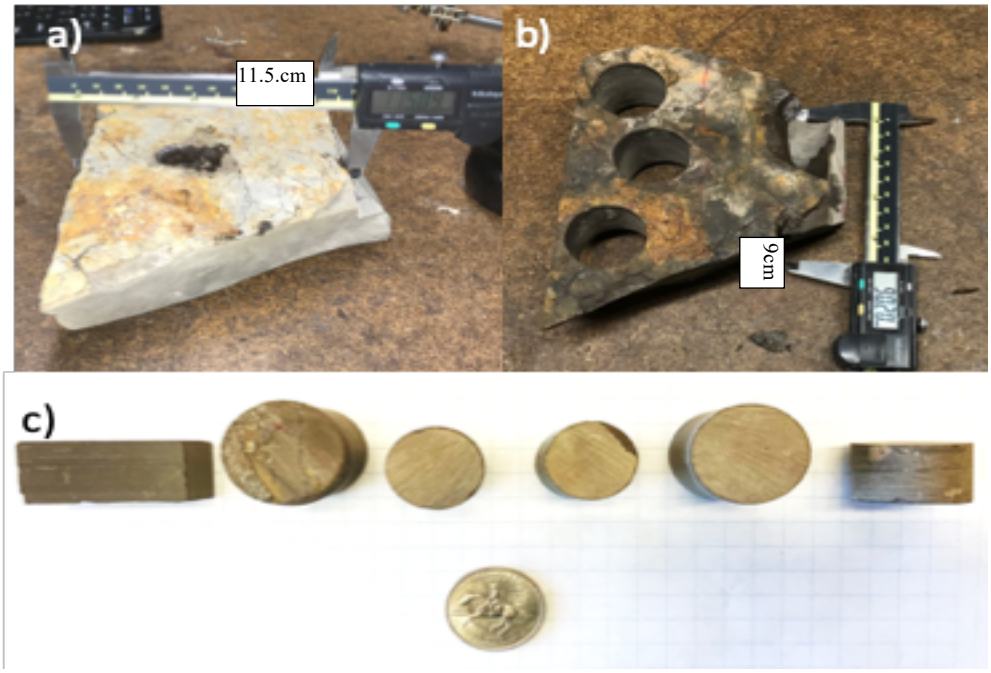

Figure 3-8. A) Mudrock sample from the quarry before undergoing the process of core sampling. It is a light gray with orange tones and bitumen filled fractures observed. B) Mudrock sample after collecting the four plugs, the change in color is due to water and other additives (grease) interaction during the core drilling. The change in color also gives inference on how the fluid can quickly interact with the rock. C) Plugs and rock sample after removing surface asperities.

The sample, that was obtained from the outcrop has an irregular shape and raspy surface. After coring the sample, I recovered four different plugs, three of those four plugs were drilled parallel to the fractures, and have a diameter of 2.54 cm and five centimeters in length. A fourth plug was drilled perpendicular to the bitumen fracture plane with a 1.25 cm in diameter and 8 cm in length. All plugs have at least a 1:2 ratio.

On the plugs, I performed two acoustic measurements, changing the frequency and position of the sensors on the cylinders and measuring. Before measuring the velocity profile, I confirmed the receiver response by placing the source and receiver in contact to measure the source directly.

Raw signals were amplified by 50 dB using Applied Seismology consultants (ASC) preamplifiers. Amplified waveforms from three positions were continuously saved by ASCs

Richter acquisition system, which has a 500 mv dynamic range. Analog data were sampled at 10 MHz and digitized at 32-bit resolution (Figure 3-9). The source was selected as a on the pulse generator as a sennoside wave.

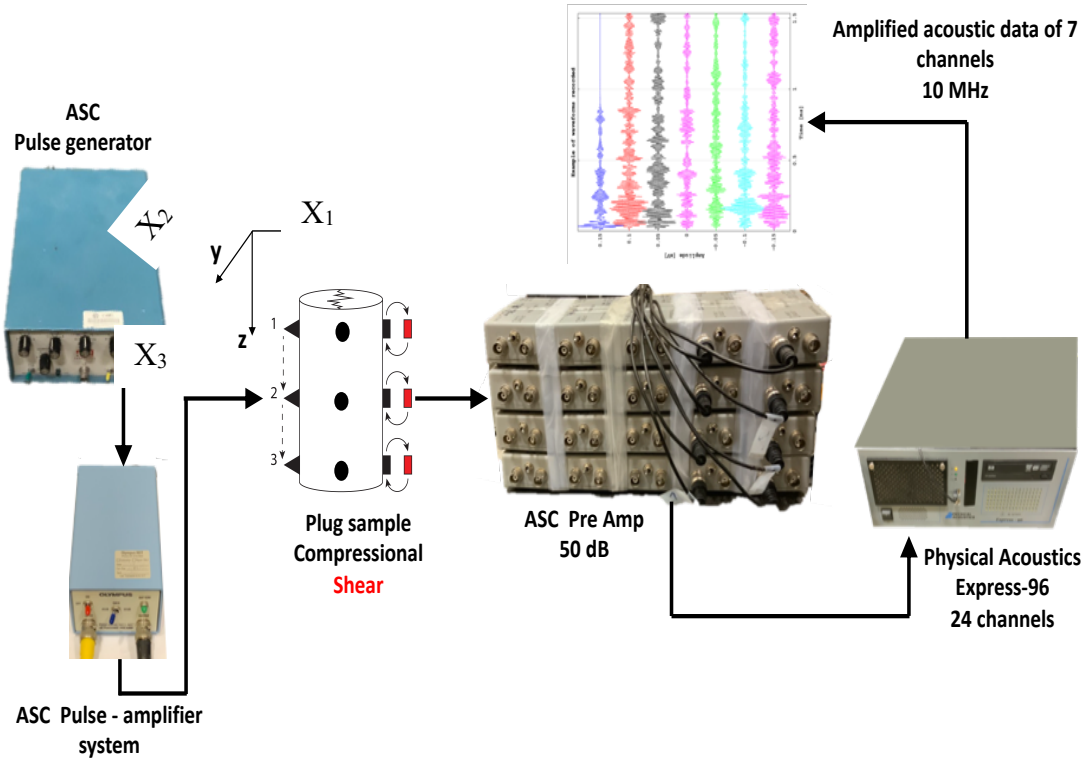

Figure 3-9 Complete diagram for active ultrasonic acquisition setup for the shale plug to screen anisotropy.

Ideally, shales will exhibit two horizontal axes of isotropy different from the vertical axis, that is, shales exhibit horizontally transvers isotropy HTI, which represents that the plane of anisotropy is perpendicular to the layering. Now for this shale sample in particular, the horizontal plane of isotropy is not relevant since it exhibits a massive behavior with some siliceous beds and phosphate nodules. The relevant plane of isotropy is vertical since the sample is fractured and those fractures are filled with bitumen. (Sayers, 2010; Vernik & Milovac, 2011).

Vernik et al (1997) makes an extensive review of the anisotropy in shale samples by varying the confining stress using the methodology of ultrasonic measurements. In his study, he highlights the dependence on TOC and kerogen content to characterize fracture dependence anisotropy and discern from the preferred direction of fracturing.

I measured parallel and perpendicular to the rock sample, as in Figure 3-10. The sensors have different polarization angles. The P-wave sensor has a perpendicular polarization, that excites the source perpendicular to the plane of the crystal surface. The S-wave sensor used in this experiment has a horizontal polarization in reference to the plane of the crystal. This means that the waves are recorded parallel to the surface of the receiver. Due to the size of the sample, I acquired the waveforms by placing only three sensors at a time. The objective of this strategy is to reduce interference. I placed the source at the first position and measure P-wave velocity straight across the shale plug on the $X_1 – X'_1$ direction and 90˚ counterclockwise on the $X_2 – X'_2$ axis. Each measurement was acquired with changing the source frequency from 10 kHz to 250 kHz before moving along the X_3-X'_3 axis the source and receivers to the second and third positions. Then I replaced the P-wave sensor with the S-wave receivers and place the sensor in the same positions and also making the frequency sweep. On the second position of the source (Figure 3-10a) I repeated the acquisition strategy and the frequency sweep for each receiver, position 2 on.

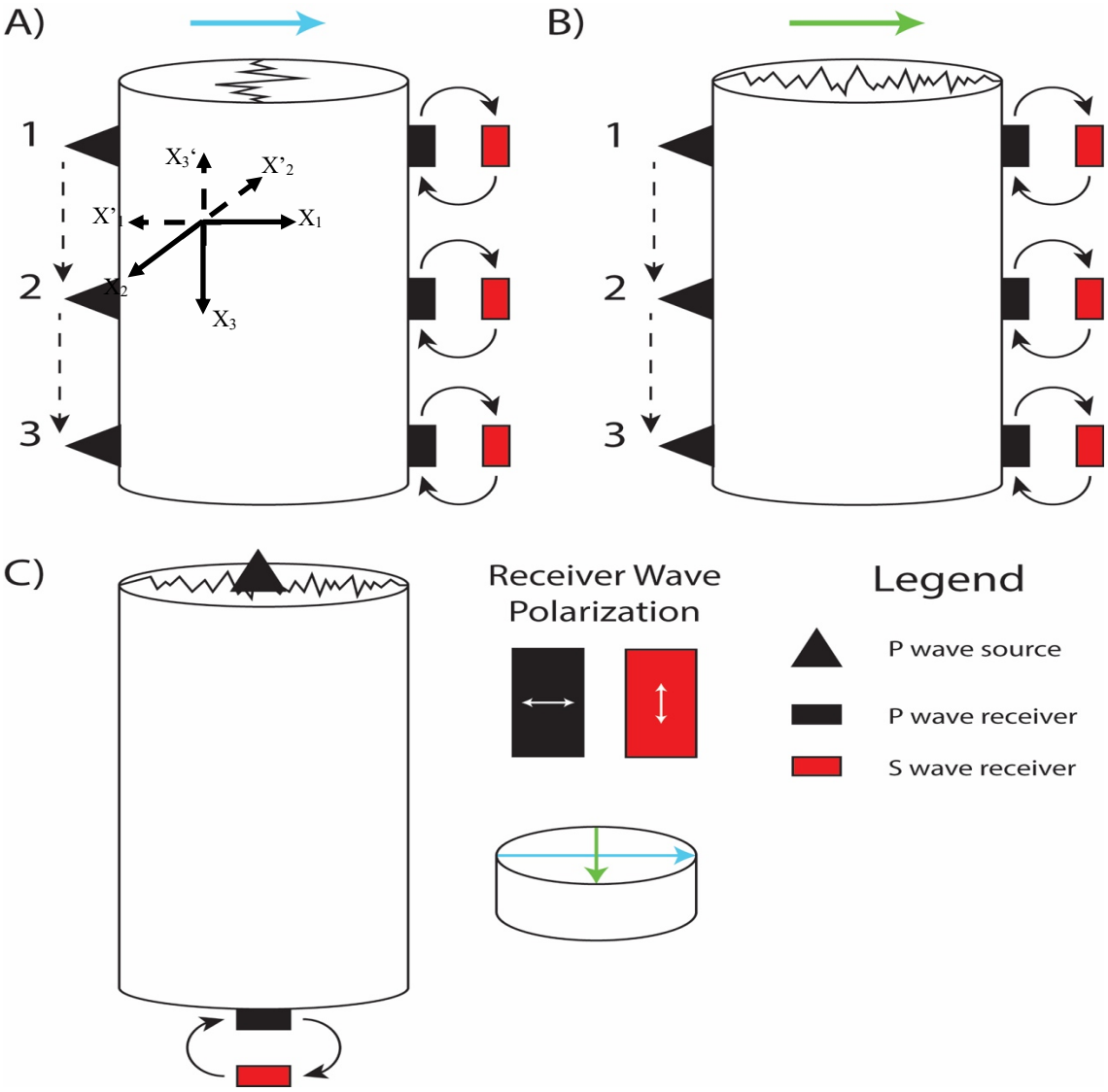

Figure 3-10. A) Acquisition diagram an ultrasonic active source used to measure first arrivals times to compute the velocity of P and S waves. Polarization of the sensors is represented on the receivers. B) second stage of acquisition with source parallel to fracture direction. C) Third stage of acquisition with source and receivers vertically oriented

The pulse transmission for velocity measurements was employed with frequency sweeps, varying the central frequency from 10 kHz to 250 kHz. The repeatability of velocity measurements (the difference between different experiments) is ± 3 % for P-waves and ± 5% to S-waves.

3.4 Wavefield acquisition and waveform analysis

In the experiment, I measured the P-wave velocity in the X_1-X'_1 direction and X_2-X'_2 direction simultaneously while activating an active source in the X_1-X'_1 plane, then moved to position 2) on Fig 3-10a and then to position 3) in Fig 3-10b. It is noteworthy that the direction of the fracture is perpendicular to the X_1-X'_1. After the three positions are recorded, the source is reset to position 1) and the P-wave sensors are swapped to S-wave sensors to change the position of the source and the receivers vertically to explore the anisotropic response on the P-wave and S-wave. Each source at each vertical position was excited on a frequency range of 10 kHz to 250 kHz to analyze the frequency dependence velocity on each direction acquisition direction.

I choose this frequency range since it is a typical frequency range for dipole borehole tools used during acoustic log acquisition. Density power spectrogram shows the peak frequency of the recorded P and S waves (Fig 3-11a). I picked the travel time using the maximum energy from the recorded waves, which corresponds to the peak frequency on the spectrograms. There is a small lag between the maximum envelope energy versus the first break. This difference is consistent, and the same attribute was used to pick the first arrival time of the 650 waveforms recorded. Each sensor recorded twenty-five shots at different frequency. The measurements are recorded at room temperature.

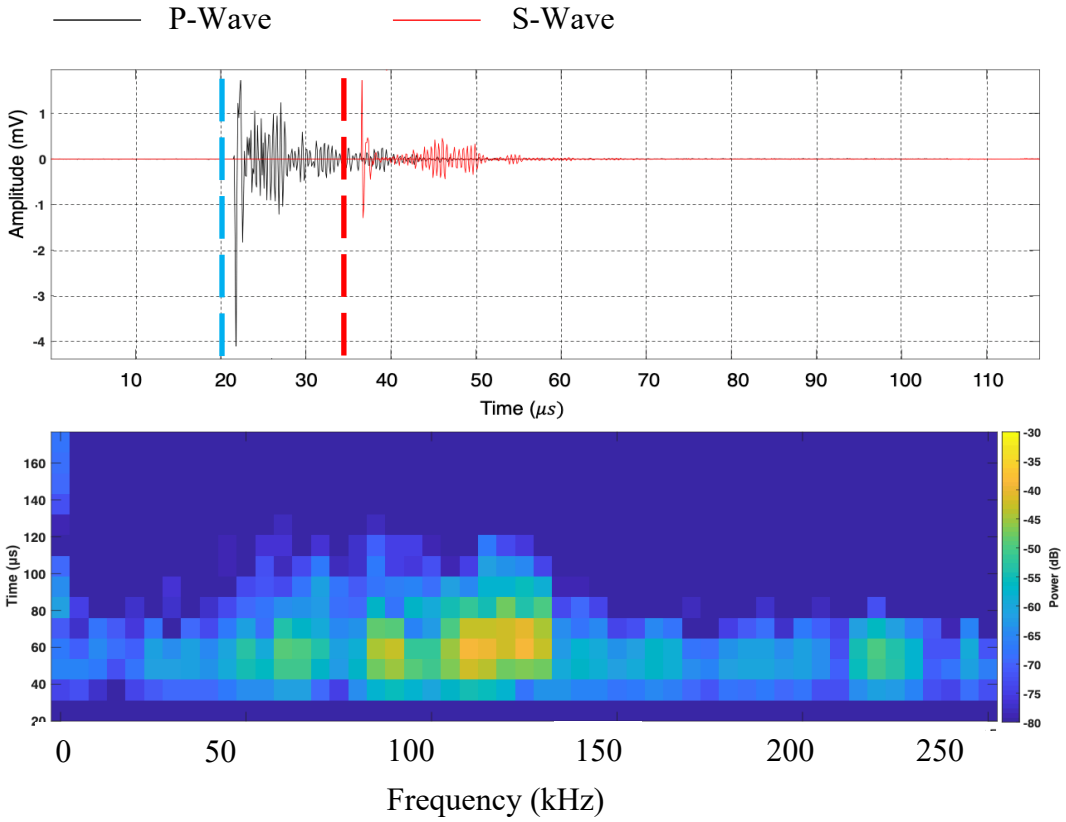

Figure 3-11. A) Waveform representative of P and S wave at a source frequency of 150 kHz. B) Spectrogram of S-wave sensor, recording a 250 kHz. The peak of power amplitude is centered at 120 kHz. The low frequency band present is due to mechanical noise in the lab.

3.5 Anisotropy screening

An isotropic region, (continuum material) is called isotropic with respect to a certain quantity of a property remains constant regardless the direction of measurement. The existence of anisotropy indicates a change in the measurement as a function of the direction of measurement. Anisotropy implies the presence of a certain order or feature. Fractured shale for example, implies the notion of heterogeneity that affects the propagation of waves thru the material. In this, case, a fractured shale theoretically exhibits as vertical transversely isotropy, where a property of the fractured shale has the same value in two directions but a different value in the third direction.

Theoretically, the vertical transverse isotropy model characterizes vertical fractured massive shales as the model (Figure 3-12).

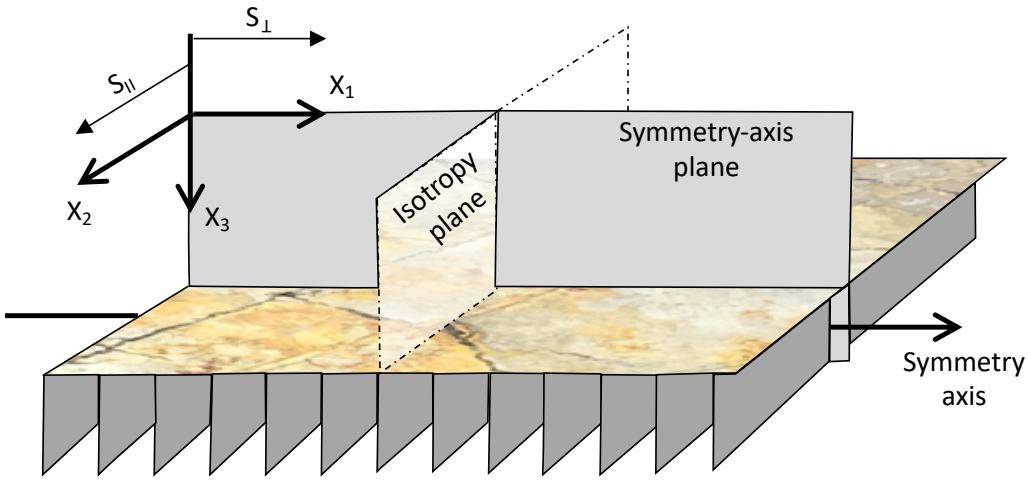

Figure 3-12. Scheme on the VTI model for fractures of the rock sample. The horizontal plane is a plane taken from the rock sample. Conceptual model from (Tsvankin, 2013).

The transversely isotropic material with a vertical axis of symmetry (VTI) has five independent moduli, in contrast with an isotropic material which can be characterized with only two independent moduli. The S-waves that travel in the X_3 direction splits into two modes; parallel and perpendicular to the fracture faces (this shear waves are more impacted by the bitumen filled fractures). VTI materials have a vertical property different from the two horizontal directions. In this work I defined the stiffness tensor C_{ij} using two Young's moduli (Vertical and Horizontal) and three Poisson's ratios (two independent vertical and one horizontal).

The C_{ij} tensor for VTI is presented as:

$$C_{ij} = \begin{bmatrix} C_{11} & C_{12} & C_{13} & 0 & 0 & 0 \\ C_{12} & C_{11} & C_{13} & 0 & 0 & 0 \\ C_{13} & C_{13} & C_{33} & 0 & 0 & 0 \\ 0 & 0 & 0 & C_{44} & 0 & 0 \\ 0 & 0 & 0 & 0 & C_{44} & 0 \\ 0 & 0 & 0 & 0 & 0 & C_{66} \end{bmatrix} \quad \textbf{Equation 26}$$

(Tsvankin, 2013)

Young's moduli, vertical and horizontal moduli for VTI formations risen from C_{ij} stiffness components:

$$\boldsymbol{E_v = C_{33} - 2\frac{C_{13}^2}{C_{11}+C_{12}}} \quad \textbf{Equation 27}$$

$$\boldsymbol{E_h = \frac{(C_{11}-C_{12})(C_{11}C_{33}-2C_{13}^2+C_{12}C_{33}}{C_{11}C_{33}-C_{13}^2}} \quad \textbf{Equation 28}$$

Poisson's ratio driven from the C_{ij} stiffness components is:

$$\boldsymbol{v_V = \frac{C_{13}}{C_{11}+C_{12}}} \quad \textbf{Equation 29}$$

Since the experiment measured the horizontal and vertical difference in shear and compressional velocity, these elastic components can be derived as;

Compressional: $\boldsymbol{C_{33} = \rho V_{33}^2}$ **Equation 30**

Fast-shear: $\boldsymbol{C_{44} = \rho V_{32}^2}$ **Equation 31**

Fast-shear: $\boldsymbol{C_{55} = \rho V_{31}^2}$ **Equation 32**

Tran et al (2007) determined, from a nanoindentation test of Woodford sample, a set of calibrated stiffness values:

Statistics	GPa	GPa	GPa	GPa	GPa
Average	22.56	7.87	15.58	5.59	8.96
Standard deviation	4.07	0.71	0.60	0.60	0.71

Table 3-2. Stiffness values computed from the measurements for the five unknowns to characterize the horizontal transverse isotropic (Tran et al., 2007; Abousleiman, et al., 2010).

To compare this information from sonic dipole tools in drilled boreholes, tools can measure three of the five unknows, either for horizontal or vertical boreholes drilled. These component in borehole sonic are: C_{11}, C_{44} and C_{66}.

3.6 Results

I measured horizontal P-wave velocity and vertical P-wave velocity, perpendicular to the siliceous layers and perpendicular to the fractures. I also determined the horizontal S-wave and vertical S-wave velocity, perpendicular to the layering and perpendicular to the fractures. The P-wave velocity measured parallel to the bitumen fracture as a function of the frequency is shown in Figure 3-13.

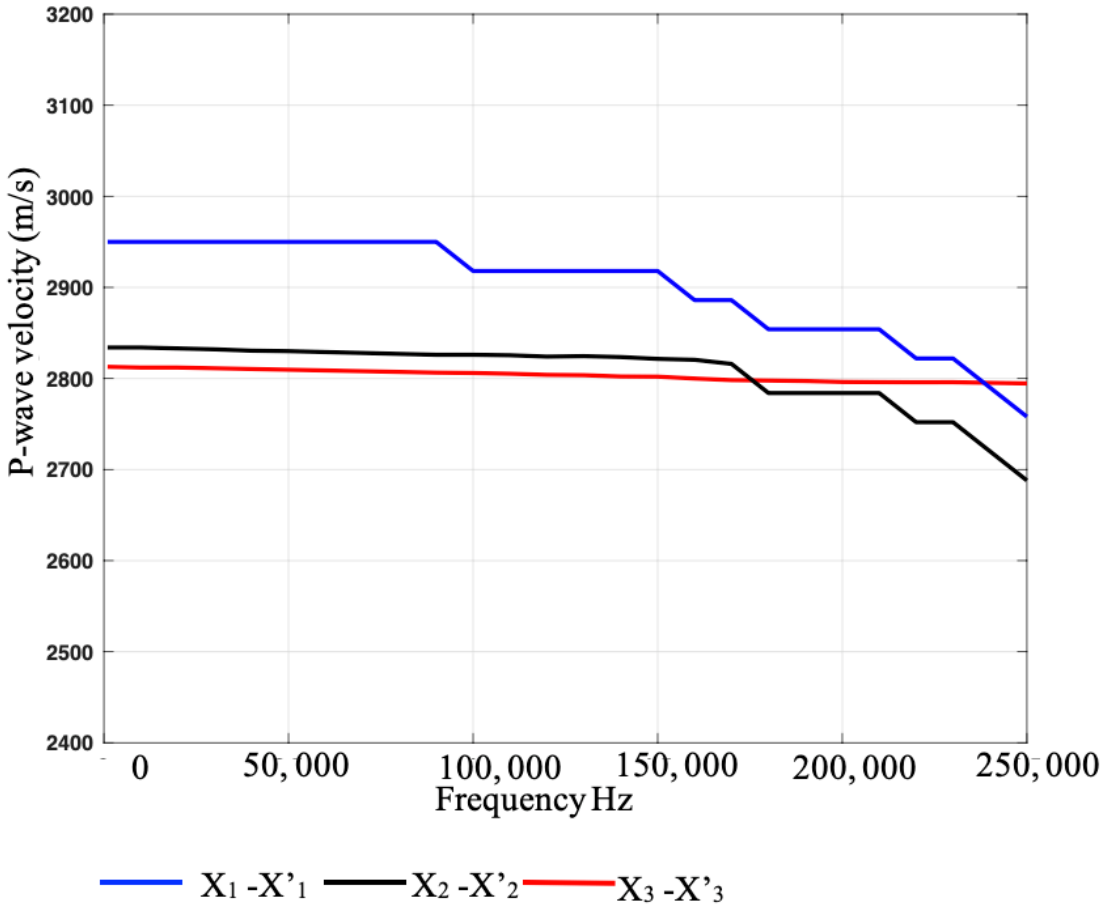

Figure 3-13. P-Wave velocity summary of a source activated on the X_2-X'_2 parallel to the fracture.

The analysis of the velocity profiles showed that the velocity decreases close to 6% in the X_1 direction with a steeper decent around 160,000 kHz. For the X_2 direction the velocity decreases 5%. These two measurements are made simultaneously but I plotted the P-wave velocity that was acquired in the X_3 direction from a different time. The velocity on the X_3 direction remains almost constant at 2820 m/s. Typically, velocity derived from high frequency measurements shows higher values in comparison to seismic velocities or borehole measurements. However, as samples are expensive to collect and preserve, and are carefully stored for different analysis. It is important to consider it was collected from an outcrop and measurements were made at ambient pressure and

room temperature. Shear velocities from a source activated parallel to the fracture shows a similar trend in the sense of recording lower velocities at high frequency than the values at low frequency, however. The absolute order of magnitude for each direction measured is different than in the P-wave experiment on Fig. 3-14. That is, on the P-wave monitoring of the fracture, the P velocity measured on the X_1-X'_1 direction is higher at lower frequencies and almost the same as the P-velocity to the X_3-X'_3 (vertical direction) at the higher frequency. The P-wave velocity measured at X_2-X'_2 at lower frequency is almost 50 m/s faster than the vertical velocity but 100 m/s slower at high frequency. On the S-wave velocity the S-wave measured on the X_2-X'_2 is faster both at low frequencies than at high frequency. Followed in order of magnitude by the X_1-X'_1 S-wave profile that is 50 m/s faster than the X_3-X'_3 direction.

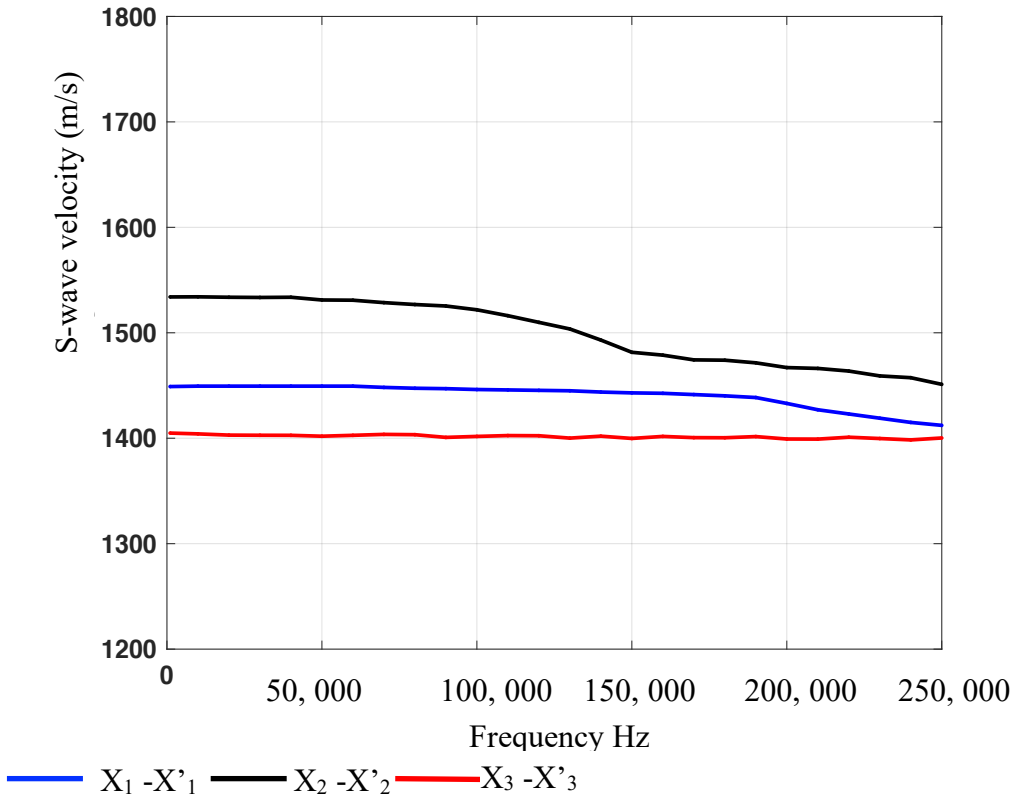

Figure 3-14. S-wave velocity profile as a function of frequency for X_1-X'_1, X_2-X'_2 and X_3-X'_3 direction.

On the other hand, from a source activated in the X_1-X'_1 direction, that is, perpendicular to the bitumen-filled fracture, the P-wave measurements exhibited a larger change 17 % in the X_2-X'_2 direction, and 11% on the X_1-X'_1 direction. Which is two times larger than a source activated on the X_2-X'_2. As in the source parallel to the bitumen fractures, the velocities profiles on the perpendicular case, showed a more rapid change after 160,000 kHz. For example, a P-wave velocity excited at 160, 000 kHz has a wavelength of 17.5 millimeters and a resolution of 4.15 millimeters. For a source of 250,000 kHz the wavelength is 11 millimeters and a detectability of 2.75 millimeters, which is close to the bitumen factures. The compressional velocity profiles of the acquisition perpendicular are summarized on the Figure 3-15, and S-wave profiles are shown in the Figure 3-16.

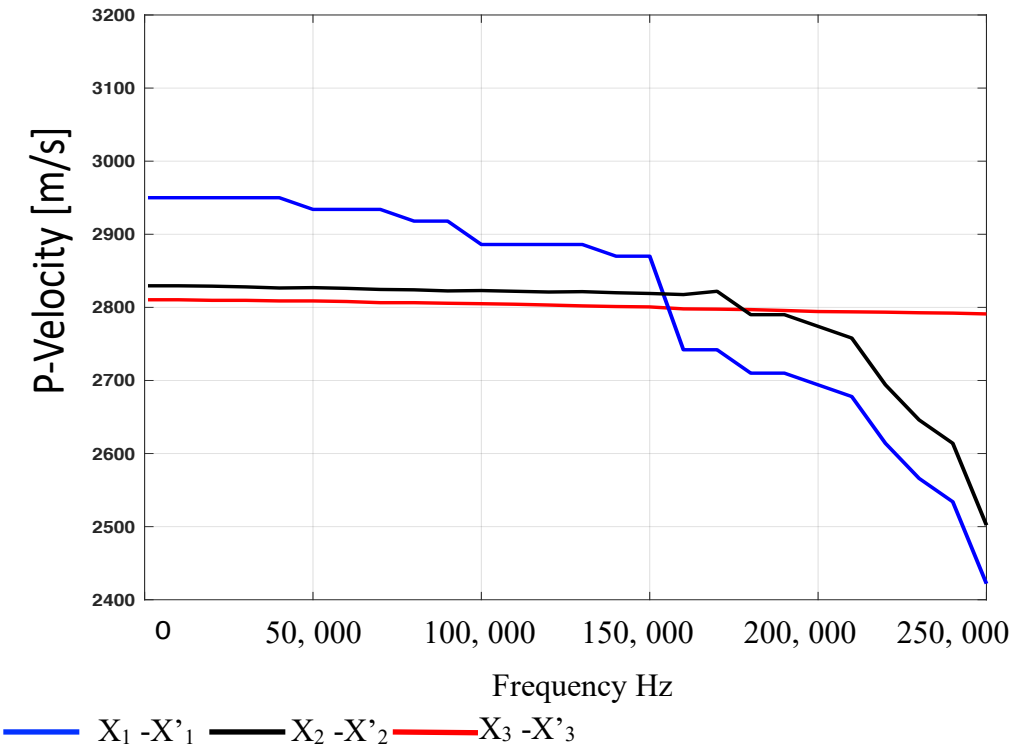

Figure 3-15. P-Wave profiles on different direction on the rock sample acquired as a function of frequency when the source is activated on the X_2-X'_2.

The 15 % difference on the P-wave velocities is shown on the X1-X1'direction on Figure 3-16. The drop of velocity goes from 2900 m/s to 2400 m/s. The velocity changed with a small gradient from 10 kHz to 150 kHz, at 160 kHz the velocity difference is close to 200 m/s. This reduction of velocity could suggest a reduction of elastic moduli as a function of frequency (either Young's or shear modulus) given that there is no loss of material or, that the waveform couples within the fracture. The order of magnitude in Figure 3-16 is the following, X_1-X'_1 had the highest velocity at low frequencies and the lower velocity at highest frequencies. 170 m/s slower, the X_2-X'_2 has a velocity of 2835 m/s at low frequency (50 kHz) and 2500 m/s at high frequencies (200 kHz), that represents 15% velocity change.

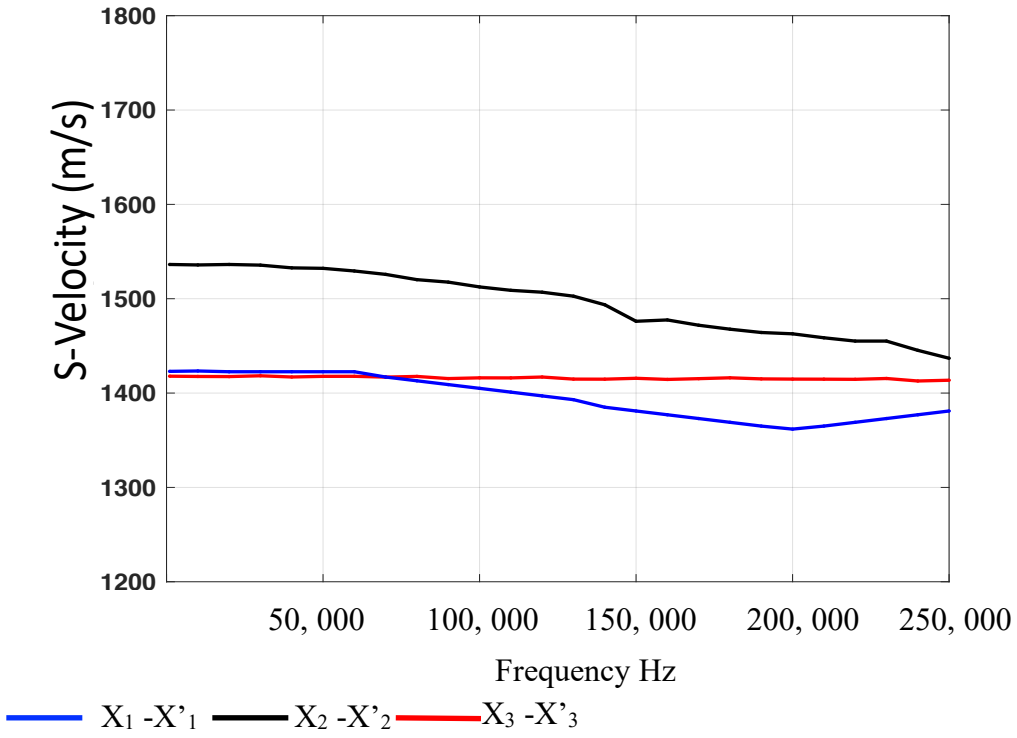

Figure 3-16. S-Wave profiles as a function of frequency for a source activated on the X_1-X'_1 direction, that is perpendicular to the filled fracture.

The vertical velocity, which was recorded and acquired vertically exhibits no change in the velocity as function of the frequency. The S-wave profiles on the Figure 3-14 the X_1-X'_1 and vertical measurements (X_3-X'_3) are closer at low frequency and exhibited a larger difference at 200 kHz. The percentage change between these two profiles was close to 3.5 % for the X_2-X'_2 and 0.4 % for the X_3-X'_3. The X_2-X'_2 shear velocity has a reduction of 7.3%. Since shear velocity is a function of shear modulus and density as:

$$\boldsymbol{S-Wave = \sqrt{\frac{G}{\rho}}} \qquad \textbf{Equation 33}$$

G is the shear modulus and density of the rock is represented by ρ.

I compared the elastic moduli based upon the percentage of S-wave anisotropy, defined by (Cheng & Toksoz, 1981) as:

$$\boldsymbol{\frac{V_{sh}-V_{sv}}{V_{sv}} x100} \qquad \textbf{Equation 34}$$

At high frequencies, the elastic-stiffening effect is exaggerated for both bulk and shear moduli, hence, the density effect is neglected. At 200, 000 Hz the wavelengths measured are close to 7 millimeters, which divided by four would have a resolution of 1.75 mm.

3.7 Hydraulic fracture simulation

A well stimulation is made to increase initial well productivity and in the long term to increase reserves, either by bypassing the damage zone, connecting more reservoir area to the boreholes or creating permeability pathways for the hydrocarbon fluids escape the isolated porosity systems. Ideally the fracture grows only in the zone of interest and will have a constant height and defined geometry (Figure 3-17). Well stimulation has multiple advantages, but it is expensive, time intensive and resource demanding. That is, several fit-to purpose pumps,

manifolds, and sand mixers are used and thousands of liters of waters to create specific fluid mixes tailored for each formation depending on the lithology and the objectives.

Given the resources used it is necessary to select the candidates to frack based on economic evaluation by determining the most feasible candidates by selecting the higher revenue with the lower investment (NPV).

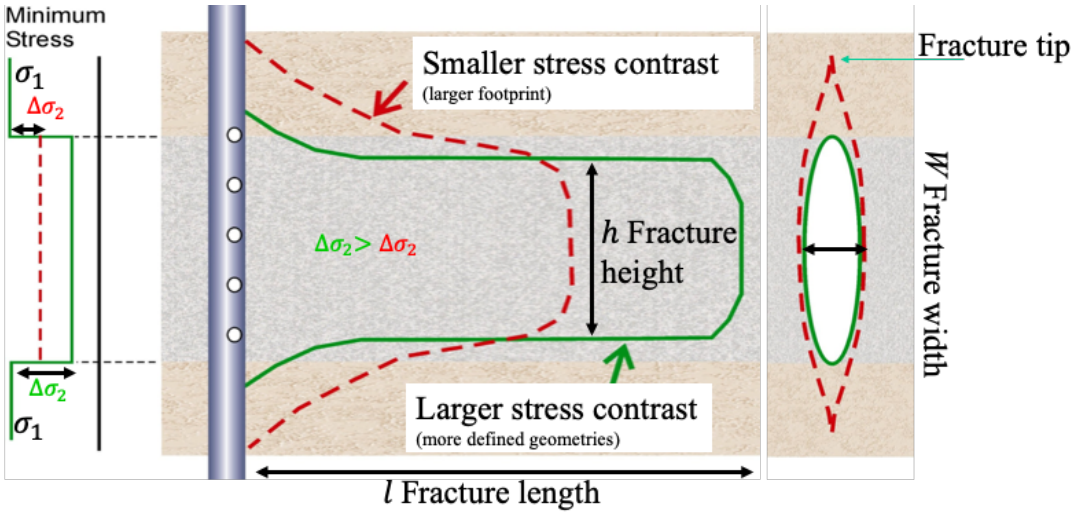

Figure 3-17. Conceptual model and important terms of a hydraulic fracture (image modified from (J. Guo et al., 2016).

The hydraulic fracture pressure/time analysis is one of the most adequate techniques to have an estimation of the minimum horizontal stress (Sessty & Ghassemi, 2016). As a summary, an hydraulic fracture will have different stages of interaction with the formation, changing the fluids during the HF and the pressure (Figure 3-17) the stages of an hydraulic fracture are: First, the pre-pad stage, where the fluid pressure is built up and is used to cool the formation and calibrate the fluid chemical composition. The pad stage where the fracture initiates and propagates, in this stage the minimum horizontal stress is reached and surpassed. Slurry stage it is a turbulent flow injects and transports the proppant. Finally, the flush: Displace slurry out of the surface equipment.

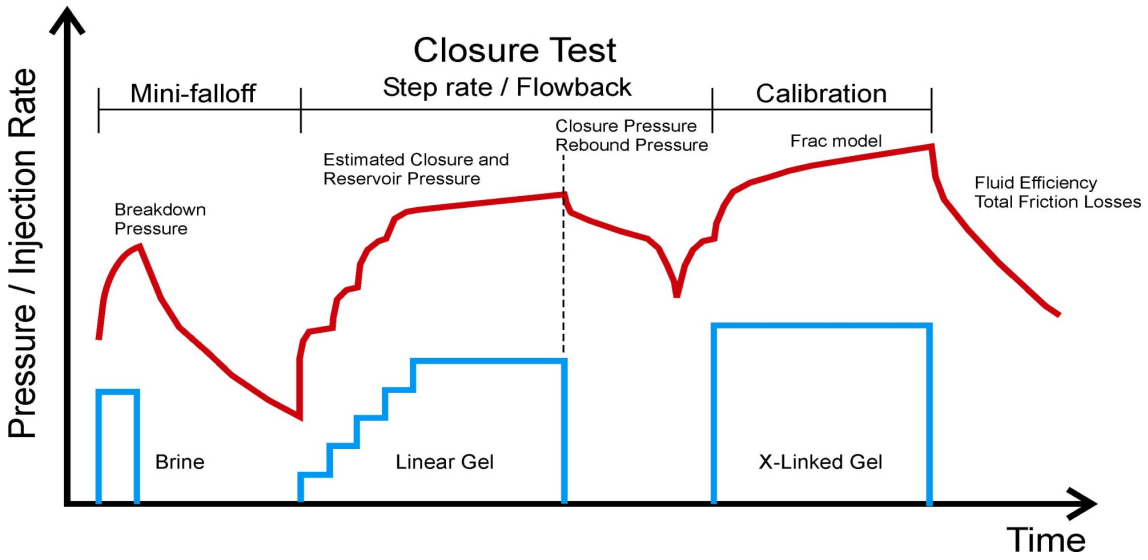

Figure 3-18. Conceptual Data Frack of a hydraulic fracture job. Derived from (Meng & De Pater, 2010)

In-situ stress is the single most important factor controlling HF, since it affects; fracture orientation, height (h), fracture width (w), proppant crushing and from tortuosity. Studying the anisotropy of a common reservoir rock in Oklahoma at the outcrop scale helps in estimating, stresses, rock properties (Young's modulus, Poisson's ratio, permeability, fracture toughness), and other reservoir properties.

I modeled the stress distribution during the pad stage, where the instantaneous shut in pressure represents the minimum horizontal stress at reservoir conditions. The numerical simulation is based on a two-dimensional model (2D), that represents the Woodford shale reservoir at 2900 meters depth for the two different directions (X_1-X'_1 and X_2-X'_2). The summary of the assumptions made in the model for the two different direction are in the Table 3-1. To calculate the minimum horizontal stress, I used the poro- elastic equations:

$$\sigma_h = \frac{v}{1-v}\sigma_v + \alpha\frac{1-2v}{1-v}P_p \qquad \textbf{Equation 35}$$

Where *v* is the Poisson ratio, a is the Biot's coefficient of effective stress (Biot, 1941; Kumpel,1991; Englender & Fischer, 1994), and P_p represents the pore pressure.

Properties	Parallel X_2—X'_2	Perpendicular X_1—X'_1
Regional Stress Azimuth	N85˚E	N85˚E
Density	2.4 $^{gr}/_{cm^3}$	2.4 $^{gr}/_{cm^3}$
Shear Modulus	0.31	0.29
Young's Modulus	9510 MPa	8700 MPa
Poisson Ratio	0.31	0.29
Depth/ Overburden	2900 m	2900 m

Table 3-1. Mechanical properties used as assumptions for the numerical simulation.

Since overburden and pore pressure is assumed constant, a normalized minimum horizontal stress after resolving the equations from Plumb (1994) presented as:

$$\boldsymbol{\sigma_{h\ in\ x2}} = \frac{\boldsymbol{v_{x2}}}{\boldsymbol{1-v_{x2}}} + \boldsymbol{\alpha}\frac{\boldsymbol{1-2v_{x2}}}{\boldsymbol{1-v_{x2}}} = 0.45 \qquad \textbf{Equation 36}$$

$$\boldsymbol{\sigma_{h\ in\ x1}} = \frac{\boldsymbol{v_{x1}}}{\boldsymbol{1-v_{x1}}} + \boldsymbol{\alpha}\frac{\boldsymbol{1-2v_{x1}}}{\boldsymbol{1-v_{x1}}} = 0.40 \qquad \textbf{Equation 37}$$

It is noteworthy that the normalized horizontal stress is unitless and helps to calculate the minimum horizontal stress at any given depth and compare the stress propagation.

Finite element models are employed to evaluate the stress distribution and help to understand the sensibility of hydraulic fracturing in a different direction in the Woodford Shale reservoir rock. I used a computational procedure to analyze the stress distribution using the finite element method (ABAQUS software) with 1000 elements. The result of the simulation for a frack

job parallel to bitumen-filled fractures is presented in two different times in Figure 3-19. I show the stress distribution in the X_1-X_1' direction on the Figure 3-20.

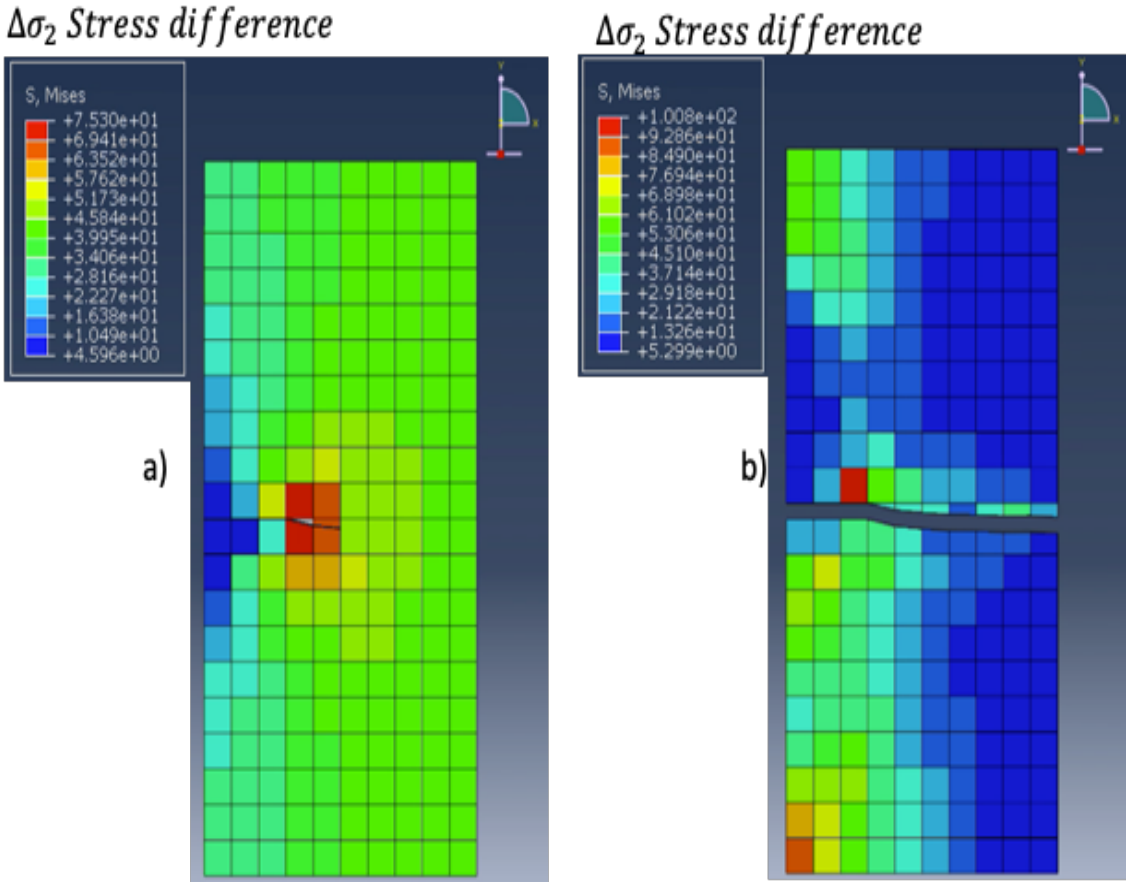

Figure 3-19. Stress concentration on the X_2-X'_2 direction. A) Initial stage of the fracture propagation, the fracture initiates at a stress difference 75 PSI. B) shows the fracture on a late time stage (3 min) with a maximum horizontal stress difference of 100 PSI.

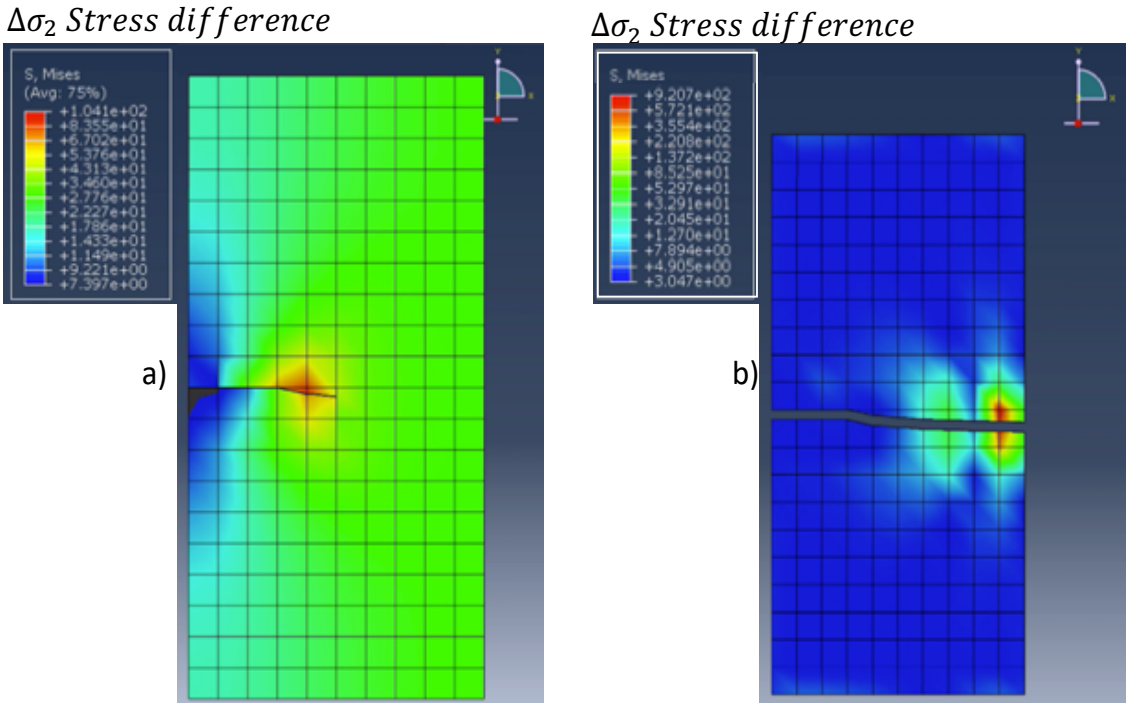

Figure 3-20 Stress concentration on the X_1-X'_1 direction A) Early stage of the fracture propagation, the fracture initiates at a stress difference 100 PSI. B) Later time step with a 900 PSI difference.

3.8 Anisotropy versus Scattering discussion

The mineral grains are randomly spread in the rock sample, generating various grain contacts (Moore & Wade, 2013), the problem of wave scattering by grains is not completely solved (Carcione et al., 2013). Only the particles smaller than the wavelength of the radiation and the spherically symmetrical particles of arbitrary radius can increase the probability of scattering. Anisotropy, is the concept that velocity may depend on the direction in which is recorded (Helbig & Thomsen, 2005). In this experiment, the fractured quasi-layered rock presents both effects in the measurements, impacting the velocity and increasing the uncertainty. An HTI model is insufficient to characterize completely the wave propagation but offers a close approximation.

a) b)

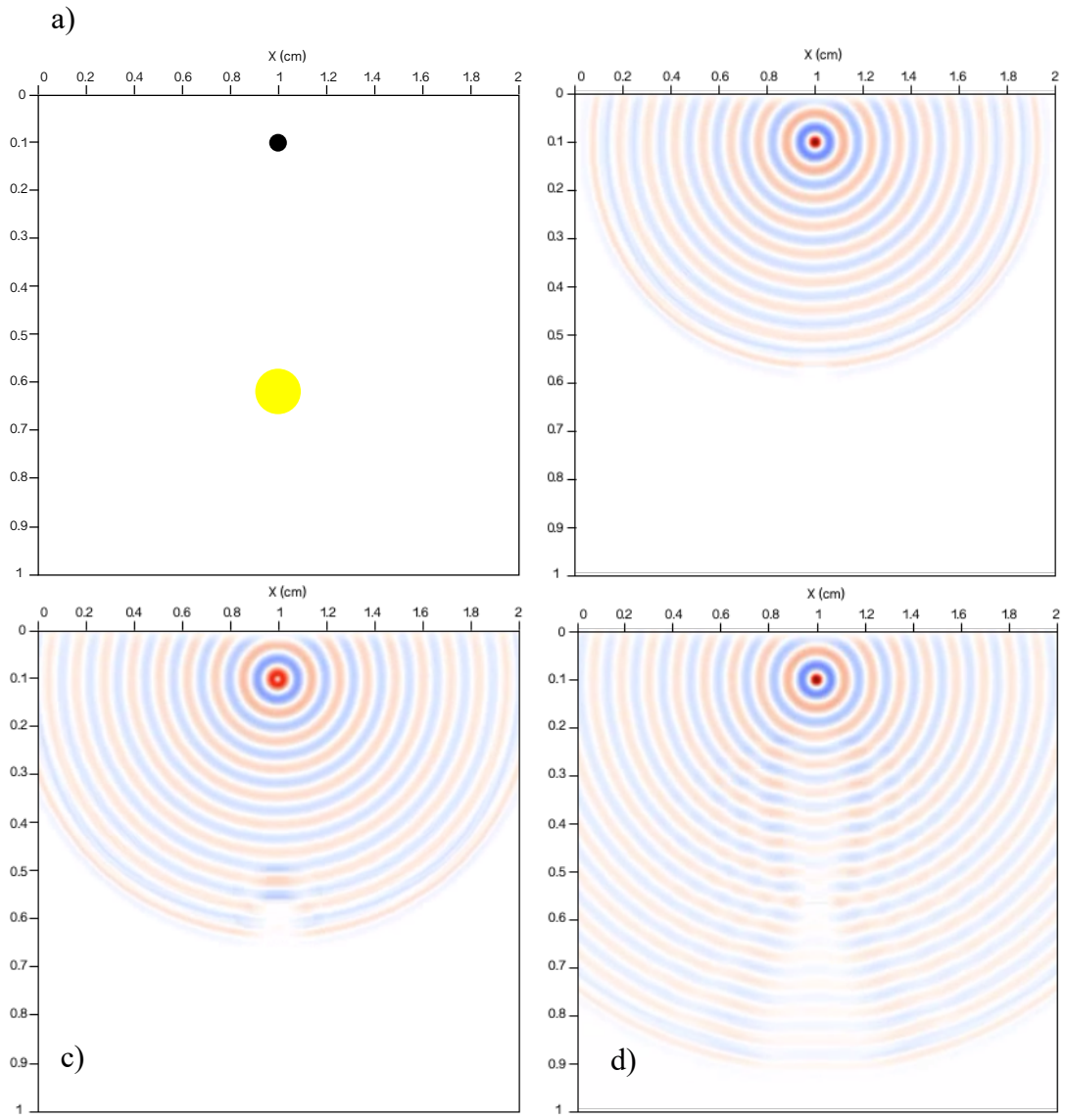

Figure 3-21. Scattering effect after an incident plane wave a) Initial model of a numerical simulation in Madagascar with a Gaussian velocity anomaly of shape (1/r) faster than the background b) wave propagation on the isotropic media c) Wavefront impact the velocity anomaly d) wavefront shape is affected, amplitude decrease and wavefront becomes flat.

In this model I showed the difference of scattering, where the velocity is affected by heterogeneities, but the direction of the measurements also changes, as wavelength reduces, the wavefront is more affected by heterogeneities. Since the trend of the velocity changes is different,

and the velocity measurements values at each frequency is different I conclude the most important observation is the anisotropy screening.

3.9 Interpretation and discussion

Undoubtedly outcrop studies have helped to understand the properties of similar subsurface formations better. Rock samples collected from the outcrops have a bias to be aware of, the most competent rock is typically collected. Different mechanical properties create a difference in velocity as a function of bitumen filled fracture. This difference can be explained by the fracture diagenesis followed by bitumen percolation due to tectonic stresses and hydrocarbon migration processes. These processes altered the initial state of the rock ordering the mechanical properties of the rock, and the heterogeneities were exacerbated when the formation was exhumated, and the overburden stress was removed. The rock sample and outcrop analyses it is observed that thinner mudrock presents a higher vertical intensity of fractures, while thicker mudrock has a lower vertical intensity fracture.

The clayrock on the other hand, the rock that deposited between the mudrock does not exhibit any vertical fractures but depicts highly papery bedding. The difference in the deformation mechanism also accounts for the difference in stress propagation. While the fractures are only generated in a more brittle material, the stress is distributed along the horizontal planes of the layers in the clayrock, serving as damping mechanism (attenuator).

The difference in P and S wave velocities at a higher frequency from a cored rock samples presents contrasting behavior compared to other studies. In this study, in general, the velocity measured in the vertical axis of the rock sample shows no significative difference. However, on the X_2-X'_2 and X_1-X'_1 there is a reduction in P-wave and S-wave velocity as a function of

frequency. The velocity reduction is more significant (5% versus 17%) at higher frequencies (250 kHz), and its trend changes rapidly from 150 kHz to 250 kHz. The most crucial velocity difference is observed in the acquisition perpendicular to the bitumen filled fracture. This difference for the P-wave can be explained as the wave energy that has to be transmitted through the organic matter, which is more ductile when the wavelength is small enough to be close to the filled fractures. At the same time, S-wave energy is more rapidly scattered and thus is the S-wave velocity.

Modeling the difference of elastic parameters in a different direction using an isotropic propagation mechanism is just a rough method to showcase the difference in the stress propagation due to elastic parameters in different directions. Setting the horizontal minimum stress aside. Fracking parallel to a fracture would create a fracture with a smaller stress difference, while fracking perpendicular to a bitumen fracture initiates the fracture at 100 PSI, the stress difference is only 25 %.

After the fracture, the fluid flow pressure (without any proppant) would create a different stress concentration in the two cases. On the X_1-X'_1, the stress concentration would be concentrated at the tip of the fracture turning towards the far-field maximum horizontal stress. while on the X_2-X'_2 direction it would be more scattered and in general concentrated near-wellbore. The resolution of the model prevents me from observing the fracture tip splitting into multiple segments.

The stress difference is similar in magnitude to that of Adachi (2009). This study modeled a fracture height growth with parameters shown in Table 4-1, the stress differences as a function of time in Figure 3- 21.

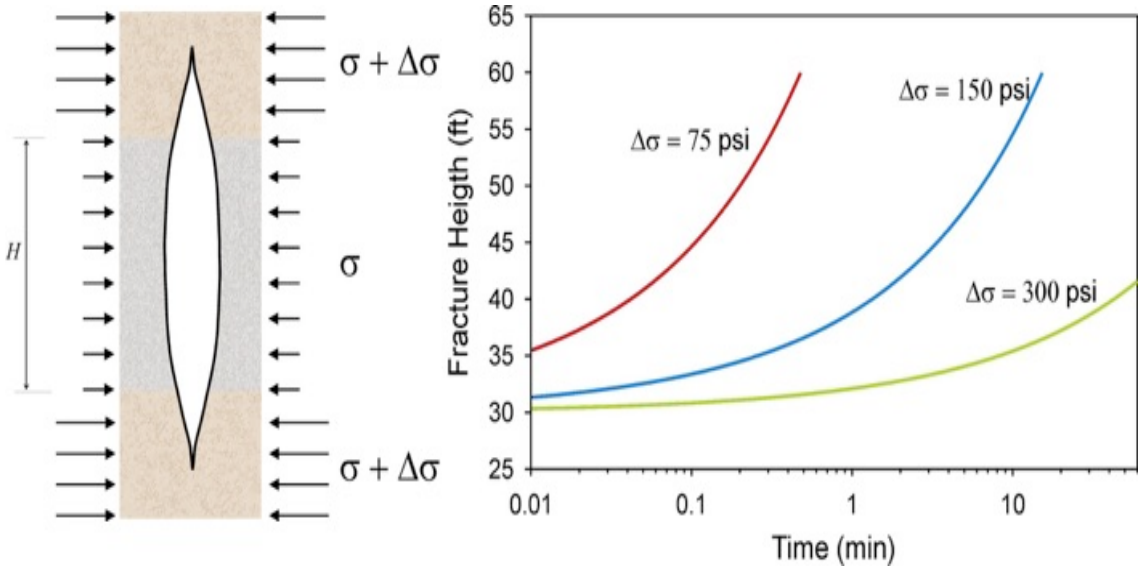

Figure 3-22 Example of fracture height growth of stress contrast on a pseudo 3D modeling on an isotropic case.

Parameter	Data
Initial fracture height	30 ft
Flow rate	15 bpm
Young Modulus	145 kPSI
Poisson ratio	0.2
Fluid viscosity	100 cp

Table 4-1. Mechanical parameters used in Adachi J, 2009.

In this study I used a frequency range of 10 kHz to 250 kHz versus Hoffman (2015), where he observed a different behavior on shales (higher velocity at higher frequency), he studied with a constant sampling rate a range from 3 Hz to 8000 Hz, and one sample from 8 kHz to 800 kHz. The rock sample he used was rich in organic matter and highly laminated but not fractured. Also, these samples were from a borehole core.

To confirm this particular behavior further constraints are needed, for example, measuring the velocity under confining stress. Also, it would be important to model the anisotropy in the 1D wave propagation, to cast doubt on the effect of anisotropy on stress shadow. However, both of these tasks are beyond the scope of this thesis at this point.

It is essential to generate mechanical models from outcrop samples for its correlation with buried formations to gain an understanding in the critical trends. From a Woodford shale outcrop, the ultrasonic measurements show different velocities as a function of the fracture direction and the presence of bitumen. Adding different methodologies to understand brittleness and its heterogeneities helps to derive information on hydrocarbon termination techniques. Multiscale integration that is studying the rock sample at different resolution scales assists the monitoring of mechanical properties of reservoir rocks and its complex relationship with in-situ stresses. Numerical modeling techniques used to visualize a geological challenge has proved to be a valuable tool to understand its performance.

As context, Mexico has just entered exploration-production in non-conventional reservoirs. In Mexico, hydraulic fracturing techniques has been employed in tight sands (low permeability) in the north of Mexico (Burgos Basins and Chicoantepec basins) (Perez-Cruz, 1993). However, hydraulic fracturing jobs have not escalated to the massive scale it has in the USA, in specific in shale reservoirs. In order, to provide further insight to the complexities of producing from shale reservoirs, outcrops studies provide an excellent source of rock samples, where abundant techniques can be applied to link outcrop rock samples to analogous formation in the subsurface. In order to assist anisotropy screening I propose the implementation of this technique to rocks collected to monitor the anisotropy impact on hydraulic fracturing. This could impact the resource

budgeting, reduce production cost and, increment profitability. The results of this work are associated with a 3-5 % uncertainty for P-wave, that is, on measuring the travel time first arrivals, the values from one position varied between 3 to 5 %. For S-wave velocities the uncertainty was larger, changes differ from 5-15% between measurements. Principal source of errors in the velocity readings come from sensors disconnecting from the rock samples. The second error specially detected at low frequencies comes from the corner frequency of the sensors, which has a preferred frequency from 20kHz to 500kHz, but it has a more stable behavior from 50 kHz.

Chapter 4 Discussion and Conclusions

4.1 Discussion

Incorporating different aspects of the hydrocarbon industry cycle can expand our understanding of the mechanical properties that control production in oil and gas reservoirs. Mechanical properties in the subsurface control the fractures in a naturally fractured reservoir. Also, they play an essential role in controlling the permeability genesis in sandstone reservoirs or diagenetically altered carbonate reservoirs. Also, incorporating drilling and engineering parameters helps to understand the stress state in the formations of interest better. The in-situ earth stress model can be better characterized as more information is included. Especially in mature oil provinces where thousands of mechanical tests (hydraulic fractures) takes place daily. To properly estimate the pore-pressure regime in the Ceja survey I would need other sources of information, from P-velocity used for time or depth migration to update reservoir production pressure profiles or MDT. The pore pressure would be one of the factors that most impacts the BI as it impacts the effective stress.

Further research would be needed to measure the P- velocity of different types of rock from the outcrop, to calibrate the anisotropy measurements with other properties, such as organic richness or chemical content. Also needed, are the inclusion of anisotropy models for fracture propagation and visual inspection of fracture growth and stress contrasts.

4.2 Conclusions

The integrated approach to determine the Brittleness Index in this work makes it feasible to discern the impact of pre-existing basement structures and paleo-deposition environments on

the interplay between sequence stratigraphy and mechanical properties. The BI attribute shows that high values correlate with higher hydrocarbon production and are not completely associated with the structural highs, but with the sedimentary deposition features. For example, high prospective areas are located on the structural flanks, corresponding to brecciated fluxes that had different diagenesis than the open water carbonates.

In the Mississippi Lime, the hydrocarbon production is in part controlled by the mechanical properties. A less brittle inter-sequence seal would have a lower Poisson's ratio, a lower Young's modulus and a lower BI value of (0.1-0.4). Those values correlate with dry intervals and smaller gas production due to the lack of connectivity of isolated porosity patches. Moreover, the rate of penetration (ROP) in the Mississippi Lime, in the chert facies, which is a lithological unit in the Mississippi Lime, is higher than in the argillaceous limestone. The contrasting ROP could have several origins, and I interpret it as higher rock fragility that breaks with more ease thanks to the higher porosity and the stiffer matrix of the chert (Qi X. et al. 2018).

Drilling and completions engineers could potentially benefit from understanding the fragility of the formation of interest. The mechanical facies classification can assist in driving appraisal campaigns; water injection wells spacing, and better evaluations of the frackability of the formation of interest. To evaluate the formation frackability potential of one of the most critical hydrocarbons plays in the USA and ergo in the world (The Woodford shale) I measured the difference in P- and S-wave velocities over a large frequency range from a cored rock sample from a representative outcrop. The velocity measured on the vertical axis of the rock sample shows no significative difference. However, in the X_2-X_2' and X_1-X_1'there is a reduction in P-wave and S-wave velocity as a function of frequency. The velocity reduction observed in the profiles is more

significant (5 % versus 17%) at higher frequencies (250 kHz). This difference suggests a frequency dependence in the elastic moduli.

The P-wave difference and velocity reduction could potentially suggest that the wave energy that has to be transmitted through the organic matter, which is less brittle, is more attenuated when the wavelength is small enough to detect the filled fractures. Less brittle formations would represent the need to have had a more significant stress contrast to propagate the fracture. However, the vertical discontinuities, represent a weak plane that would break before the stress is transmitted perpendicular to the strata. In this thesis, the S-wave velocity profiles generated from S-wave sensors show that the waveform energy is more rapidly scattered in the fractures and and results in a velocity.

Modeling the difference of elastic parameters in a different direction using an isotropic propagation mechanism is just a rough method to showcase the difference in the stress propagation due to elastic parameters in different directions. Fracking parallel to a fracture would create a fracture with a smaller stress difference, while fracking perpendicular to a bitumen fracture initiates the fracture at a 25% stress difference. After the fracture is created, the fluid flow pressure (without any proppant) would create a different stress concentration in the two cases. In the X_1-X_1', the stress concentration concentrates at the tip of the fracture turning towards the far-field maximum horizontal stress. While in the X_2-X'_2 direction it would be more scattered and in general concentrated near-wellbore. The resolution of the model prevents observation of fracture tip splitting into multiple segments.

From this thesis, I showed the value of data integration for mature fields to discern productive units and the relationship with productivity index. Brittleness Index presents a sound

explanation on why boreholes with more than 200,000 BPD coexist within 500 meters of boreholes that have produced less than 2,000 BPD drilled in the same time interval from the same operator. Another output from my thesis is a to have a high-resolution velocity model to correlate with the regional velocity model of Oklahoma. I presented the fault mapping of the area and deep basement faults that are connected to shallower strata. The fault architecture could help to expand the analyses on faults nucleation, since the fault model on the depth domain.

From the analysis on the anisotropy of the Woodford shale, I concluded that fracturing perpendicular to the fracture would require a 25% larger stress difference. Also, I showed how a fracture parallel to the bitumen fractures is faster and that both directions have a different mechanical distribution of the stress field.

References

Abdulraheem, A., Roegiers, J.-C., & Zaman, M. (1992). Mechanics of pore collapse and compaction in weak porous rocks. *The 33th U.S. Symposium on Rock Mechanics (USRMS)*, p. 10. Retrieved from https://doi.org/

Abousleiman, Y. (University of O., Tran, Minh, (University of Oklahoma), & Hoang, S. (University of O. (2010). Geomechanics field characteization of Woodford shale and barnett shale with advanced logging tools and nano-indentation on drill cuttings. *The Leading Edge*, *Borehole g*(June), 730–736.

Aisenberg, M. (2013). The value of processing legacy data_A acase study of bois d'arc, a Mississippi play in Northeastern Oklahoma (Oklahoma). Retrieved from http://mcee.ou.edu/aaspi/upload/AASPI_Theses/2013_AASPI_Theses/Aisenberg_MS_Thesis.pdf

Aktepe, S., Marfurt, K. J. ., & Altamar, R. P. (2008). Attribute expression of basement faulting —. *The Leading Edge*. https://doi.org/10.1190/1.2896627

Algeo, T. J., & Tribovillard, N. (2009). Environmental analysis of paleoceanographic systems based on molybdenum-uranium covariation. *Chemical Geology*, *268*(3–4), 211–225. https://doi.org/10.1016/j.chemgeo.2009.09.001

Alrefaee, H., Keller, G. R., & Marfurt, K. J. (2012). Integrated Geophysical Studies on the Basement Structure of the Arkoma Basin , Oklahoma and Arkansas. *AAPG Search and Discovery*, *50710*.

Alt II, R. (Stanford), & Zoback, M. (Stanford). (2015). In-situ stress and active faulting in Oklahoma. *AAPGE*, *2*(1), 1–48.

Alt, R. C., & Zoback, M. D. (2017). In situ stress and active faulting in Oklahoma. *Bulletin of the Seismological Society of America*, *107*(1), 216–228. https://doi.org/10.1785/0120160156

Avset, Per, Mukerji Tapan, Mavko, G. (Stanford). (2005). *Quantitative Seismic Interpretation*.

Bass, N. (1940). Subsurface Geology and Oil and Gas Resources of Osage County, Oklahoma. *Summary of Subsurface Geology with Special Reference to Oil and Gas*, *111*(111), 380–382. Retrieved from https://pubs.usgs.gov/bul/0869/report.pdf

Bass, N. W., Dillard, W. R., & Kennedy, L. E. (1941). Subsurface geology and oil and gas resources of Osage County, Oklahoma. *Department of The Interior*, *900*(1), 319.

Becerra, Daniela, M. (Oklahoma U. (2017). *Daniela Becerra MS Thesis*. Oklahoma University.

Bernal, A. S. (2013). *Geological Characterization of the Woodford Shale, McAlister Cemetery Quarry, Criner Hills, Ardmore Basin, Oklahoma*. Retrieved from https://books.google.com/books?id=x7u6ngEACAAJ

Biot, M. A. (1941). General Theory of Three-Dimensional Consolidation. *Journal of Applied Physics*, *12*(2), 155–164. https://doi.org/10.1063/1.1712886

Bjørlykke, K., Jahren, J., Mondol, N. H., Marcussen, O., Croize, D., Peltonen, C., & Thyberg, B. (2008). Sediment Compaction and Rock Properties. *AAPG International Conference and Exhibition*, *50192*, 1–8.

Bowers, G. (1995). Pore Pressure Estimation From Velocity Data: Accounting for Overpressure Mechanisms Besides Undercompaction. *SPE Drilling & Completion*, *10*(02), 89–95. https://doi.org/10.2118/27488-PA

Bowers, G. (2001). *Determining an Appropriate Pore-Pressure Estimation Strategy*. https://doi.org/10.4043/13042-MS

Boyd, D. (2002). *Map of Oklahoma O&G production: reservoir age* (p. 1). p. 1.

Branson, C, (OGS). (1958). *Fifty years progress semi-centennial report -of the director to the governor of the state of Oklahoma*.

Carcione, J. M., Gurevich, B., Santos, J. E., & Picotti, S. (2013). Angular and Frequency-Dependent Wave Velocity and Attenuation in Fractured Porous Media. *Pure and Applied Geophysics*, *170*(11), 1673–1683. https://doi.org/10.1007/s00024-012-0636-8

Chen, X., Nakata, N., Pennington, C., Haffener, J., Chang, J. C., He, X., … Walter, J. I. (2017). *The Pawnee earthquake as a result of the interplay among injection , faults and foreshocks*. (May), 1–18. https://doi.org/10.1038/s41598-017-04992-z

Chopra, S., & Marfurt, K. (2014). *Seismic Attribute Expression of Differential Compaction *. 41265*.

Corp., P. R. O., Sea, N., River, P., & River, P. (2018). Petro River Oil Discovers North Blackland Field in Osage County , Ok. *Glob Energy*, pp. 17–20.

DeGarmo, C., Nguygen, T., & Philp, R. P. (2016). A new look at the organic geochemical variability in the Woodford Shale of the Ardmore Basin: paleoweathering and organic matter source. *Search and Discovery*, *41799*(41799), 28pp.

Denison, R. (1981). *Basament rocks in northeastern Ok* (first edit; Oklahoma geological survey, Ed.).

Denison, R. E. (1966). *Basement Rocks in Adjoining Parts of Oklahoma, Kansas, Missouri, and*

Arkansas.

Dicman, A., & Vernik, L. (2012). A New Petrophysical Model for Organic Shales. *Spwla*, *54*(3), 1–15.

Dowdell, B. L., Kwiatkowski, J. T., & Marfurt, K. J. (2013). Special section : Interpretation for unconventional resources Seismic characterization of a Mississippi Lime resource play in Osage County , Oklahoma , USA. *Interpretation*, *1*(2), 97–108.

Dowdell, B. L., Roy, A., & Marfurt, K. J. (2012). An integrated study of a Mississippian tripolitic chert reservoir – Osage County, Oklahoma, USA. In *SEG Technical Program Expanded Abstracts 2012* (pp. 1–5). https://doi.org/10.1190/segam2012-1563.1

Dutta, N. C. (1983). Shale compaction and abnormal pore-pressures: A model of geopressures in the Gulf Coast basin. In *SEG Technical Program Expanded Abstracts 1983* (pp. 542–544). https://doi.org/10.1190/1.1893736

Dutta, N. C. (2003). Geopressure prediction using seismic data: Current status and the road ahead. *Geophysics*, *67*(6), 2012–2041. https://doi.org/10.1190/1.1527101

Dutta, T. (Stanford). (2009). *Integrating Sequence stratigraphy and Rock-physics to interpret seismic amplitudes and predict reservoir quality*.

Dvorking, J. (Deparment of G. U., & Nur, A. (D. of G. / S. U.). (2000). *Cricial porosity models*. Stanfrod Ca.

Eaton, B. A. (1975). The Equation for Geopressure Prediction from Well Logs. *Fall Meeting of the Society of Petroleum Engineers of AIME*, p. 11. https://doi.org/10.2118/5544-MS

Edwards, S. T., Bratton, T. R., & Standifird, W. B. (2002). Accidental Geomechanics - Capturing In-situ Stress from Mud Losses Encountered while Drilling. *SPE/ISRM Rock Mechanics Conference*, p. 14. https://doi.org/10.2118/78205-MS

Ekwunife, Ifunaya, C. (2017). Assessing mudrock characteristics, high resolution chemostratigraphy, and sequence stratigraphy of the woodford shale in the Mcalister cemetery quarry, Ardmore basin, Oklahoma.

Elebiju, O. O., Matson, S., Keller, G. R., Marfurt, K. J., & Group, S. E. (2011). Integrated Geophysical Studies of the Basement Structures , the Mississippi Chert , and the Arbuckle Group of Osage County Region , Oklahoma. *AAPG*.

Elebiju, O. O., Matson, S., Randy Keller, G., & Marfurt, K. J. (2011). Integrated geophysical studies of the basement structures, the Mississippi chert, and the Arbuckle Group of Osage County region, Oklahoma. *AAPG Bulletin*, *95*(3), 371–393. https://doi.org/10.1306/08241009154

Englender, T. (Pennsylvania S. U., & Fischer, Mark, (Pennsylvania State University). (1994). Influence of poroelasticity behavior on the magnitude of minimum horizontal stress, Sh, in overpressured parts of sedimentary basins. *Geology*, Vol. 22, pp. 949–952.

Evans, S., & Suneson, N. (2016). Bibliography of Osage County Geology. *Oklahoma Geological Survey*, *1*(August), 10.

Feinstein, S. (1981). Subsidence and Thermal History of Southern Oklahoma Aulacogen: Implications for Petroleum Exploration. *AAPG Bulletin*, *65*, 2521–2533. https://doi.org/10.1306/03B599F9-16D1-11D7-8645000102C1865D

Ferron, D. (Chevron), & Smiley, B. (Chevron). (2014). *Revised 2014 / DSG Drilling Specialties Company a division of Chevron Phillips Chemical Company LP Main Office : 832-813-1866 Customer Service : 800-423-3985 Technical Service : 800-221-1956*.

Fjær, E., Holt, R., Horsrud, P., M. Raaen, A., & Risnes, R. (1992). Petroleum Related Rock Mechanics. In *Developments in Petroleum Sience* (Vol. 33).

Galvis, H., Becerra, D., & Slatt, R. (2018). *Special section : Characterization of the Woodford Shale : Latest concepts and techniques Lithofacies and stratigraphy of a complete Woodford Shale outcrop section in South Central Oklahoma : Geologic considerations for the evaluation of unconventional sh*. *6*(1). https://doi.org/10.1190/INT-2017-0074.1

Gardner, G. H. F., Gardner, L. W., & Gregory, A. R. (1974). Formation Velocity and Density—the Diagnostic Basics for Stratigraphic Traps. *Geophysics*, *39*(6), 770–780. https://doi.org/10.1190/1.1440465

Gersztenkorn, A., & Marfurt, K. J. (1999). Eigenstructure-based coherence computations as an aid to 3-{D} structural and stratigraphic mapping. *Geophysics*, *64*(5), 1468–1479.

Gholami, R., Moradzadeh, A., Rasouli, V., & Hanachi, J. (2014). Practical application of failure criteria in determining safe mud weight windows in drilling operations. *Journal of Rock Mechanics and Geotechnical Engineering*, *6*(1), 13–25. https://doi.org/https://doi.org/10.1016/j.jrmge.2013.11.002

Ghosh, S. (2017). *Integrated studies on Woodford Shale natural fracture attributes, origin, and their relation to hydraulic fracturing*. https://doi.org/10.13140/RG.2.2.15739.82722

Goebel, T. H. W., Weingarten, M., Chen, X., Haffener, J., & Brodsky, E. E. (2017). The 2016 Mw5 . 1 Fairview , Oklahoma earthquakes : Evidence for long-range poroelastic triggering at > 40 km from fluid disposal wells. *Earth and Planetary Science Letters*, *472*, 50–61. https://doi.org/10.1016/j.epsl.2017.05.011

Goldstein, R., & King, B. (2014). History of Hydrothermal Fluid Flow in the Midcontinent: A Key to Understanding the Origin and Distribution of Porosity*. *AAPG Search and*

Discovery, *50958*(50958), 34. Retrieved from http://www.searchanddiscovery.com/pdfz/documents/2014/50958goldstein/ndx_goldstein.pdf.html

Goodfellow, S. D., Tisato, N., Ghofranitabari, M., Nasseri, M. H. B., & Young, R. P. (2015). Attenuation Properties of Fontainebleau Sandstone During True-Triaxial Deformation using Active and Passive Ultrasonics. *Rock Mechanics and Rock Engineering*, *48*(6), 2551–2566. https://doi.org/10.1007/s00603-015-0833-8

Guo, J. C., Luo, B., Zhu, H. Y., Yuan, S. H., Deng, Y., Duan, Y. J., … Chen, L. (2016). Multilayer stress field interference in sandstone and mudstone thin interbed reservoir. *Journal of Geophysics and Engineering*, *13*(5), 775–785. https://doi.org/10.1088/1742-2132/13/5/775

Guo, Z., Li, X., Liu, C., Feng, X., & Shen, Y. (2013). *A shale rock physics model for analysis of brittleness index , mineralogy and porosity in the Barnett Shale*. https://doi.org/10.1088/1742-2132/10/2/025006

Gupta, I. N. (1973). Seismic velocities in rock subjected to axial loading up to shear fracture. *Journal of Geophysical Research*, *78*(29), 6936–6942. https://doi.org/10.1029/jb078i029p06936

Hale, D. (2013). Methods to compute fault images, extract fault surfaces, and estimate fault throws from 3D seismic images. *Geophysics*, *78*(2), O33–O43. https://doi.org/10.1190/geo2012-0331.1

Harris, N. B. (2015). Shale velocity and density as functions of TOC and thermal maturity: Upper Devonian Woodford Shale, Permian Basin, Texas. *Search and Discovery*, *51124*(51124), 1–27.

Helbig, K., & Thomsen, L. (2005). 75th Anniversary Paper - 75-plus years of anisotropy in exploration and reservoir seismics: A historical review of concepts and methods. *Geophysics*, *70*(6), 9ND-23ND. Retrieved from http://library.seg.org/doi/10.1190/1.2122407%0Apapers3://publication/doi/10.1190/1.2122407

Higley, D. K. (2013). 4D petroleum system model of the Mississippian System in the Anadarko Basin Province, Oklahoma, Kansas, Texas, and Colorado, U.S.A. *Mountain Geologist*, *50*(3), 81–98. Retrieved from http://pubs.er.usgs.gov/publication/70192034

J., E. K., Cheng, C. H., & Toksoz, M. N. E. R. L. (1981). *Estimating a shear modulus of transversely isotropic formation*.

Jannane, M., Beydoun, W., Crase, E., Cao, D., Koren, Z., Landa, E., … Xie, M. (1989). Wavelengths of earth structures that can be resolved from seismic reflection data.

Geophysics, *54*(7), 906–910. https://doi.org/10.1190/1.1442719

Jansen, D. P., Carlson, S. R., Young, R. P., & Hutchins, D. A. (1993). Ultrasonic imaging and acoustic emission monitoring of thermally induced microcracks in Lac du Bonnet granite. *Journal of Geophysical Research: Solid Earth*, *98*(B12), 22231–22243. https://doi.org/10.1029/93jb01816

Keller, G. R., & Stephenson, R. A. (2007). The Southern Oklahoma and Dniepr-Donets aulacogens: A comparative analysis. In *Memoir of the eological Socity of America* (Vol. 200, pp. 127–143). https://doi.org/10.1130/2007.1200(08)

Kerimov, A. (Colorado S. of M. (2013). *Middle Bakken wettability evaluation using NMR T2 Forward modeling and mineralogy*.

Khatiwada, M., Keller, G. R., & Marfurt, K. J. (2013). A window into the Proterozoic: Integrating 3D seismic, gravity, and magnetic data to image subbasement structures in the southeast Fort Worth basin. *Interpretation*, *1*(2), T125–T141. https://doi.org/10.1190/int-2013-0041.1

Kirkland D.W., D. R. E. S. D. M. (1992). Geology and organic geochemistry of the Woodford Shale in the Criner Hills and western Arbuckle Mountains, Oklahoma, in K.S. Johnson and B.J. *OGS Circular*, *93*, 65–78.

Li, C., Liu, D., Cai, Y., & Yao, Y. (2016). Fracture permeability evaluation of a coal reservoir using geophysical logging: A case study in the Zhengzhuang area, southern Qinshui Basin. *Energy Exploration and Exploitation*, *34*(3), 378–399. https://doi.org/10.1177/0144598716631664

Liner, K. M. (University of A. (2015). *An Investigation of 3D Seismic Deep Basement Events in Osage County , Oklahoma*.

Lo, T., Coyner, K. B., & Toksöz, M. N. (1986). Experimental determination of elastic anisotropy of Berea sandstone, Chicopee shale, and Chelmsford granite. *Geophysics*, *51*(1), 164–171. https://doi.org/10.1190/1.1442029

Looms, M. C., Jensen, K. H., Binley, A., & Nielsen, L. (2008). Monitoring Unsaturated Flow and Transport Using Cross-Borehole Geophysical Methods. *Vadose Zone Journal*, *7*(1), 227. https://doi.org/10.2136/vzj2006.0129

Marfurt, K. J. (2006). Robust estimates of 3D reflector dip and azimuth. *Geophysics*, *71*(4), P29–P40. https://doi.org/10.1190/1.2213049

Marfurt, K. J. (2014). Seismic attributes and the road ahead. *Geophysical Society of Houston*, *2*(September), 11–15. https://doi.org/10.1190/segam2014-1644.1

Marfurt, K. J., Kirlin, R. L., Farmer, S. L., & Bahorich, M. S. (1998). 3-D seismic attributes using a semblance-based coherency algorithm. *Geophysics*, *63*(4), 1150–1165. https://doi.org/10.1190/1.1444415

Marsh, S., & Holland, A. (2016). Comprehensive Fault Database and Interpretive Fault Map of Oklahoma. *Oklahoma Geological Survey Open File Report OF2-2016*, *OF2-2016*.

Mavko, G., Mukerji, T., & Dvorkin, J. (2009). *The Rock Physics Handbook: Tools for Seismic Analysis of Porous Media*. Retrieved from https://books.google.com/books?id=bcx-KTvpptMC

McCullough, B. J., & Slatt, R. M. (2014). Stratigraphic variability of the Woodford Shale across Oklahoma. *Search and Discovery*, *80417*(80417), 24pp.

McKnight, E, T., & Fischer, R, P. (1970). Geology and Ore Deposits of the Picher Field Oklahoma and Kansas Geology and Ore Deposits of the Picher Field Oklahoma and Kansas. *United States Geological Survey Professional Papper*, *588*(580), 1–148.

Meng, C., & J. De Pater, H. (2010). Hydraulic Fracture Propagation in Pre-Fractured Natural Rocks. *44th US Rock Mechanics Symposium - 5th US/Canada Rock Mechanics Symposium*. https://doi.org/10.2118/140429-MS

Milad, B., Ghosh, S., & Slatt, R. M. (2018). Comparison of rock and natural fracture attributes in karsted and non-karsted Hunton Group Limestone: Ada and Fittstown area, Oklahoma. *Shale Shaker*, *69*(2), 70–86.

Moore, C., & Wade, W. (2013). Carbonate Reservoirs: Porosity and Diagenesis in a sequence stratigraphy framework. In *Elsevier science & Technology* (1st ed., Vol. 67). https://doi.org/10.1017/9781316341285.001

Murray, Kyle, (Oklahoma Geological Survey), & Holland, Austin, (Oklahoma Geological Survey). (2014). Structural Analysis of the Boktukola Syncline , Central Ouachita Mountains , Oklahoma ; Inventory of Class II Underground Injection Control Volumes in the Mid-Continent ; Inventory of Class II Underground Injection Control Volumes in the Midcontinent. *The Journal of the Oklahoma City Geological Society*, *65*(2), 98–106.

Nakata, N., & Snieder, R. (2011). Near-surface weakening in Japan after the 2011 Tohoku-Oki earthquake. *Geophysical Research Letters*, *38*(17), 1–5. https://doi.org/10.1029/2011GL048800

Nelson, K. D., Lillie, R. J., de Voogd, B., Brewer, J. A., Oliver, J. E., Kaufman, S., … Viele, G. W. (1982). Cocorp seismic reflection profiling in the Ouachita Mountains of western Arkansas: Geometry and geologic interpretation. *Tectonics*, *1*(5), 413–430. https://doi.org/10.1029/TC001i005p00413

Nolan, Thomas, B. (USGS). (1963). Geological survey research 1963. *USGS*, *2*(2), 194. https://doi.org/10.1016/0022-1694(64)90031-9

Nur, A. (1987). Seismic rock properties for reservoir descriptions and monitoring. In G. Nolet (Ed.), *Seismic Tomography: With Applications in Global Seismology and Exploration Geophysics* (pp. 203–237). https://doi.org/10.1007/978-94-009-3899-1_9

Nur, Amos, & Simmons, G. (1969). Stress-induced velocity anisotropy in rock: An experimental study. *Journal of Geophysical Research*, *74*(27), 6667–6674. https://doi.org/10.1029/jb074i027p06667

Pan, B. Z., Yuan, M. X., Fang, C. H., Liu, W. Bin, Guo, Y. H., & Zhang, L. H. (2017). Experiments on acoustic measurement of fractured rocks and application of acoustic logging data to evaluation of fractures. *Petroleum Science*, *14*(3), 520–528. https://doi.org/10.1007/s12182-017-0173-2

Petersen, M., S. Mueller, C., Moschetti, M., M. Hoover, S., L. Llenos, A., L. Ellsworth, W., … S. Rukstales, K. (2016). Seismic-Hazard Forecast for 2016 Including Induced and Natural Earthquakes in the Central and Eastern United States. *Seismological Research Letters*, *87*, 1327–1341. https://doi.org/10.1785/0220160072

Pigott, John, D., & Abouelresh, M. (2016). Basin deconstruction–construction: Seeking thermal–tectonic consistency through the integration of geochemical thermal indicators and seismic fault mechanical stratigraphy–Example from Faras Field, North Western Desert, Egypt. In *Journal of African earth sciences* (Vol. 114).

Plumb, R. (1994). Influence of composition and texture on the failure properties of clastic rocks, in Rock Mechanics in Petroleum Engineering. *Proceedings SPE/ISRM International Conference, Delft, Netherlands,* (August).

Plumb, R. A. (2002). Variation of the least horizontal stress magnitude in sedimentary rocks, in rock mechanics and measurments challenges from industry. In *Rock Mechanics Models and Measurements Challenges from Industry* (pp. 71–81).

Plumb, R., Edwards, S., Pidcock, G., Lee, D., & Stacey, B. (2000). The Mechanical Earth Model Concept and Its Application to High-Risk Well Construction Projects. *IADC/SPE Drilling Conference*, p. 13. https://doi.org/10.2118/59128-MS

Posamentier, H. W., & Allen, G. P. (1999). Siliciclastic Sequence Stratigraphy: Concepts and Applications. *SEPM (Society for Sedimentary Geology)*, *7*. https://doi.org/https://doi.org/10.2110/csp.99.07

Puckette, J., & Al-Shaieb, Z. (2008). Sequence stratigraphy, lithofacies, and reservoir quiality upper morrow sandstones northwestern shelf. In *Oklahoma Geological Survey*: *Vol. Circular 1* (pp. 39–47).

Qi, X. (MCEE/ O. U. (2018). Seismic attributes assisted quantitative unconventional reservoir characterization (Vol. 1). https://doi.org/10.22201/fq.18708404e.2004.3.66178

Reeves, T. K., Banerjee, S., & Contract, U. (1999). *An explration 3D seimic field test program in OSAGE county, Oklahoma.* Tulsa,Okllahoma.

Romo, D. (2015). The cantarell oil field and the mexican economy. *Problems in Oil Apprisal*, *46*(183), 1–21.

Roy, A., Dowdell, B., & Marfurt, K. (2013). Characterizing a Mississippian tripolitic chert reservoir using 3D unsupervised and supervised multiattribute seismic facies analysis: An example from Osage County,. *Interpretation for Unconventional Resources*, *1*(2), 109–124. https://doi.org/10.1190/segam2012-1365.1

Santamarina, C., Macdougall, C., & Roy, V. (1992). Tomographic Imaging Stress Changes in Soil Media. *Transportation Research Record*, *1415*(2), 95–99.

Sayers, C. M. (2010). *Geophysics Under Stress : Geomechanical Applications of Seismic and Borehole Acoustic Waves* (First edit; S. of E. G. (SEG) & (EAGE). European Association of Geoscientist and Engineers, Eds.). Tulsa.

Sayers, C. M. (2013a). Introduction: Rock Physics for Reservoir Exploration, Characterisation and Monitoring. *Geophysical Prospecting*, *61*(2), 251–253. https://doi.org/10.1111/1365-2478.12034

Sayers, C. M. (2013b). The effect of kerogen on the AVO response of organic-rich shales. *The Leading Edge*, *December*, 1514–1519.

Sayers, C. M., & den Boer, L. D. (2018). The Elastic Properties of Clay in Shales. *Journal of Geophysical Research: Solid Earth*, *123*(7), 5965–5974. https://doi.org/10.1029/2018JB015600

Scott, T. E., Abousleiman, Y., & Zaman, M. (2001). *Acoustical Imaging and Mechanical Properties of Soft Rock and Marine Sediments (Quarterly Technical Progress Report # 15302R04)*.

Scott, T., Ma, Q., Roegiers, J.-C., & Reches, Z. (1994). Dynamic stress mapping utilizing ultrasonic tomography. *1st North American Rock Mechanics Symposium*, (1990).

Sebaa, N., Sebaa, N., Fellah, Z. E. a, Fellah, Z. E. a, Fellah, M., Fellah, M., … Lauriks, W. (2006). Ultrasonic characterization of human cancellous bone using the Biot theory: inverse problem. In *The Journal of the Acoustical Society of America* (Vol. 120). https://doi.org/10.1137/1.9780898717921

Sessty, V. (Reservoir G. and S. G. U., & Ghassemi, A. (Reservoir G. and S. G. U. (2016).

Numerical Modeling of Hydraulic Fracture Propagation From Horizontal Wells in Anisotropic Shale. *ARMA*, *52*(10), 1–15.

Shepherd, M. Depositional Environments and their Flow Charateris. , Oil Field Production Geology 253 (2009).

Simm, R. (2007). Practical Gassmann fluid substitition in sand/shale sequences. *First Break*, *25*(December), 61–68.

Slatt, Roger, M. (University of O., & Abousleiman, Y. (University of O. (2011). Merging sequence stratigraphy and geomechanics for unconventional gas shales. *The Leading Edge*, *Shales*(March), 274–282.

Slatt, R. (University of O. (2013). *Stratigraphic Reservoir Characterization for Petroleum Geologists , Geophysicists , and* (Second edi; Elsevier, Ed.). Elsevier.

Slatt, R. M., Galvis-Portillo, H., Becerra-Rondon, D., Ekwunife, I. C., Brito, R., Zhang, J., … Milad, B. (2018). Outcrop and subsurface geology applied to drilling, sweet spot and target zone detection of resource shales: the Woodford example. *Unconventional Resources*, *URTEC*(Figure 1), 1–17. https://doi.org/10.15530/urtec-2018-2893838

Slatt, R. M., Molinares, C., Amorocho, J. D., Cabarcas, C., & Torres-Parada, E. (2014). Sequence Stratigraphy, Geomechanics, Microseismicity, and Geochemistry Relationships in Unconventional Resource Shales. *Search and Discovery*, *80407*(80407). https://doi.org/10.15530/urtec-2014-1934195

Slatt, R. M., & Rodriguez, N. D. (2012). Comparative sequence stratigraphy and organic geochemistry of gas shales: Commonality or coincidence? *Journal of Natural Gas Science and Engineering*, *8*, 68–84. https://doi.org/https://doi.org/10.1016/j.jngse.2012.01.008

Sleep, N. H., & Nakata, N. (2017). Nonlinear attenuation of S waves by frictional failure at shallow depths. *Bulletin of the Seismological Society of America*, *107*(4), 1828–1848. https://doi.org/10.1785/0120160334

Sleep, N. H., & Nakata, N. (2018). Nonlinear Body Waves in the Shallow Subsurface , Implications of Flow-Law Rheologies. *11th U.S. National Conference on Earthquake Engineering*, *94025*. Los Angeles.

Sone, H. (Stanford). (2012). *Mechanical properties of shale gas reservoir rocks and its relation to the in-situ stress variation observed in shale gas reservoirs* (Vol. 128).

Sone, H., & Zoback, M. D. (2013). Mechanical properties of shale-gas reservoir rocks — Part 1: Static and dynamic elastic properties and anisotropy. *Geophysics*, *78*(5), 381–392. https://doi.org/10.1190/GEO2013-0050.1

Stein, S., Stein, C. A., Elling, R., Kley, J., Keller, G. R., Wysession, M., … Moucha, R. (2018). Insights from North America's failed Midcontinent Rift into the evolution of continental rifts and passive continental margins. *Tectonophysics*, *744*(March), 403–421. https://doi.org/10.1016/j.tecto.2018.07.021

Suneson, N. H. (2012). Arkoma Basin Petroleum Past , Present , and Future. *Oklahoma City Geological Socity*.

Suriamin, F., & Pranter, M. J. (2016). Integrating Standard Petrophysical Analysis with Statistical Measures of Petrophysical Heterogeneity to Estimate Petrofacies in Mississippian Limestone, North-Central Oklahoma*. *AAPG Search and Discovery*, *41767*, 1–3. Retrieved from http://www.searchanddiscovery.com/documents/2016/41767suriamin/ndx_suriamin.pdf

Tisato, N., & Madonna, C. (2012). Attenuation at low seismic frequencies in partially saturated rocks: Measurements and description of a new apparatus. *Journal of Applied Geophysics*, *86*, 44–53. https://doi.org/10.1016/j.jappgeo.2012.07.008

Tran, minh hue, N. Abousleiman, Y., K. Hoang, S., J. Ortega, A., Bobko, C., & Ulm, F. (2007). The Acoustic Signature of Woodford Shale and Upscale Relationship from Nano-Scale Mechanical Properties and Mineralogy. *AGU Fall Meeting Abstracts*.

Trumbo, D. B. (2014). *A production calibrated reservoir characterization of the Mississippi lime in a mature field utilizing reprocessed legacy 3D seismic data, kay county, Oklahoma* (Oklahoma University). Retrieved from http://mcee.ou.edu/aaspi/upload/AASPI_Theses/2014_AASPI_Theses/Trumbo_MS.pdf

Tsvankin, I. (2013). Seismic Signatures and Analysis of Reflection Data in Anisotropic Media, Third Edition. In *Seismic Signatures and Analysis of Reflection Data in Anisotropic Media, Third Edition* (third edit). https://doi.org/10.1190/1.9781560803003

Vail, P. R., & Mitchum, R. M. (1977). Seismic stratigraphy and global changes of sea level, 1, Overview. *Memoirs of the American Association of Petroleum Geologists*, *22*(26), 51–52.

Vandervoort, C. (2011). Data & Drilling Methods from Horizontal Mississippian Reservoirs Across Northern Oklahoma. *Orion Exploration Partners*.

Vanorio, T., Scotellaro, C., & Mavko, G. (2008). The effect of chemical and physical processes on the acoustic properties of carbonate rocks. *The Leading Edge*, *27*(8), 1040–1048. https://doi.org/10.1190/1.2967558

Vernik, L., & Liu, X. (1997). Velocity anisotropy in shales: A petrophysical study. *Geophysics*, *62*(02), 521–532.

Vernik, L., & Liu, X. (2002). Velocity anisotropy in shales: A petrophysical study. *Geophysics*,

62(2), 521–532. https://doi.org/10.1190/1.1444162

Vernik, L., & MIlovac, J. (Marathon O. C. (2011). Rockphysics of organic shales. *The Leading Edge*, *Shales*(March), 318–323.

Vernik, L., & Zoback, M. D. (1992). Estimation of maximum horizontal principal stress magnitude from stress-induced well bore breakouts in the Cajon Pass Scientific Research borehole. *Journal of Geophysical Research: Solid Earth*, *97*(B4), 5109–5119. https://doi.org/10.1029/91JB01673

Wang, F. P., and J. F. W. G. (2009). Screening criteria for shale-gas systems. *Gulf Coast Association of Geological Societies Transactions*, *59*, 779–793.

West, A. (2015). *Pennsylvanian Subsurface Sequence Stratigraphy Based on 3D Seismic and Wireline Data in Western Osage County , Oklahoma*.

Williams, T. (2013). The Effectiveness of Oil and Gas Regulatory Oversight on Oil and Gas Operations Osage County , Oklahoma. *The Enviromentally Friendly Drillnig Program*, *2*(July), 1–68.

Wu, X., & Hale, D. (2016). *Technical papers t Automatically interpreting all faults , unconformities , and horizons from 3D seismic images*. *4*(2), 227–237.

Yilmaz, N. G., Karaca, Z., Goktan, R. M., & Akal, C. (2009). Relative brittleness characterization of some selected granitic building stones : Influence of mineral grain size. *Sciencedirect*, *23*(1), 370–375. https://doi.org/10.1016/j.conbuildmat.2007.11.014

Zhang, J., Scott, J., Slatt, R., & Turner, B. (2016). *Regional Fine-Scale Sequence Stratigraphy of the Woodford Shale and Its Impact on Microseismic Activity and Optimizing Future Hydraulic Fractures *. 51241*. https://doi.org/10.1190/1.3567258.

Zhao, L., Qin, X., Han, D., Geng, J., Yang, Z., & Cao, H. (2016). *Rock-physics modeling for the elastic properties of organic shale at different maturity stages Rock-physics modeling for the elastic properties of organic shale at different maturity stages*. (December 2017). https://doi.org/10.1190/geo2015-0713.1

Zoback, M. (Stanford). (2007). *Reservoir Geomechanics* (1st Editio; Cambridge, Ed.). Cambridge University Press.

Appendix A: Experiments to characterize velocity recovery in a porous limestone after a stress-perturbation

Stress field perturbations in rocks are common on multiple scales. The stress perturbation in many cases generates an elastic change, a quasi-dynamical mechanism that alters the internal structure for a determined period of time. If the stress-strain ratio is below elastic limit of the rock, the material relaxes back to its unperturbed state. The limits of the recovery are given by the elastic properties and confining conditions; at any given depth, the materials are naturally more resistant to deformation.

Rocks under stress exhibit a hysteresis behavior which explains components of the history of strain-stress. The stress-strain history alters the strain-stress ratio changing the rheological properties of different lithologies at different depth, i.e. higher confining pressure makes subsurface rock stiffer. This recovery can be measured by acquiring ultrasonic waveforms produced by and ultrasonic compressional source in a dry-laboratory sample. I apply coda wavefield interferometry on time windows to identify in different time windows the velocity changes due to an external perturbation an its posterior velocity recovery after a perturbation is removed.

The physics behind the nonlinear elasticity behavior ranging from hysteresis and memory to a transient response of elastic properties during stress field perturbations. This velocity reduction quasi-dynamically recover to the background values after the perturbation is removed as a logarithmic function over time. This physical phenomenon it is observed in most materials and on different scales. I applied coda wavefield interferometry as a tool to estimate elastic velocity changes due to external perturbations. In this work, applying coda wavefield interferometry to

ultrasonic waveforms recorded on the rock sample, I actively image the nonlinear velocity recovery after a mechanical perturbation to characterize the velocity recovery. Also, I measure the shear velocity to analyze to explore shear wave changes.

The experimental rock sample is a limestone block with eight to twelve sensors. The source had a frequency of 150 kHz, the sampling frequency was 10 MHz and the total recorded time was 0.15 ms. The sample was loaded in a uniaxial loading frame in the Rock Mechanics Laboratory at the University of Oklahoma. One of the experimental perturbations consisted on three different perturbation magnitudes, 400 N, 800 N. The second perturbation experiment consisted of a weight shock of 100 kg dropped from one meter to a contact metallic cylinder of 11 cm of radius.

I analyzed the acoustic events with seismic interferometry techniques. Velocity changes are affected due to ray path characteristics from the perturbation caused by the impact and the loading. For example, for an unperturbed imaging, the monitoring of the rock sample exhibits a constant velocity, that is, no change. However, the velocity changes and the recovery of velocity changes have a range of 1.2% (0.6 % decrease to 0.6% increase).

Acoustic monitoring of rocks is a powerful method to examine the behavior of materials deforming under stress. Stress perturbations that do not surpass the elastic limit generate a transient nonlinear elastic response that affects the wave propagation path, from the source to the receiver. Using ultrasonic active source waveforms, I monitor these velocity changes by estimating the cross-correlation time lag on the coda part of the waveforms. Velocity changes can be correlated to monitor pore fluid content (Nur, 1987) thermal fracturing (Jansen, Carlson, Young, & Hutchins, 1993), the intensity of stresses around the fracture (Santamarina et al., 1992).

Monitoring triaxial stress acoustic velocity changes as a function of triaxial stress is an activity well studied since the late 1960s (Amos Nur & Simmons, 1969; Gupta, 1973; Lo et al. 1986; Fjaer et al. 1989; Sayers et al. 1990; Scott et al. 1993), these experiments were done at laboratory scale. On regional scale (Maeda ,2010, Nakata 2011, Sleep, 2017) showed the temporal relationship of weakening due to water saturation levels and the velocity recovery with time.

The results from these studies show that a perturbation of the stress field creates a region of changes around the stress perturbation, even when the stress is below the elastic limit. Scott et al. (1994) documented the ultrasonic tomography of velocity distribution during the loading of a sandstone. The experiment documented the development of a high-velocity zone during application of indentation stress. The velocity results showed a monotonic relationship between regions with high stress and the observed velocity increase (Jannane et al., 1989; Young et al. 1992; T. Scott et al., 1994)

Methodology

The rock sample block is an Indiana limestone, that is a carbonate rock, a grainstone of a very uniform texture and grade. It was deposited from early Carboniferous. Its chemical composition is 97% calcium carbonate (Table A-1). It has a porosity that varies from two to twelve porosity percentage. Grainstone has an ultimate compressive strength of 2.75 x10^7 Pa (27.5 MPa). This sample is a freestone, which means that it has no preferential direction of splitting, making the sample highly versatile. Two samples from the same material were used for this experiment. The first sample was a prism sample with dimesons of 220 mm, 160 mm and 140 mm that was machined from a more massive block, and then each side was surface grounded using a

CNC surface grinder. The objective was to remove imperfection and obtain 5 μm flatness and to make the sample parallel (0.01 mm). With this sample I performed the three different acquisitions to observe the non-linear recovery after a stress perturbation using coda wavefield interferometry. From the block sample I generated three cores of 45 mm diameter and 90 mm length (maintaining the 1:2 ratio). I used these cores for ultrasonic experiments d) and e). All samples were oven-dried at 60°C during 24 h before each waveform acquisition, since carbonates are very susceptible to humidity and the experiments took place at room temperature and humidity.

I used an ultrasonic pulse generator and physical acoustic express receiver to excite a compressional source of nominal frequency of 150 kHz every 2-ms and record simultaneously eight different receivers. The waveforms recorded by different sensors. The Figure A-1-1 shows the workflow I used to monitor the limestone rock.

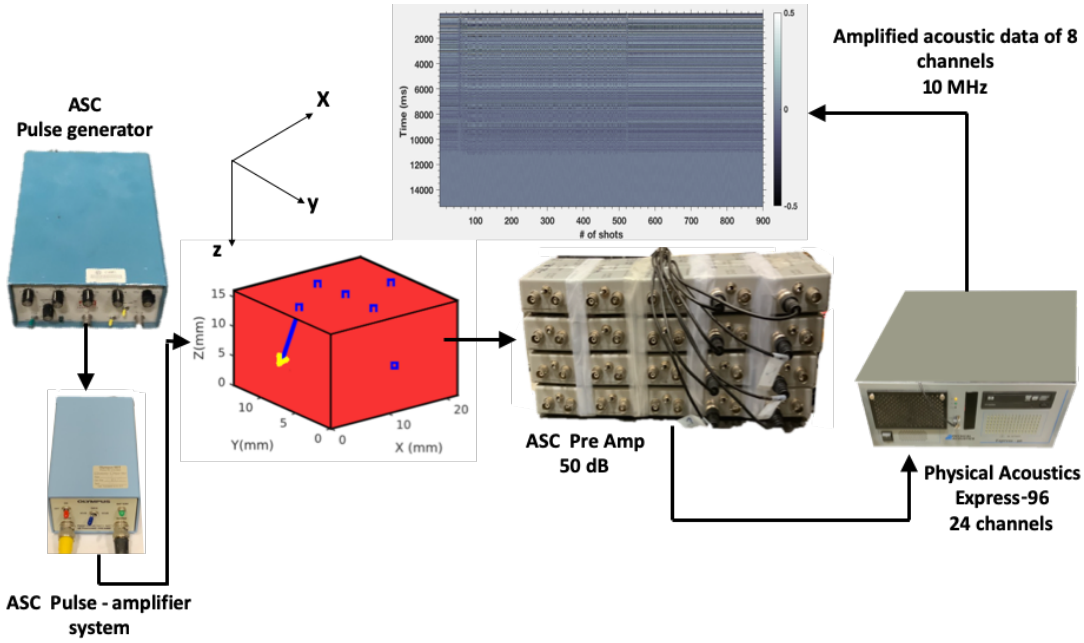

Figure A-1-1 Acquisition diagram for damage experiments -Source-Sample-Receivers-Recording system-waveforms.

On the cubic carbonate sample, I performed three different experiments with different sensor locations and explored different perturbation mechanisms. To monitor noise level background of the laboratory and confirm that the coda wavefield interferometry is measuring changes in the velocity I monitored a source activated every 2 ms with eight different sensors using the acquisition setup in (Figure A-1-2). The rock sample under different stress alteration I will present on the results section were using the sensor distribution on Figure A-1-3. The last results were more mechanical control was needed, I three cylinders from the rock sample. I performed a failure test on one of the cylinders.

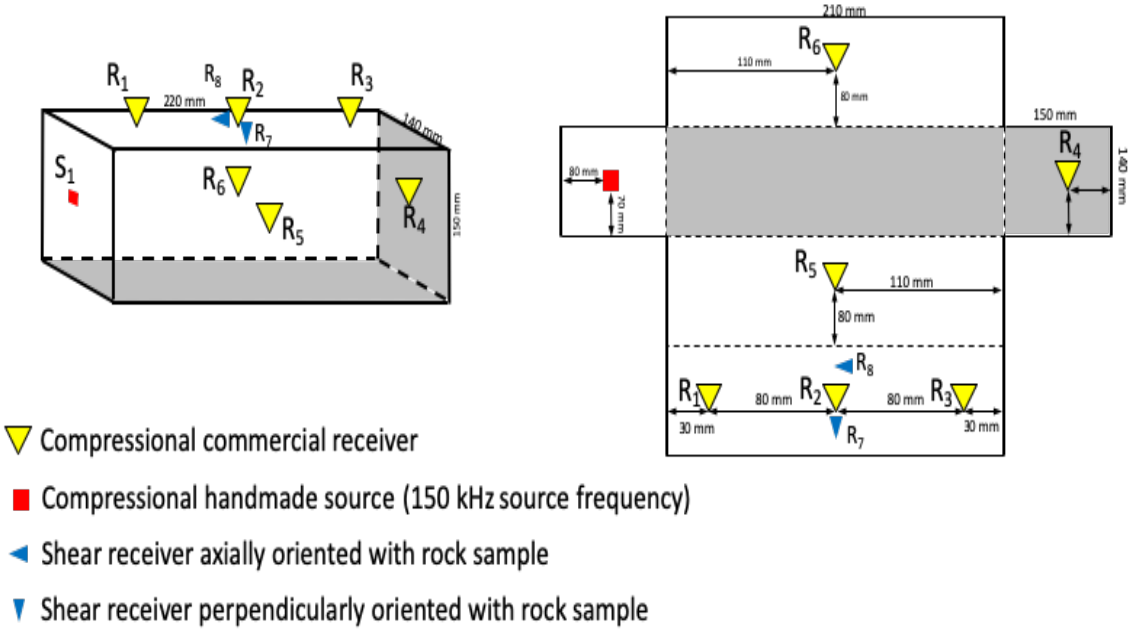

Figure A-1-2 Background monitoring and source and sensor location

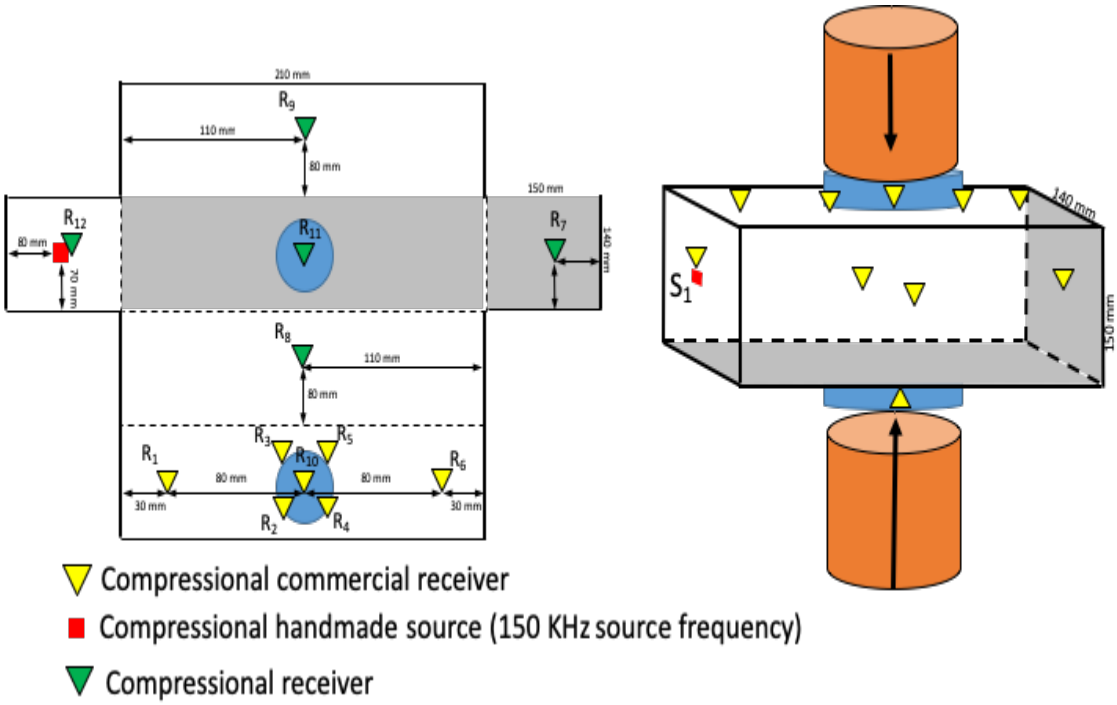

Figure A-1-3 Damage monitoring and source and sensor location

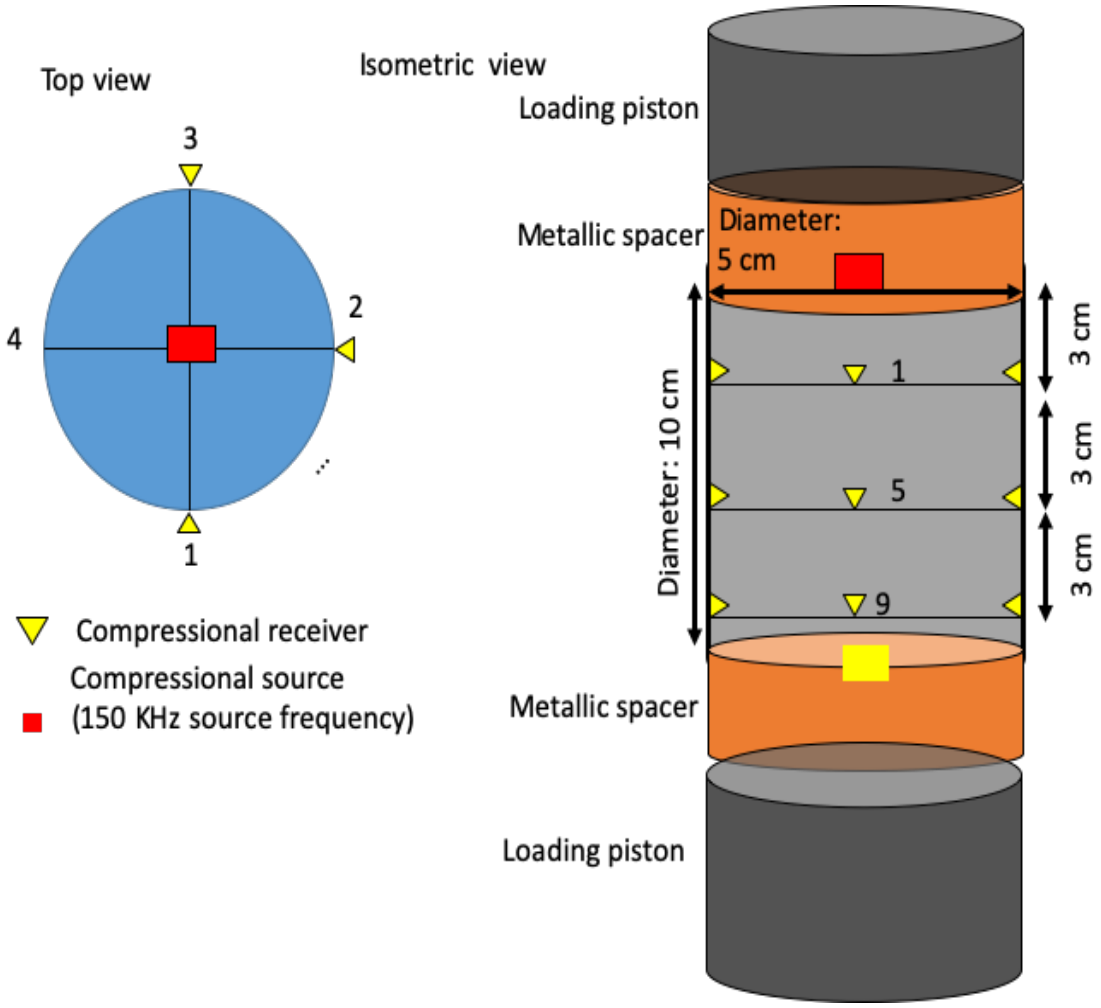

Figure A-1-4 Loading scheme and waveform acquisition.

Element composition	Concentration %
$CaCO_3$	97.30%
$MgCO_3$	0.40%
Al_2O_3	0.50%
SiO_2	1.70%

Table A-1 . XRF mineralogy composition of the tested rock sample

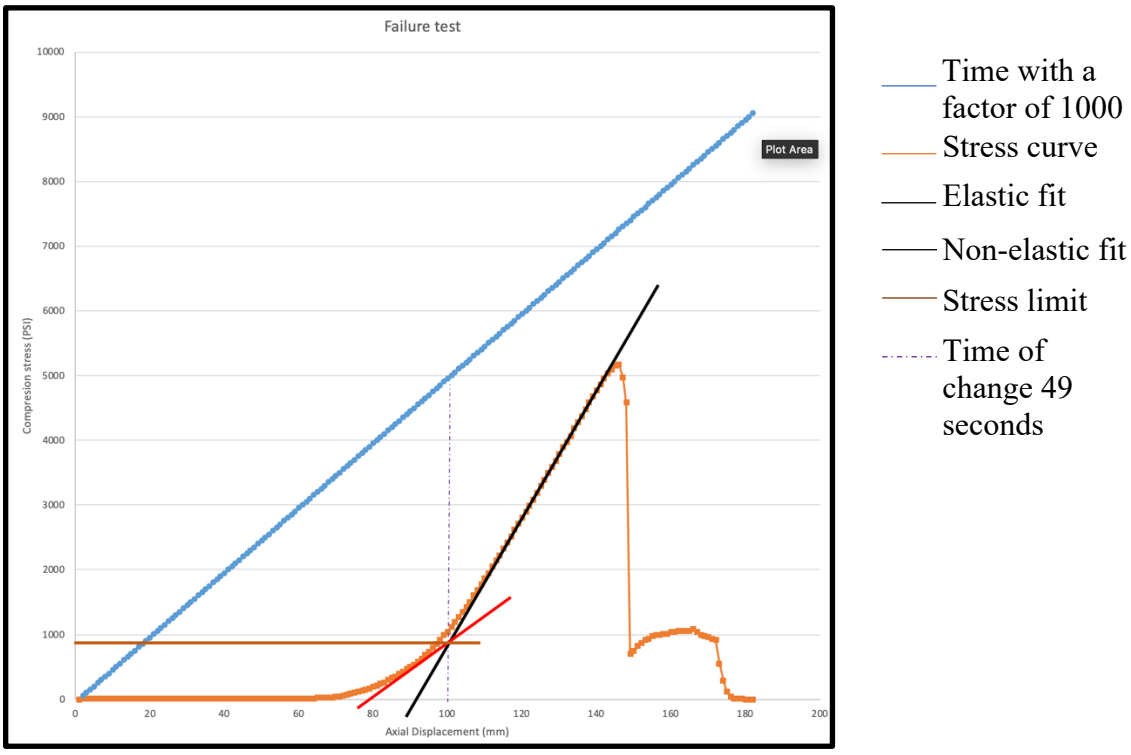

Figure A-1-5. Failure test to determine the maximum stress and the elastic behavior. The non-linear and linear change exhibit the non-elastic and elastic behavior of the rock.

The velocity measurements for monitoring the velocity background, that is, without any perturbation, using the scheme on figure A-1-2, shows no velocity perturbation using the coda interferometry method.

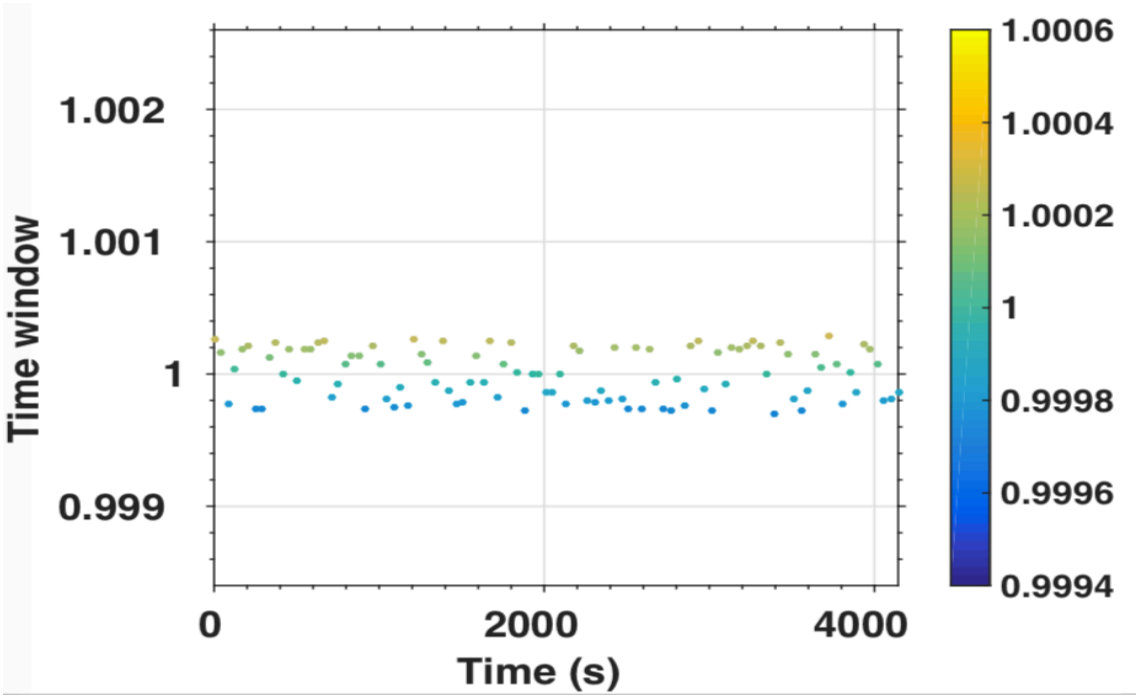

Figure A-1-6. Velocity monitoring without any perturbation for 4200 seconds.

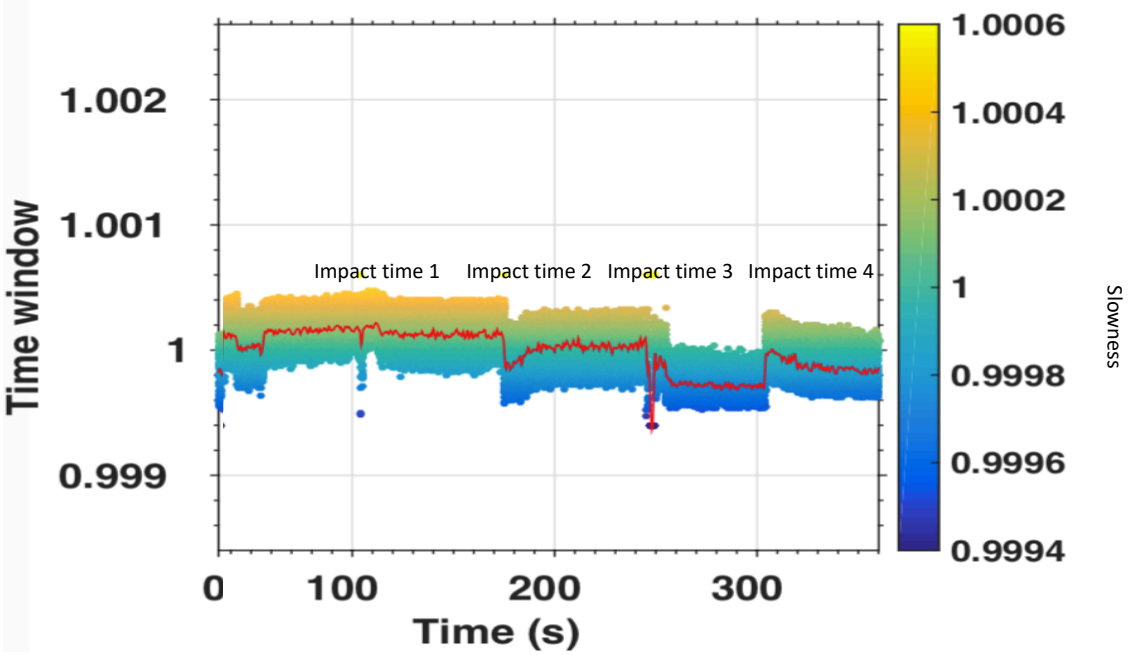

Figure A-1-7. This plot shows the velocity monitoring for monitoring different impacts.

In Fig. A-7 it is evident that there is no clear correlation on the recovery and the impact. Impact 2 at 170 sec suggest a logarithmic recovery or non-elastic rebound, this is probably due to the many unknowns during the acquisition. Scheme A.3 received a heavy block using a loading crane. The drop was controlled with the crane motor, but the impact/landing is not completely flat. The weight of the metallic block is close to 100 kg, that represents a stress with a controlled fall of 840 PSI. On the other hand, acquiring with controlled loading, using a uniaxial loading on the cylinder as in Fig. A- 4, with twelve sensors around the rock cylinder. The velocity monitoring analysis for the twelve sensors is shown in Figure A-1-8.

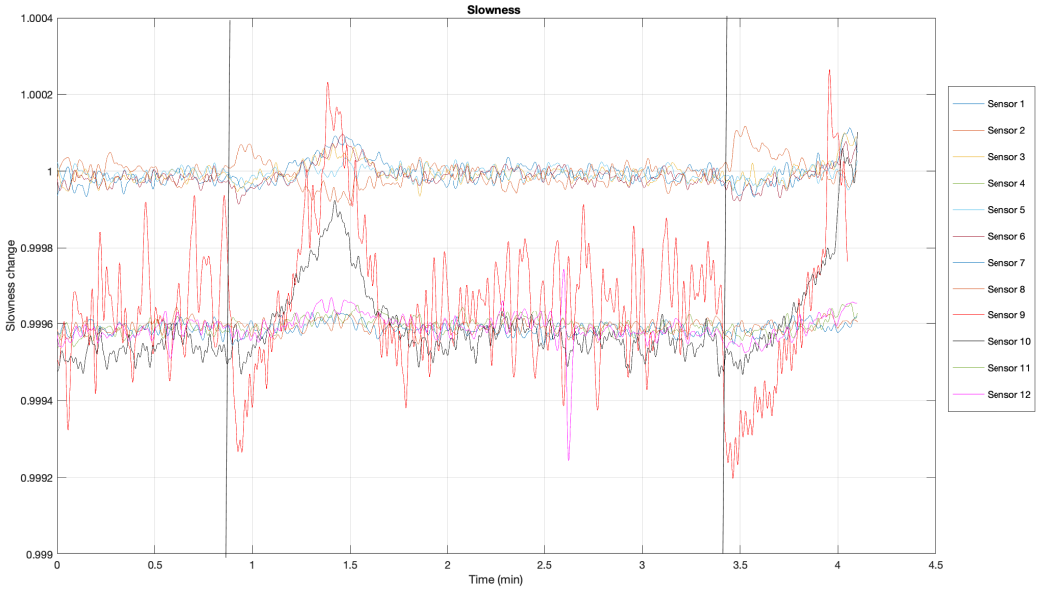

Figure A-1-8. Velocity change with fitting lines from the experiment using the scheme on Figure 1-4. With two uniaxial compressions, the first at 50 seconds and the second at 2 min 40 seconds. The stress applied in this experiment was 250 psi (5% of maximum stress) and 500 psi (10 % of maximum stress), to make sure I was on the non-elastic domain and well below the maximum compressional strength of the rock.

There is a compressional stress applied normally to the rock sample, the stress applied is on the non-elastic behavior. In Figure A-1-6, there is no clear change and it agrees with having no

perturbation. Figure A-1-7, shows the sensibility of the method to monitor the stress change, suggesting an increase on the velocity (reduction on the slowness) that could mean a closure of porosity and cracks for the sensor # 1 (see position inn Figure A-1-3). There is no constant and precise amount of stress and precise timing computed since the test are performed using a loading crane that place the weight on the rock sample at a constant velocity. On the other hand, for results in Figure A-1-8, I plot all the sensors to show the variability of the method to monitor stress perturbation. Sensors 1-4 are on the top position, 5 to 8 are in the middle and 9-12 are on the bottom. The stress applied is 5% and 10% of the maximum compressive strength (see Figure A-5) for the first and second test. The sensor 1, 2 and 4 have a reduction in the slowness and that begins with the compression, to reach that amount of stress it takes close to 5 second and then there is a increase on the slowness (reduction of velocity) to follow a recovery to a normal state of slowness (close to 1). Sensor 3 on the other hand shows the opposite performance (opposite polarity of slowness), suggesting that the stress distribution is not homogenous, opening the pores or reducing the strength of the material framework and then bouncing to the be faster to then recover to the normal state of slowness. This takes place in ~45 seconds, then I continue monitoring the waveforms and perform the experiment a second time at 2 min 40 seconds with a larger stress applied (500 PSI) the sample does not recover completely, and I stop recording. Sensors 5-8 show a constant performance and I shifted .04 % to show this constant performance (no change) probably the sensor do not monitor the stress at this position of the sample (6 cm) below the top. The sensors 9-12 shows the larges variation, due to the difference on the sensors. (Sensor 1-6 were sensors manufactured in Germany) sensors 7-12 were the acoustic sensors I made from the piezoelectric crystals. I bulk shifted the profile .04 % to compare the changes. The performance is similar, sensor

9, 10, and 12 shows an increase on the velocity (reduction on the slowness) to rebound to a slower portion and the stabilize at 1. Sensor 11 shows and opposite behavior, the alignment of this opposite behavior could be explained by a difference in porosity distribution on the sample (Fig. A-1-9). One of the first steps to confirm this non-linear behavior would be to homogenize the sensors to have a consistency on the quality of the waveform recorded. A second step would be to perform a computational tomography to monitor the stress change as a difference velocity perturbation to have a 3D distribution of this changes.



Figure A-1-9. Portions of the rock sample with a difference in the porosity distribution. Red line represents the middle of the sample.

Appendix B: Table with the wellbores analyzed in the Brittleness Index characterization.

The total list of the boreholes used by API number is on Table B-1-1

API #	Surf X	Surf Y	Lat	Long	KB elevation (ft)	Classification
35100000000000	2316574	534193	36.46269	-96.9234	821	DRY
35100000000000	2293389	537471.8	36.47238	-97.0022	845	Minor Gas
35100000000000	2295182	560958.2	36.53684	-96.9952	932	DRY
35100000000000	2292586	558296.3	36.5296	-97.0042	925	Minor Oil
35100000000000	2320935	555341.7	36.52065	-96.9078	991	Minor Oil
35100000000000	2326176	559393.3	36.53161	-96.8898	1039	Oil
35100000000000	2326176	559393.3	36.53161	-96.8898	1036	DRY
35100000000000	2325524	557403.7	36.52617	-96.8921	1044	Minor Oil
35100000000000	2325513	558723.6	36.52979	-96.8921	1015	DRY
35100000000000	2314305	558555.4	36.52968	-96.9303	963	DRY
35100000000000	2332112	558095.7	36.52786	-96.8697	888	DRY
35100000000000	2322193	561315.3	36.53702	-96.9033	1019	Abandoned Minor O&G
35100000000000	2326921	552778.4	36.51342	-96.8875	995	Minor Oil
35100000000000	2322845	561330.8	36.53704	-96.9011	1019	Abandoned Minor O&G
35100000000000	2327493	558782.8	36.52989	-96.8854	946	Oil
35100000000000	2327493	558782.8	36.52989	-96.8854	946	DRY
35100000000000	2311961	536125.3	36.46814	-96.9391	847	DRY
35100000000000	2318959	553986.6	36.51699	-96.9146	1044	Oil
35100000000000	2318959	553986.6	36.51699	-96.9146	1044	DRY
35100000000000	2322840	561330.7	36.53704	-96.9011	1017	Oil
35100000000000	2322840	561330.7	36.53704	-96.9011	1017	Minor Oil
35100000000000	2310677	532767.9	36.45895	-96.9436	851	Oil
35100000000000	2313278	538806.7	36.47546	-96.9345	920	DRY

35100000000000	2324418	538934.1	36.47547	-96.8966	883	Oil
35100000000000	2320781	559634.5	36.53244	-96.9082	945	Oil
35100000000000	2320543	561284.3	36.53698	-96.9089	945	DRY
35100000000000	2323564	556043.8	36.52249	-96.8988	1016	DRY
35100000000000	2323564	556043.8	36.52249	-96.8988	1016	Oil
35100000000000	2321529	561634.6	36.53791	-96.9055	948	DRY
35100000000000	2318236	561231.8	36.53691	-96.9168	905	DRY
35100000000000	2325646	544078.3	36.48956	-96.8922	940	Oil
35100000000000	2336086	554208.3	36.51705	-96.8563	894	DRY
35100000000000	2333978	561447.4	36.53701	-96.8632	928	DRY
35100000000000	2304665	557457.3	36.52695	-96.9631	948	Oil
35100000000000	2321512	560474.2	36.53473	-96.9057	968	Oil
35100000000000	2320187	556129.7	36.52283	-96.9103	1048	Oil
35100000000000	2325541	557742.5	36.5271	-96.892	1056	Oil plugged
35100000000000	2318510	555802.6	36.52199	-96.916	1057	Minor Oil
35100000000000	2320512	560503.4	36.53484	-96.9091	929	Oil
35100000000000	2322704	554555	36.51843	-96.9018	993	Oil
35100000000000	2317972	553644.5	36.51608	-96.918	1032	Abandoned Minor O&G
35100000000000	2323831	557614.9	36.5268	-96.8979	1016	Oil
35100000000000	2317670	552880.3	36.51399	-96.919	1044	DRY
35100000000000	2329308	552340.5	36.51214	-96.8794	922	DRY
35100000000000	2320030	552926.8	36.51404	-96.911	1045	Oil
35100000000000	2326639	557879.4	36.52744	-96.8883	1017	Oil
35100000000000	2326103	558701.6	36.52971	-96.8901	1006	Abandoned oil and Gas
35100000000000	2326103	558701.6	36.52971	-96.8901	1006	DRY
35100000000000	2330684	561640.4	36.53764	-96.8744	933	DRY
35100000000000	2331406	560745.6	36.53516	-96.872	924	Abandoned oil and Gas
35100000000000	2330851	554790.6	36.51882	-96.8741	947	Abandoned Minor O&G
35100000000000	2333435	554841.5	36.51888	-96.8653	919	Abandoned Minor O&G
35100000000000	2327533	554781.6	36.5189	-96.8854	939	Oil

35100000000000	2307412	556164.6	36.52332	-96.9538	1011	DRY
35100000000000	2327211	556782.4	36.52441	-96.8864	984	Oil
35100000000000	2311966	532683.8	36.45868	-96.9392	843	Oil
35100000000000	2311966	532683.8	36.45868	-96.9392	843	Minor Oil
35100000000000	2311296	533485	36.4609	-96.9414	840	Minor Gas
35100000000000	2295434	541175.9	36.48249	-96.9951	841	Gas
35100000000000	2318374	552344.1	36.51249	-96.9166	1028	DRY
35100000000000	2326866	560741.5	36.53529	-96.8874	1022	Oil
35100000000000	2331421	559996.8	36.5331	-96.8719	904	Gas
35100000000000	2320326	560382.2	36.53451	-96.9097	913	Oil
35100000000000	2320558	561360.6	36.53719	-96.9089	935	Oil
35100000000000	2319883	561269.2	36.53696	-96.9112	909	Abandoned oil and Gas
35100000000000	2321038	561295.5	36.537	-96.9072	958	Oil
35100000000000	2320838	559968.8	36.53336	-96.908	946	Injection
35100000000000	2299976	544443.3	36.49134	-96.9795	935	Gas
35100000000000	2316601	540082.3	36.47887	-96.9231	924	Oil
35100000000000	2310275	560569.6	36.53533	-96.9439	877	Abandoned oil and Gas
35100000000000	2310235	560570	36.53533	-96.944	877	Abandoned oil and Gas
35100000000000	2310255	560569.8	36.53533	-96.944	877	Minor Gas
35100000000000	2294774	539208.9	36.47711	-96.9974	852	Injection
35100000000000	2294774	539208.9	36.47711	-96.9974	852	DRY
35100000000000	2297479	533300.5	36.4608	-96.9884	854	Minor Oil
35100000000000	2297479	533300.5	36.4608	-96.9884	854	DRY
35100000000000	2294149	534608.7	36.46449	-96.9997	947	DRY
35100000000000	2336255	539773	36.4774	-96.8563	852	DRY
35100000000000	2331606	535050.4	36.46458	-96.8723	916	Minor Oil
35100000000000	2330971	533066.4	36.45915	-96.8745	922	DRY
35100000000000	2329671	534370	36.46277	-96.8789	912	DRY
35100000000000	2332336	537022.2	36.46997	-96.8697	903	Minor Oil
35100000000000	2292828	541173.3	36.48256	-97.004	863	Minor Gas

35100000000000	2294114	539202.9	36.47711	-96.9996	856	DRY
35100000000000	2294114	539202.9	36.47711	-96.9996	856	Gas
35100000000000	2332266	535059.1	36.46458	-96.8701	958	DRY
35100000000000	2293982	539366.7	36.47756	-97.0001	857	Oil plugged
35100000000000	2293982	539366.7	36.47756	-97.0001	857	Oil
35100000000000	2292808	539863.2	36.47896	-97.0041	855	DRY
35100000000000	2293532	539876.2	36.47898	-97.0016	860	Oil plugged
35100000000000	2294128	538548.5	36.47531	-96.9996	858	Oil
35100000000000	2294475	537231.4	36.47169	-96.9985	857	DRY
35100000000000	2335610	534445.8	36.46279	-96.8587	942	DRY
35100000000000	2296755	538606.7	36.4754	-96.9907	1053	Oil
35100000000000	2293460	539202.9	36.47713	-97.0019	850	DRY
35100000000000	2334941	537749	36.47188	-96.8609	934	Minor Oil
35100000000000	2334941	537749	36.47188	-96.8609	934	Abandoned Minor O&G
35100000000000	2334992	535102.3	36.46461	-96.8608	939	Minor Gas
35100000000000	2333520	533756.9	36.46096	-96.8658	965	Oil
35100000000000	2325759	534976.9	36.46456	-96.8922	835	Oil plugged
35100000000000	2324441	534300.8	36.46274	-96.8967	836	Minor Oil
35100000000000	2297135	534947.8	36.46534	-96.9895	852	Minor Gas
35100000000000	2333004	535398.2	36.46549	-96.8675	931	Abandoned oil and Gas
35100000000000	2327394	535336.2	36.4655	-96.8866	931	Abandoned oil and Gas
35100000000000	2325752	535635.7	36.46637	-96.8922	931	DRY
35100000000000	2327088	533009.5	36.45911	-96.8877	944	Abandoned oil and Gas
35100000000000	2325761	534322.2	36.46276	-96.8922	960	Abandoned oil and Gas
35100000000000	2327074	534176.6	36.46232	-96.8877	960	Abandoned oil and Gas
35100000000000	2331650	534392	36.46277	-96.8722	960	DRY
35100000000000	2331692	534064.4	36.46187	-96.872	960	DRY
35100000000000	2335034	539718.1	36.47729	-96.8605	931	Oil plugged
35100000000000	2293167	536235.5	36.46899	-97.003	853	Gas plugged
35100000000000	2332315	535059.8	36.46458	-96.8699	962	Abandoned oil and Gas

35100000000000	2331646	535150.8	36.46485	-96.8722	962	Abandoned oil and Gas
35100000000000	2332604	534074.3	36.46186	-96.8689	962	Abandoned oil and Gas
35100000000000	2293061	539867.7	36.47897	-97.0032	962	Oil
35100000000000	2295669	537901.3	36.47349	-96.9944	857	Minor Oil
35100000000000	2336304	535747.6	36.46634	-96.8563	935	DRY
35100000000000	2336296	539618.1	36.47697	-96.8562	857	Oil
35100000000000	2298462	533968.3	36.46261	-96.985	831	Abandoned oil and Gas
35100000000000	2297384	541884.9	36.48438	-96.9884	863	DRY
35100000000000	2300554	550500.1	36.50796	-96.9773	1032	DRY
35100000000000	2299262	549168.9	36.50434	-96.9818	979	DRY
35100000000000	2297909	552439	36.51336	-96.9863	889	DRY
35100000000000	2319030	547414.4	36.49893	-96.9146	967	Abandoned Minor O&G
35100000000000	2315125	544718.8	36.49165	-96.928	1046	DRY
35100000000000	2309985	537416.1	36.47174	-96.9457	917	Minor Oil
35100000000000	2312670	539477.6	36.47732	-96.9365	947	Minor Oil
35100000000000	2331587	550182.5	36.50614	-96.8718	885	Minor Oil
35100000000000	2295387	542253.6	36.48545	-96.9952	849	Minor Oil
35100000000000	2305972	541961.8	36.48435	-96.9592	986	DRY
35100000000000	2294703	545151.1	36.49343	-96.9974	862	Abandoned Minor O&G
35100000000000	2293359	547124.5	36.49889	-97.0019	866	Oil
35100000000000	2325673	541595.6	36.48274	-96.8922	898	DRY
35100000000000	2311961	536125.3	36.46814	-96.9391	847	Abandoned Minor O&G
35100000000000	2313715	538042.7	36.47335	-96.933	893	DRY
35100000000000	2313847	542750.3	36.48628	-96.9324	976	Minor Oil
35100000000000	2307883	544603	36.49154	-96.9526	1034	Minor Oil
35100000000000	2318445	542151	36.48449	-96.9168	948	Minor Oil
35100000000000	2313769	548018.9	36.50075	-96.9325	1060	DRY
35100000000000	2313814	534823.8	36.46451	-96.9328	849	DRY
35100000000000	2313814	534823.8	36.46451	-96.9328	849	Oil
35100000000000	2312619	533497.9	36.4609	-96.9369	841	Abandoned Minor O&G

35100000000000	2305823	553159.8	36.51511	-96.9593	1018	DRY
35100000000000	2318468	542153.2	36.4845	-96.9167	930	Oil
35100000000000	2327015	542968.3	36.48647	-96.8876	917	Injection
35100000000000	2326333	541526	36.48253	-96.89	897	Oil
35100000000000	2314273	537820.9	36.47273	-96.9311	888	Oil
35100000000000	2313278	538806.7	36.47546	-96.9345	920	Oil
35100000000000	2310566	542701.3	36.48624	-96.9436	1045	Abandoned Minor O&G
35100000000000	2310638	534788.1	36.4645	-96.9436	848	DRY
35100000000000	2328995	541635.1	36.48275	-96.8809	865	DRY
35100000000000	2331728	550067.7	36.50582	-96.8713	888	Abandoned Minor O&G
35100000000000	2296051	542855.3	36.48709	-96.9929	867	DRY
35100000000000	2306095	547329.6	36.49909	-96.9586	1073	Minor Gas
35100000000000	2302603	546013.4	36.49557	-96.9705	1026	DRY
35100000000000	2303638	542922	36.48705	-96.9671	975	Oil
35100000000000	2326479	551652.5	36.51034	-96.8891	963	Oil
35100000000000	2312584	538115.3	36.47358	-96.9369	918	Oil
35100000000000	2310594	536770.6	36.46995	-96.9437	893	DRY
35100000000000	2307337	551590.3	36.51075	-96.9542	1055	Oil
35100000000000	2313913	536810.1	36.46996	-96.9324	876	Oil
35100000000000	2313931	534169.3	36.46271	-96.9324	839	Oil
35100000000000	2328923	548201.9	36.50079	-96.8809	897	DRY
35100000000000	2304804	553505.6	36.51609	-96.9628	1029	Abandoned Minor O&G
35100000000000	2304661	541273.2	36.48249	-96.9637	963	Oil
35100000000000	2329953	544640.5	36.49097	-96.8775	899	Abandoned Minor O&G
35100000000000	2310469	548289	36.50159	-96.9437	1076	DRY
35100000000000	2310469	548289	36.50159	-96.9437	1076	DRY
35100000000000	2305030	536009.8	36.46803	-96.9626	843	Oil
35100000000000	2309905	540052.3	36.47899	-96.9459	960	Oil
35100000000000	2315703	546419	36.4963	-96.926	972	Oil
35100000000000	2330264	545613	36.49363	-96.8764	906	Oil

35100000000000	2329641	543632.2	36.48821	-96.8786	888	Oil
35100000000000	2330942	544773.5	36.4913	-96.8742	901	Oil
35100000000000	2330253	546932.8	36.49726	-96.8764	915	Oil
35100000000000	2328907	550155.7	36.50615	-96.8809	928	Oil
35100000000000	2305918	544602	36.4916	-96.9593	1034	Abandoned oil and Gas
35100000000000	2305918	544602	36.4916	-96.9593	1034	Abandoned oil and Gas
35100000000000	2329559	550824.7	36.50797	-96.8786	934	Abandoned oil and Gas
35100000000000	2315370	549656.7	36.5052	-96.927	1017	DRY
35100000000000	2330978	540315.1	36.47906	-96.8742	831	DRY
35100000000000	2326860	542968.1	36.48647	-96.8881	922	DRY
35100000000000	2332156	543657.7	36.4882	-96.8701	838	Abandoned minor O&G
35100000000000	2332156	543657.7	36.4882	-96.8701	838	DRY
35100000000000	2309835	546632.8	36.49706	-96.9459	1073	DRY
35100000000000	2311134	547967.6	36.50069	-96.9414	1082	DRY
35100000000000	2333246	545658.7	36.49366	-96.8663	834	Oil
35100000000000	2305300	543923.9	36.48976	-96.9614	1034	Abandoned oil and Gas
35100000000000	2305300	543923.9	36.48976	-96.9614	1034	Oil
35100000000000	2304603	545262.7	36.49345	-96.9638	1035	DRY
35100000000000	2332892	548915.1	36.50262	-96.8674	869	Abandoned oil and Gas
35100000000000	2305473	545074	36.49291	-96.9608	1033	Minor Oil
35100000000000	2305247	545253.2	36.49341	-96.9616	1043	Oil
35100000000000	2329569	549834.8	36.50525	-96.8786	913	DRY
35100000000000	2309089	553852.4	36.51691	-96.9482	1018	DRY
35100000000000	2306935	542004.7	36.48444	-96.9559	983	Abandoned oil and Gas
35100000000000	2307343	538672.8	36.47527	-96.9547	930	Oil
35100000000000	2332239	543358.5	36.48738	-96.8698	838	Abandoned oil and Gas
35100000000000	2321707	550063.9	36.50613	-96.9054	800	DRY
35100000000000	2328558	551458	36.50974	-96.882	960	Oil
35100000000000	2328558	551458	36.50974	-96.882	960	DRY
35100000000000	2302709	537980.6	36.47351	-96.9705	853	Oil

35100000000000	2312621	534811.9	36.46451	-96.9369	848	Oil plugged
35100000000000	2312618	534154.1	36.4627	-96.9369	847	Oil
35100000000000	2314618	535494.1	36.46632	-96.9301	848	Oil
35100000000000	2312927	536264.9	36.46849	-96.9358	848	Oil
35100000000000	2310645	534075.8	36.46255	-96.9436	850	DRY
35100000000000	2331580	550842.4	36.50795	-96.8718	869	Minor Gas
35100000000000	2307473	549573.9	36.50521	-96.9538	1046	Minor Oil
35100000000000	2302617	544567.6	36.4916	-96.9705	1000	Abandoned O&G
35100000000000	2297542	540916.2	36.48172	-96.9879	854	Minor Gas
35100000000000	2297361	540215.3	36.4798	-96.9886	850	Oil
35100000000000	2330962	542314.3	36.48455	-96.8742	839	DRY
35100000000000	2322856	551063.9	36.50884	-96.9014	974	Abandoned Minor O&G
35100000000000	2331275	544314.5	36.49003	-96.8731	887	Abandoned oil and Gas
35100000000000	2305923	545285.8	36.49348	-96.9593	1039	Abandoned oil and Gas
35100000000000	2326396	542248.2	36.48451	-96.8897	913	Oil
35100000000000	2308584	539973.4	36.47881	-96.9504	955	Oil
35100000000000	2308684	539976.4	36.47881	-96.9501	955	Oil
35100000000000	2308784	539979.3	36.47882	-96.9497	955	Abandoned oil and Gas
35100000000000	2308925	539876.8	36.47853	-96.9493	944	Abandoned oil and Gas
35100000000000	2299989	544554.4	36.49164	-96.9795	935	Injection
35100000000000	2300079	544554.8	36.49164	-96.9792	970	Abandoned oil and Gas
35100000000000	2319187	540103.5	36.47884	-96.9143	881	Abandoned oil and Gas
35100000000000	2319097	540102.1	36.47884	-96.9146	878	Oil
35100000000000	2299976	544423.3	36.49128	-96.9795	935	Oil
35100000000000	2299977	544383.3	36.49117	-96.9795	935	Oil
35100000000000	2299976	544403.3	36.49123	-96.9795	935	Abandoned oil and Gas
35100000000000	2299977	544363.3	36.49112	-96.9795	935	Abandoned oil and Gas
35100000000000	2326203	544899.8	36.4918	-96.8903	910	Oil
35100000000000	2316581	540082.1	36.47887	-96.9232	946	Abandoned oil and Gas
35100000000000	2316561	540081.8	36.47887	-96.9233	946	Oil

35100000000000	2316621	540082.5	36.47887	-96.9231	946	Abandoned oil and Gas
35100000000000	2331548	542745.1	36.48571	-96.8722	860	Abandoned oil and Gas
35100000000000	2331488	542745.1	36.48572	-96.8724	860	Abandoned oil and Gas
35100000000000	2330778	542744	36.48574	-96.8748	835	Abandoned oil and Gas

Table 2. Location of the boreholes used in the analysis; 234 wellbores were studied in this project to integrate different the distribution of this table is in Figure B.0-1

That corresponds to the distribution shown in the Figure B-1-1

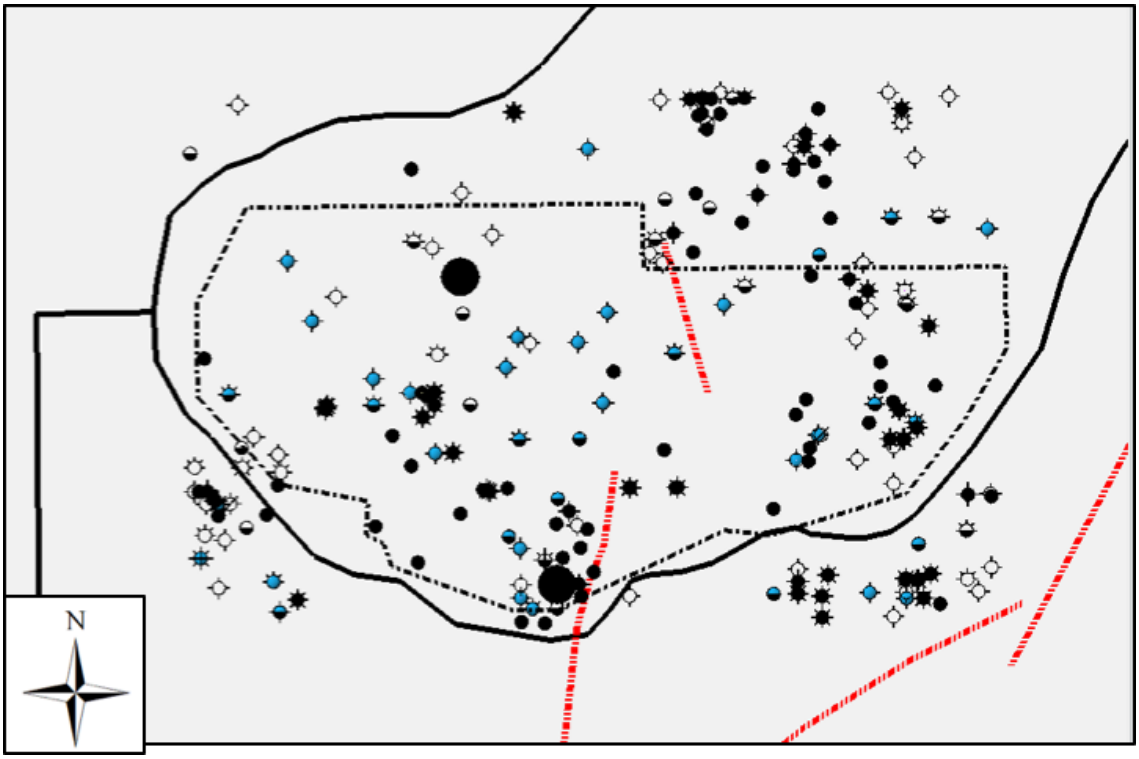

Figure B-1-1. Location of total list of boreholes analyzed in black symbols, blue dots represents the boreholes that were used during the geomechanical modeling either as mud-profiles to calibrate pressure, or formation integrity test when cemented the casing sites.

The boreholes that contributed to the geomechanical model have the distribution shown in figure B-1-1. Further information in table 7.

API #	Surf X	Surf Y	Lat	Long	KB elevation (m)	TD (m)
35117200940000	2324441.46	534300.84	36.46274369	-96.89669329	255.4	987.804878
35117202100000	2297134.66	534947.77	36.4653372	-96.98952381	243.9	1013.719512
35117210350000	2333003.71	535398.22	36.46548711	-96.86753529	292.6	960.9756098
35117212640000	2327088.46	533009.53	36.45911381	-96.8877429	292.6	923.1707317
35117216360000	2331692.14	534064.41	36.46186541	-96.87204791	260.0	925.9146341
35117218370000	2335034.11	539718.09	36.47728741	-96.8604586	258.5	939.9390244
35117218470000	2293167.1	536235.54	36.4689871	-97.0029705	258.2	1021.036585
35113000450000	2325524.38	557403.67	36.52616711	-96.89211451	288.7	491.7682927
35113000690000	2616954	5688636	36.50433819	-96.98178369	284.4	101.5243902
35113000850000	2314305.32	558555.4	36.52967619	-96.93025098	300.6	888.4146341
35113000860000	2297908.86	552438.99	36.51335931	-96.98627009	262.8	999.695122
35113000910000	2319029.71	547414.41	36.4989309	-96.91459659	264.0	975.6097561
35113001320000	2315124.79	544718.75	36.4916458	-96.92798209	258.2	998.7804878
35113001330000	2309985.33	537416.07	36.47174171	-96.94573431	272.2	967.3780488
35113001560000	2312670.01	539477.63	36.4773239	-96.93652759	297.5	953.0487805
35113003020000	2326921.4	552778.35	36.51341881	-96.88754069	323.1	958.5365854
35113005070000	2305972.19	541961.8	36.48434669	-96.95921629	256.4	1032.621951
35113006670000	234703.31	515107.3	36.4934326	-96.9974333	250	258.2317073
35113006680000	2293359.04	547124.5	36.49889119	-97.0019371	283.0	995.4268293
35113007060000	2325672.65	541595.55	36.48274191	-96.89222379	279.5	958.8414634
35113008220000	2313847.14	542750.32	36.48627769	-96.93240179	263.7	992.0731707
35113008440000	2307882.57	544603	36.49154499	-96.9526216	270.7	914.3292683
35113011120000	2318445.27	542151.04	36.48449171	-96.91678459	264.3	1051.219512
35113011150000	2313768.51	548018.93	36.50075159	-96.93247219	327.1	938.1097561
35113012890000	2313814.2	534823.75	36.46450631	-96.9328102	293.5	894.2073171
35113012920000	2312618.81	533497.85	36.46090039	-96.93692442	272.2	894.2073171
35113049100000	27014.94	542968.32	36.4864704	-96.88760488	273.1	1707.317073
35113204130000	2324418.44	538934.13	36.47547091	-96.8965925	274.0	960.6707317
35113204760000	2323564.05	556043.8	36.5224932	-96.89883819	257.0	1032.621951

35113205040000	2310565.97	542701.33	36.48624171	-96.94356411	276.2195122	992.3780488
35113207210000	2310638.03	54788.14	36.46450391	-96.94361188	276.2195122	1073.170732
35113212660000	2336085.88	554208.31	36.517054	-96.85630102	282.9268293	949.3902439
35113232240000	2302602.83	546013.42	36.49557419	-96.97053039	254.2682927	965.2439024
35113245720000	2312584.19	538115.34	36.47358459	-96.9368702	283.5365854	941.7682927
35113250660000	2307337.38	551590.34	36.51075359	-96.95422009	292.6829268	917.9878049
35113255490000	2313912.58	536810.07	36.46995929	-96.93240139	292.6829268	911.5853659
35113262990000	204661.34	531273.24	36.4824939	-96.96369989	271.3414634	1067.073171
35113263820000	2329952.74	544640.45	36.49097041	-96.8775466	264.9390244	1000.304878
35113263830000	2310469.16	548288.95	36.5015924	-96.94368661	318.902439	918.902439
35113263890000	2309905.43	540052.34	36.4789853	-96.94590869	259.1463415	1064.634146
35113275260000	2315370.07	549656.73	36.5052017	-96.92696209	318.902439	934.1463415
35113277050000	2332156.23	543657.72	36.48820091	-96.87009022	269.8170732	949.695122
35113280050000	2309834.57	546632.76	36.49706221	-96.94590669	300.6097561	284.4512195
35113286090000	2333245.75	545658.71	36.4936622	-96.86630481	264.0243902	289.9390244
35113288540000	2304603.14	545262.74	36.4934538	-96.96375301	258.2317073	1158.536585
35113288600000	2332892.06	548915.05	36.50261779	-96.86737871	272.2560976	597.5609756
35113291620000	2305246.72	545253.2	36.49340871	-96.96156409	315.2439024	581.097561
35113303470000	2302708.56	537980.62	36.47350691	-96.9704605	283.5365854	373.4756098
35113303520000	2312621.28	534811.9	36.46450971	-96.93686709	279.5731707	303.9634146
35113307300000	2310644.51	534075.81	36.46254711	-96.94361621	318.597561	251.8292683
35113367680000	2311965.68	532683.76	36.45868389	-96.93917549	327.1341463	237.195122
35113438760000	2326396.25	542248.21	36.4845119	-96.88973729	255.7926829	978.9634146
35113447490000	2299975.87	544443.29	36.4913376	-96.97952291	292.6829268	2207.317073
35113448320000	2316580.79	540082.09	36.47886579	-96.92320429	274.695122	2342.073171
35117000510000	2297479.46	533300.49	36.46080261	-96.98840969	284.7560976	983.2317073
35117001840000	2329670.53	534370	36.46276911	-96.87890998	255.4878049	911.5853659
35117002580000	2332336.15	537022.15	36.469969	-96.869741	327.1341463	836.5853659
35117003120000	2294114.01	539202.89	36.47711101	-96.99964642	254.2682927	1008.536585
35117003510000	2292807.86	539863.23	36.4789617	-97.0040656	314.9390244	763.7195122

Table 3. Location of boreholes that were included in the geomechanical model

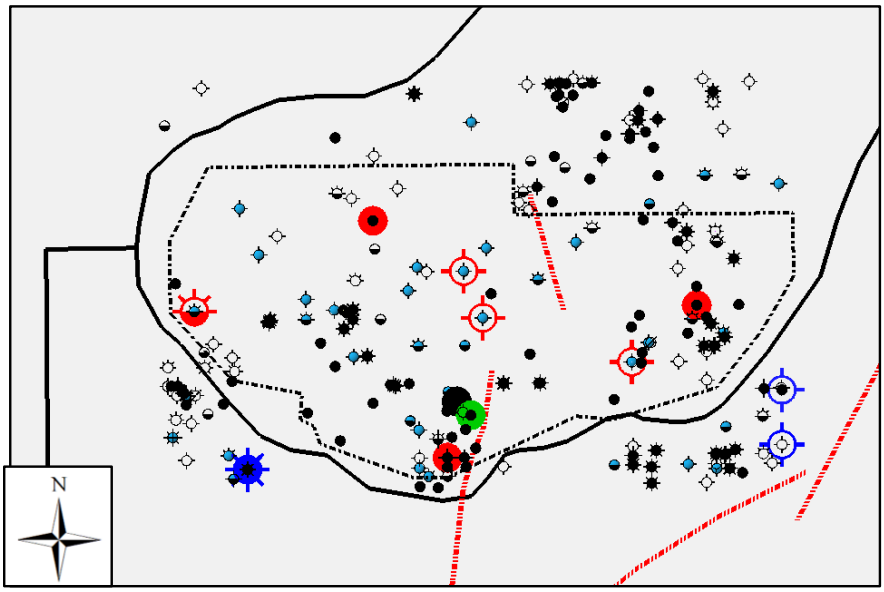

Figure B-1-2 Color location represent boreholes with wireline information, where I derived and compute multiple attributes. This survey has a well density of 3 wells per square kilometer.

Wireline boreholes with name, location, and position are in Table 8.

API #	Surf X	Surf Y	Lat	Long	KB elevation (m)	TD (m)
35113011150000	2313768.50	548018.9	36.50075	-96.9325	246.15	1264.939
35113250660000	2307337.40	551590.3	36.51075	-96.9542	67.69	1214.939
35113006670000	2294703.30	545151.1	36.49343	-96.9974	289.54	1274.085
35113001320000	2315124.80	544718.8	36.49165	-96.928	261.54	1259.146
35113268580000	2330264.50	545612.9	36.49363	-96.8764	202.15	1005.793
35113007060000	2325672.60	541595.5	36.48274	-96.8922	246.15	1280.488
35113303520000	2312621.30	534811.9	36.46451	-96.9369	240.00	1219.512
35113203730000	2313278.30	538806.7	36.47546	-96.9345	246.15	1176.829
35113200030000	2314273.20	537820.9	36.47272	-96.9311	40.00	1170.122
35113303520000	2312621.3	534811.9	36.46451	-96.9369	246.15	1219.512
35117232600000	2336304.20	535747.6	36.46634	-96.8563	202.46	1621.037
35117232610000	2336296.20	539618.1	36.47697	-96.8562	283.38	1257.012
35117235530000	2298461.70	533968.3	36.46261	-96.985	43.08	1255.793

Table 4. Latitude and longitude of the boreholes with wireline logs.